New Applications of Satellite-Measured Tropical Cyclone Wind Speeds

by

David R. Mayers

A dissertation submitted in partial fulfillment
of the requirements for the degree of
Doctor of Philosophy
(Applied Physics)
in the University of Michigan
2021

Doctoral Committee:

Professor Christopher Ruf, Chair
Associate Professor Jeremy N. Bassis
Associate Research Scientist Darren McKague
Dr. Lucrezia Ricciardulli, Remote Sensing Systems
Professor Kamal Sarabandi

David R. Mayers

drmayers@umich.edu

ORCID iD: 0000-0001-8935-1867

Acknowledgements

I am grateful to have had Chris Ruf as a research advisor. He taught me how to approach research and scientific writing. He was always very supportive of my projects and ideas, while also promptly providing feedback and helpful suggestions of his own. I am thankful Chris took me on despite coming from another department and that he introduced me to remote sensing.

I am indebted to my committee members, Drs. McKague, Sarabandi, Ricciardulli, and Bassis, for their insights and support.

I am thankful that my parents provided a solid educational foundation and that they supported my decision to pursue a PhD despite being unfamiliar with the concept.

I am blessed to have Meredith's loving support throughout graduate school. Thank you for dealing with my irregular work schedule and for sacrificing kitchen space for my dual-monitor workstation.

I am thankful that the Applied Physics Program provided an excellent learning experience and opened the doors to so many research opportunities throughout the University.

The Climate and Space Sciences and Engineering Department accepted me as an honorary member; I am grateful for the support I received in education, logistics, and IT.

I am happy to have had Tianlin, Raji, Rachel, Mohammad, and Charlie as coworkers. I learned much from all of you and you all made my graduate school experience more enjoyable.

And, finally, I thank anyone who has contributed to my passion for science and learning.

Table of Contents

List of Tables

List of Figures

Abstract

Major hurricanes are becoming more frequent due to climate change and the warming of the oceans. Now more than ever, the ability to model hurricanes accurately and provide advanced warning to affected areas is crucial. However, while hurricane track forecasting has greatly improved, there has been little improvement in intensity forecasting, partly due to inadequate observations and modeling of the inner core of the storm. CYGNSS, an experimental NASA satellite mission launched in December 2016, is designed to frequently measure surface wind speeds in hurricanes via GPS reflections. These additional measurements should improve forecasting of hurricane rapid intensification.

This dissertation looks at new ways to use and interpret remotely sensed wind speeds in hurricanes. First, we look at how estimated storm intensity is affected by the spatial resolution of the satellite. Satellite-measured wind speeds are not point measurements—a single measurement is of a broad area on the surface where contributions from each part of the surface are given weight according to the antenna pattern. Hurricane intensity is usually determined by the maximum wind speed (Vm). Because satellite-measured wind speeds are effectively averages over a large area, the satellite-measured Vm is lower than the true Vm. Unless this is corrected for, hurricane wind fields from satellites will systematically underestimate storm intensity. This work explores how information from any satellite-measured wind field can be used to improve the estimated storm intensity via a scale factor correction.

Next, hurricane parametric wind speed models are examined. Parametric wind models are established using meteorological principles combined with simplifying assumptions about the

environment or storm structure. These models tune several free parameters to wind speed measurements by minimizing the difference between the measurements and the wind field "seen" by the model. Parametric wind models are especially useful for filling in gaps between measurements—once the free parameters are optimized, the model can report a wind speed estimate everywhere in the storm. Hurricane wind field characteristics such as Vm, radial distance to Vm, azimuthal information, and more are easily determined from a full wind field but are more difficult to estimate from a gap-filled wind field. Also, many modeling applications are enabled by having a full wind field. This dissertation discusses limitations of existing parametric wind models, and new parameters are added to allow for improved representation of a wider variety of storms. A parametric wind model is then used to find the center location of a hurricane using the principle that the model fit is best when the correct storm center is assumed. The storm center is the location that optimizes the model fit. Most storm center fixes are done manually—this is one of few automated storm center fix techniques and the only one not using cloud structure seen in satellite imagery. Accurate storm center locations are necessary for forecasting hurricanes, hurricane research, and historical record keeping.

Lastly, a new CYGNSS data product is described which reports gridded surface wind speeds with increased convenience and reliability for users of hurricane-specific data. This product, which will be released to the public in early 2021, processes the CYGNSS wind speeds in a way that allows for self-consistency checks of the data. This new CYGNSS hurricane wind speed product is shown to be in excellent agreement with wind speeds from models and a well-established satellite.

Chapter 1 Introduction

Tropical cyclones (TCs) are low-pressure systems associated with the warm, humid air of the near-equatorial tropics. TCs are known as hurricanes in the Americas, typhoons in south-east Asia, and cyclones in the south Pacific and Indian oceans. No matter the name, TCs typically bring strong wind, heavy rain, tornados, storm surge, and flooding.

TCs cause more damage in the United States than any other form of natural disaster. From 1980 to 2019, TCs caused $954.4 billion in damages which is 53.7% of all costs from billion-dollar natural disasters in the United States in that span ("NOAA National Centers for Environmental Information (NCEI) U.S. Billion-Dollar Weather and Climate Disasters" 2020). In that same timeframe, TCs were responsible for 6507 deaths in the United States, which is 45.6% of the deaths from billion-dollar natural disasters ("NOAA National Centers for Environmental Information (NCEI) U.S. Billion-Dollar Weather and Climate Disasters" 2020). Public interest in TCs has grown in recent years due to climate change and very active hurricane seasons. Anthropogenic warming of the ocean provides additional fuel for these storms. 3 of the 4 most costly hurricanes in the history of the Atlantic basin (Harvey, Maria, Irma) occurred in 2017 alone. Recent studies agree that the frequency of the most intense hurricanes as well as the precipitation potential of TCs will increase due to climate change, but there is disagreement on how the overall frequency of TCs will change (Bacmeister et al. 2018; Walsh et al. 2015; Murakami et al. 2012). As TCs become more destructive, it is more important than ever to understand and forecast these storms to save lives and property.

A tropical disturbance will develop into a tropical cyclone if a few ingredients are simultaneously present. First, a warm water source of at least 27 degrees Celsius is required to power the storm with latent heat (Galvin 2015). Note, latent heat is the energy that is released as moist air rises and condenses in the upper troposphere. Low wind shear, or change in wind speed with height, is also necessary. If the wind shear is too great, the storm structure is distorted, and the latent heat is ventilated away from the developing disturbance preventing further deepening (Gray, 1968). The troposphere must be very humid, and its temperature must fall rapidly with height. If these factors are all present, a positive feedback loop is established which strengthens the storm. Deepening of the surface low causes air on the surface to rush to the storm center. The increasing near-surface wind speed enhances evaporation into the near-surface air. This moistened air rises and condenses high up in the troposphere, releasing latent heat and causing a "warm core". Heating of the troposphere increases the air pressure, creating an upper level high and forcing upper-level air to diverge from the center of the system. Some of this upper-level air sinks back into the center of the storm instead to form a clear eye in the center of the storm. The increased outflow high in the atmosphere removes air from the column above the surface low, further decreasing the surface pressure. Lower surface pressure at the center of the storm results in stronger surface winds which increase both the latent heat flux and the rate of convergence/convection. If all the above conditions are met for tropical cyclone formation, storms will continue to intensify in this manner. However, this simplified positive feedback loop will not continue indefinitely. Strong storms tend to go through phases of intensification and weakening in their lifetimes.

The necessary ingredients come together to form TCs in the north-west Pacific (between March and December), the south Indian Ocean (between November and April), the north-east

Pacific, North Atlantic, and Caribbean (between June and November), and the south-west Pacific (between December and April). Many Atlantic TCs originate from African easterly waves which propagate across the Atlantic, providing the trigger mechanism for TC formation when conditions are favorable (Thorncroft and Hodges 2001; Chen, Wang, and Clark 2008). TCs do not form in the south Pacific because sea surface temperatures are too low. Similarly, TCs have difficulty forming in the south Atlantic due to strong wind shear in the troposphere (Galvin 2015). Figure 1-1 shows historical storm tracks as well as storm intensities according to the Saffir Simpson scale (Rohde 2006).

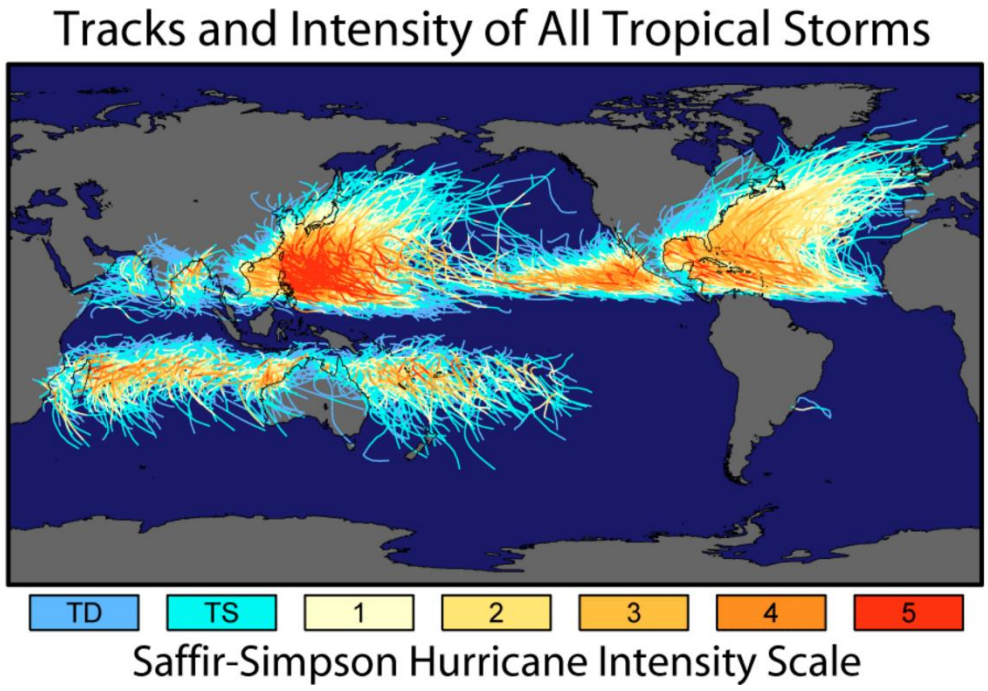

Figure 1-1: Historic TC tracks (Rohde 2006)

TCs in the Western Hemisphere are categorized according to the maximum one-minute averaged wind speed (or "maximum sustained wind speed") via the Saffir Simpson scale (Simpson 1974). To be classified as a hurricane, a TC must have a maximum sustained wind speed of at least 74 mph. The most intense storms, with maximum wind speeds of more than 155

mph, are Category-5 storms. When possible, storm intensity is established through wind speed measurements from either satellite or the Hurricane Hunter airplanes. When these are not available, storm intensity is estimated via the Dvorak method (Velden et al. 2006) which estimates the intensity via cloud patterns and features. This method has been frequently used in the past 40 years due to the ready availability of satellite imagery of cloud cover and to its simplicity, practicality, and "demonstrated skill in the face of tremendous dynamic complexity" (Velden et al. 2006).

Though the Saffir Simpson scale has been used since the 1970s to classify hurricane strength and guide public perception of the dangers of a landfalling storm, there have been many arguments that this is not the best way to quantify the threat that a storm poses at landfall. Most damage from TCs is due to storm surge and flooding which can occur without Category-5 winds (Rappaport 2014). For example, Hurricane Sandy struck the east coast of the United States in 2011. Flooding devasted New York and the storm caused almost $70 billion in damages despite the storm being extra tropical with winds of only Category-1 strength. It is argued that reporting a Category-1 storm gives the public a false sense that the storm is not dangerous. A more useful indicator for the public would capture the full destructive potential of a storm, which is a function of wind speed, but also rain rate, storm size, storm motion, and landfall location. One proposed metric is integrated kinetic energy which accounts for the storm size as well as the wind speed (Powell and Reinhold 2007). This still does not account for rainfall or the susceptibility of the coast to storm surge, however. The Extreme Rain Multiplier (ERM), defined as the ratio of the expected TC rainfall to the climatologically derived 2-year rainfall, is gaining popularity as a TC rainfall risk metric (Bosma et al. 2020). ERM is easier for the public to interpret because it is normalized by the magnitude of a rainfall event that is typically

experienced in that location. It remains to be seen if ERM will have a lasting or significant impact on quantifying destructive potential of TCs. Despite many attempts to replace the Saffir Simpson scale and its imperfections, it remains the most common system for classifying the strength of hurricanes due to its simplicity and familiarity.

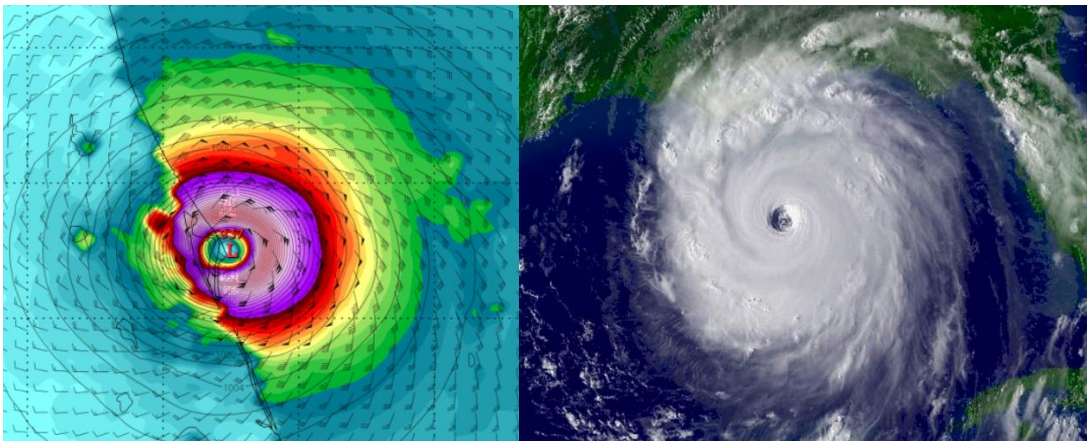

Figure 1-2: Typical TC structure in a model's wind field (left) and the clouds as seen from space (right). Note, these images represent different, arbitrary storms.

Well-organized TCs share common wind field characteristics (Figure 1-2). If the storm is more than about 5 degrees from the equator, the Coriolis force deflects the converging surface winds such that they never reach the center. Instead, the winds circulate counterclockwise (or clockwise in the southern hemisphere) around the storm. The center of the TC, or the eye, is left with only calm winds (though the ocean surface remains very rough). The eyewall, the location of the most intense convection and peak wind speed, Vm, is typically about $Rm = 50\ km$ from the center (though eyes tend to be larger in the Pacific than the Atlantic). The wind speeds radially decay between the eyewall and the edge of the storm which is typically defined by R34, or the maximum extent of the 34-knot contour line (1 knot = 0.514 m/s). The median R34 value is about 160 km in tropical storms (TCs below hurricane strength) and about 250 km in hurricanes (Landsea and Franklin 2013). Note that the strongest wind speeds are typically

located in the northeast quadrant for a northward-moving storm in the northern hemisphere because the winds are in the same direction as the overall motion of the storm. When TCs are weak (below hurricane strength), it is typical to see departures from this textbook wind field description. As TCs move north, they become larger (both in radially extent and in the size of the eye). At high latitudes (more than 35 degrees from the equator), the wind field can drastically change as the storm makes the extratropical transition (Vose et al. 2014).

Agencies such as the U.S. Joint Typhoon Warning Center and the National Hurricane Center (NHC) monitor TCs in the Pacific and Atlantic basins, respectively, and release forecasts and warnings to the public. They also keep an official data record of maximum sustained wind speed, central pressure, wind radii, storm center location, and more for each storm (Jarvinen, Neumann, and Davis 1984). These records are referred to as TCVitals and are produced in near-real-time (Trahan and Sparling 2012). After a post-season reanalysis of each storm using all available data, the data records are updated with improved estimates which are called Best Tracks (Landsea and Franklin 2013; Knapp et al. 2010).

TC agencies provide forecasts based on model output. For example, the National Oceanic and Atmospheric Administration (NOAA) Hurricane Weather Research and Forecasting (HWRF) model has been the operational backbone for TC track and intensity forecasts by the NHC since 2007 (Biswas et al. 2018). HWRF is initialized by measurements of the atmosphere and ocean. It propagates forward using a nested grid system and ocean-atmosphere coupling (Yablonsky et al. 2015). The inner nest, which is centered on a TC and only available near the storm, has the finest horizontal resolution of about 1.5 km. HWRF, like other models, struggles to forecast rapid intensification (Goldenberg et al. 2015). This is partially due to a lack of understanding of hurricane dynamics and the model resolution being too coarse to capture the

necessary features. The model is also limited by the accuracy of the initial conditions which are established by measurements from satellites, buoys, aircraft, and more. The number and accuracy of observing systems continues to increase, which improves initial conditions and, therefore, model performance.

1.1 Earth-Based Measurements of Tropical Cyclones

Earth-based measurements of TCs are primarily made via buoys, aircrafts, Doppler radar, and on-shore weather stations. Though local measurements are easier to make and are generally more reliable than space-based measurements, they are limited by availability.

Buoys measure ocean parameters like barometric pressure, wind speed and direction, air and sea temperature, and wave energy spectra. However, most buoys are positioned near the coasts, which leaves large gaps in the middle of the ocean (Teng 2010). This is mostly due to the fact that buoys are difficult to maintain far from land, and even more so in large numbers. The buoy network is not expansive enough to consistently provide measurements for most TCs, and it certainly cannot provide routine measurements to show storm evolution. Buoy measurements are reliable, however, and provide valuable in-situ “truth” comparisons for measurements made from space.

Figure 1-3: NOAA Hurricane Hunter WP-3D Orion "Kermit" (Photo by David R. Mayers, 2020, Lakeland, FL)

Aircraft reconnaissance from the NOAA Hurricane Hunters provides valuable storm information to assist with forecasting, record keeping, and scientific investigation. These WP-3D Orions (P3s), shown in Figure 1-3, are equipped with lower fuselage and tail Doppler radar systems. Together, these radars provide vertical and horizontal scans of the storm. They are also equipped with Step Frequency Microwave Radiometers (SFMRs) which can measure near-surface wind speed and column-averaged rain rate (Uhlhorn et al. 2007). SFMR, a downward looking radiometer, estimates ocean surface brightness temperature at six frequencies between 4.6 and 7.2 GHz. Wind speeds are calculated by assuming a linear increase in wind speed with brightness temperature. Because the amount of attenuation is a function of frequency, rain rate can also be estimated. P3 crewmembers also drop expendable probes called dropsondes through a launch tube in the aircraft. As they parachute to the sea below, the probes transmit pressure, temperature, humidity, wind speed, and wind direction data back to the aircraft (NOAA 2017).

Aircraft recon provides reliable real-time measurements of the storm system in higher resolution than most space-based measurements. The P3 aircraft also has the advantage of choosing which location (in both altitude and latitude/longitude) to examine and when to deploy the aircraft to the storm. In this way, crucial measurements can be made of storms threatening landfall to the United States. These measurements are used to alert the public to the intensity of the storm and to better predict the storm's future intensity. However, like other Earth-based measurements, these planes are very limited in number and are mostly limited to storms that are threatening land in the Atlantic basin. For these reasons, coverage is very limited and space-based measurements are often the primary source of information.

When TCs are at or near landfall, Doppler radar and weather stations can make measurements of the storm as well. Doppler radar provides information on both the vertical and

horizontal structure of the storm while weather stations give point measurements of wind, temperature, pressure, humidity, and more. These are valuable measurements, but again, they are limited by opportunity. These measurements are only available near land, so they typically cannot be used to forecast storm track, intensity, or rainfall.

1.2 Satellite Measurements of Tropical Cyclones

Spaceborne remote sensing is an excellent way to provide consistent measurements of TCs, especially when in locations that make Earth-based measurements difficult or sparse. Visible, microwave, and infrared satellite imagery is often used to locate the TC storm center (Wimmers and Velden 2016) and to direct aircraft recon. Cloud patterns found in the images, along with satellite-measured cloud-top temperatures related to the depth of convection, are used to determine TC intensity when direct observations are not available (Velden et al. 2006). Ocean temperature, salinity, wind speed, wind direction, rain rate, and more can be determined from satellite platforms in all weather conditions. These measurements are used in TC forecasting, TC record-keeping, and many more applications outside of tropical meteorology. The focus of this dissertation, ocean surface wind speed, is primarily measured through two classes of instruments: scatterometers and radiometers.

Scatterometer technology has been used to measure ocean surface wind speed and direction since Seasat was launched in 1978 (Wentz, Mattox, and Peteherych 1986). Since then, many scatterometers have flown such as ASCAT (C band, 5.25 GHz, 5.7 cm, ~25 km resolution; Figa-Saldaña et al., 2002), QuikSCAT (Ku band, 13.4 GHz, 2.2 cm, ~25 km resolution; Draper & Long, 2002), and RapidScat (Ku band, 13.4 GHz, 2.2 cm, ~20 km resolution; Durden & Perkovic-Martin, 2017). Scatterometers are active instruments with a precisely determined

antenna pattern for both transmission and reception. They transmit a signal toward the surface and use the back-scattered power to determine wind speed and direction. When the sea surface waves have a wavelength λ_s such that the backscattered radar signals (wavelength λ_r) add in phase, Bragg resonance occurs and becomes the dominant contribution to the backscatter (Figure 1-4). Scatterometers typically operate at microwave frequencies with wavelengths between 2 cm and 6 cm. Scatterometers are most sensitive to ocean waves similarly sized to the radar wavelength; predominantly centimeter capillary waves which are driven by the local wind. For this reason, scatterometers measure the local wind and are not biased by the large swell generated by distant winds (Hilburn et al. 2006). As the local wind speed increases, the ocean roughens at the Bragg wavelength and the amount of backscatter increases. Wind speed can be determined in this way. By looking at the same part of the surface from different azimuth angles, wind direction can be determined as well. It is worth noting that C band and Ku band are attenuated and scattered by rain drops (Ku band more so than C band), and scatterometers also suffer from reduced performance in rain due to outflow from storms and the "splash effect" of raindrops roughening the ocean surface (Hilburn et al. 2006; Portabella et al. 2012; Stiles and Yueh 2002; Weissman and Bourassa 2008). Also, many scatterometers saturate at wind speeds above ~30 m/s (Donelan et al. 2004; Hwang et al. 2013), though cross-polarization scatterometers have recently been shown to retain sensitivity to high wind speeds (Mouche et al. 2017).

Another class of ocean wind speed instrument, the radiometer, passively measures thermal emission from the surface. At microwave frequencies, the emission from the ocean depends on the sea temperature, salinity, and dielectric properties. Sea foam, which forms on the surface from the surface winds, has distinct dielectric properties. The amount of sea foam

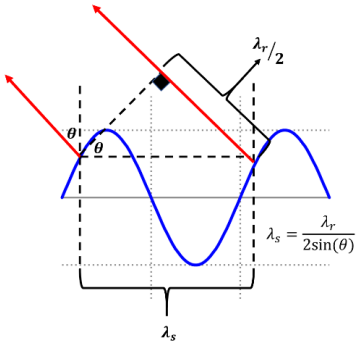

Figure 1-4: Bragg resonance mechanism which dominates the backscatter of scatterometers

increases nearly linearly with wind speed and does not saturate; this allows for radiometers to maintain good sensitivity even at hurricane-force wind speeds (Meissner, Ricciadulli, and Wentz 2017). Radiometers operating at 21 cm, or L band, easily penetrate through rain. Examples include NASA's SMAP (Entekhabi et al. 2010), ESA's Soil Moisture and Ocean Salinity mission (Reul et al. 2012; Kerr et al. 2010), and NASA's Aquarius (Lagerloef et al. 2008; Meissner, Wentz, and Ricciardulli 2014). Radiometers operating at higher frequencies face attenuation due to rain. This includes the Japan Aerospace Exploration Agency's Advanced Microwave Scanning Radiometer (AMSR2; C band, 35x62 km resolution; Zabolotskikh et al., 2016) and WindSat (6.8, 10.7, 18.7, 23.8, and 37.0 GHz, ~30 km resolution; Gaiser et al., 2004). Note that all-weather wind retrievals are possible at C band by using multiple channels at C or X band to remove rain contamination that is present in each individual channel (Meissner and Wentz 2009; Zabolotskikh et al. 2015).

1.3 CYGNSS

The Cyclone Global Navigation Satellite System (CYGNSS) is a NASA satellite mission to improve intensity forecasts of TCs by measuring ocean surface wind speed near the inner core of the storm. Surface winds are the primary mechanism for transferring moisture from the ocean

to the atmosphere and drive the intensity of the storm (Green and Zhang 2013). Accurate measurements of ocean surface winds, together with temperature and moisture fluxes, are crucial to the forecasting of TCs.

The improvement in TC track forecasting in recent decades is one of the great success stories in the field of meteorology. Meanwhile, TC intensity forecasts have only marginally improved (DeMaria, Knaff, and Sampson 2007; Emanuel and Zhang 2016). Reliable forecasting of rapid intensification remains one of the greatest challenges. It is unsurprising that track forecasting is more skillful than intensity forecasting. TCs are steered by the regional winds in the upper atmosphere—a large scale effect which is relatively straightforward to predict. Accurate intensity forecasting requires proper modeling of the inner core structure, microphysical processes, air-sea exchanges, the ocean response, the interaction with land and the larger scale environment, and radiative effects (Y. Wang and Wu 2004). Some of these processes are small-scale which are not resolved in current models, in which case they are approximated via parametrizations. The small-scale processes behind intensification have limited forecast skill thus far. The motivating hypothesis for CYGNSS is that the limited improvement in intensity forecasting is largely due to a lack of observations and proper modeling of the TC inner core (Ruf et al. 2016). Prior to CYGNSS, many satellites capable of measuring wind in the inner core either do not have the temporal resolution to capture rapid intensification, or they cannot penetrate heavy rainfall to measure the core. In situ measurements by aircraft and dropsondes are limited in space and time. Limited observations of surface wind speeds in the most dynamically active portion of the TC leads to inaccuracies in the initial conditions of model forecasts and insufficient information for parametrization of convection and surface fluxes (Ruf et al. 2016). CYGNSS was designed to address these issues.

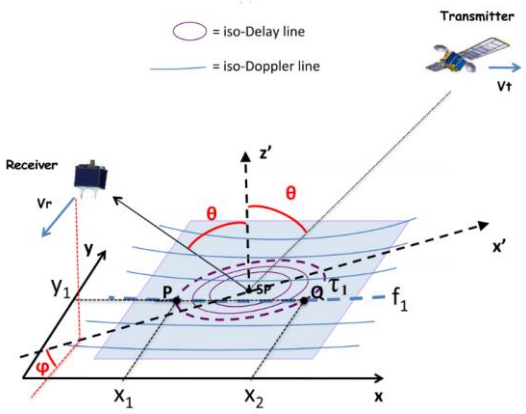

Figure 1-5: Bistatic geometry with iso-delay ellipses and iso-Doppler parabolas on the surface (Clarizia and Ruf 2016)

The CYGNSS constellation, launched on 15 December 2016, consists of 8 small satellites spread over a 520 km circular orbit at 35-degree inclination. This orbit angle allows CYGNSS to make measurements within +/- 38 degrees latitude, which is where the vast majority of TCs develop. The mean and median revisit times of 7.2 and 2.8 hours, respectively, give CYGNSS the opportunity to resolve the rapid intensification of TCs. The spatial resolution of CYGNSS measurements is about 25 km. CYGNSS receives Global Positioning System (GPS) signals reflected from the ocean surface (at L band or 1575.42 MHz). As the ocean roughens, the received power decreases since there is more power scattered in other directions. In this way, CYGNSS can determine ocean roughness which is related to wind speed.

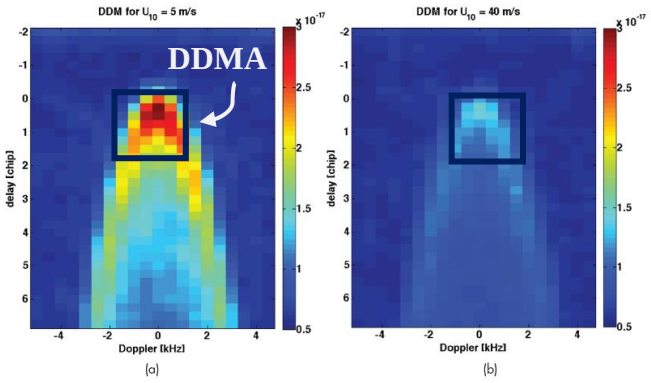

Figure 1-6: Delay Doppler Map (DDM) in different wind speed conditions (Ruf et al. 2016). The average value within the black box represents the Delay Doppler Map Average (DDMA) which is then related to wind speed.

The specular reflection point (SP in Figure 1-5) is defined as the point on the surface at which the angle of incidence and angle of reflection of the scattered signal are equal. It is also the point with the minimum travel time between transmitting GPS satellite and receiving CYGNSS satellite. Moving in any direction along the surface away from the specular point, there is increased travel time between transmitter and receiver (delay). This takes the form of iso-delay elliptical contours, as illustrated in Figure 1-5. Moving along the surface also changes the Doppler shift of the received signal. This results in iso-Doppler contours on the surface (parabolas in Figure 1-5). By scanning the 2-dimensional Delay-Doppler space, it is possible to map signal contributions to particular regions on the surface. This is made possible by the structure of the GPS signal. The Gold code, a sequence of 1023 bits repeating every 1 ms, is modulated on the carrier signal (Misra and Enge 2012). The autocorrelation of the received signal with a locally generated replica of the signal is very large when the 1023 bits are perfectly aligned, but if there is even a misalignment by one bit, the autocorrelation is nearly zero (orthogonality of the gold codes). By slightly adjusting the delay and Doppler of the local signal, it is possible to scan physical regions of the surface for scattering contributions (Gleason 2006). Figure 1-6 shows a Delay Doppler Map (DDM) which is the primary data product which is sent to the ground in normal operation (Ruf et al. 2016). Each grid cell contains the power determined through autocorrelation of the received signal with a locally generated signal of the given delay-Doppler combination. Note that the expected received power is determined from the CYGNSS zenith antenna which receives the direct signal from the GPS satellite (T. Wang et al. 2019) along with the radar equation and forward scattering model (Zavorotny and Voronovich 2000). The specular point is located in the cell where the power is highest. When the wind is weak and

the ocean is smooth, most of the power is from near the specular point. As the wind speed increases and the ocean roughens, there is less power from the specular point and more diffuse scattering contributions from other locations (right panel of Figure 1-6).

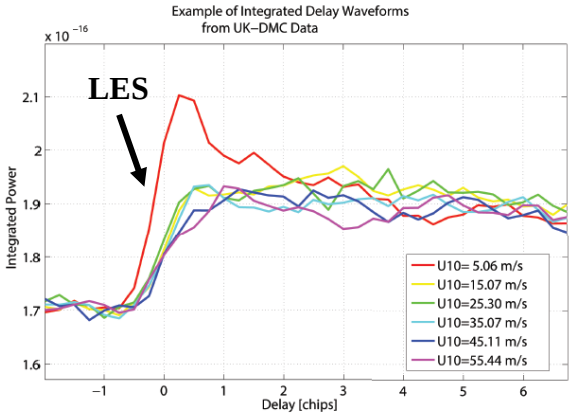

Figure 1-7: Integrating a DDM with respect to Doppler frequency results in an integrated delay waveform. Each waveform above is from a DDM of a different wind speed (see legend). The leading-edge slope (LES) is a primary observable which is related to near-surface wind speed through the geophysical model function (Ruf et al. 2016).

Two observables are used to determine wind speed: the delay-Doppler map average (DDMA) and the leading-edge slope (LES) (Clarizia and Ruf 2016). The DDMA is the average value within the black box on the DDM in Figure 1-6. This number, which represents the received power scattered from near the specular point, will decrease as the wind speed increases. The LES is the slope of the integrated delay waveform which results from integrating the DDM in Figure 1-6 with respect to Doppler frequency and considering it as a one-dimension function of time delay. Examples of these waveforms from DDMs at various wind speeds are shown in Figure 1-7. Both DDMA and LES are mapped to near-surface wind speed as a function of incidence angle through the empirically determined geophysical model function. The geophysical model function is determined by matchups of CYGNSS observables with "truth" wind speeds. At low wind speeds, numerical weather prediction models or reanalysis products such as ECMWF (European Centre for Medium-Range Weather Forecasts), MERRA-2

(Modern-Era Retrospective analysis for Research and Applications), and GDAS (Global Data Assimilation System) are matched up with CYGNSS observables to determine the geophysical model function as seen in Figure 1-8 (Ruf and Balasubramaniam 2019). Because these models are not very accurate at high wind speeds, the high wind speed matchups must include a different data source. In an old version of the geophysical model function (CYGNSS v2.1 data), the high wind speed mapping was determined through matchups of CYGNSS observables with stepped frequency microwave radiometer (SFMR) wind speed measurements in hurricanes (Ruf and Balasubramaniam 2019). SFMR is very limited in number of measurements and even more limited when only considering the measurements which coincide with a CYGNSS overpass. The most recent geophysical model function was determined through matchups of CYGNSS observables with HWRF model wind speeds in 2017 and 2018 hurricanes.

Using LES and DDMA to determine wind speed will result in two answers which both have a particular uncertainty. An improved wind speed estimate combines the two wind speeds using a minimum variance estimator which is essentially a weighted average with the weights determined by the inverse variance (Clarizia et al. 2014). This is done at low wind speeds. As wind speeds increase, LES loses sensitivity very quickly so only DDMA is used at high wind speeds.

The sensitivity of CYGNSS to wind speed is the derivative of the geophysical model function (Figure 1-8). At low wind speeds, a relatively large change in DDMA is needed to change the wind speed. This also means that a large error is needed to change the DDMA enough to cause a relatively significant error in wind speed. Because of this good sensitivity, CYGNSS wind speed measurements are very robust at low wind speeds and perform well; the wind speed uncertainty for retrievals below 20 m/s is 1.67 m/s which is within the CYGNSS baseline

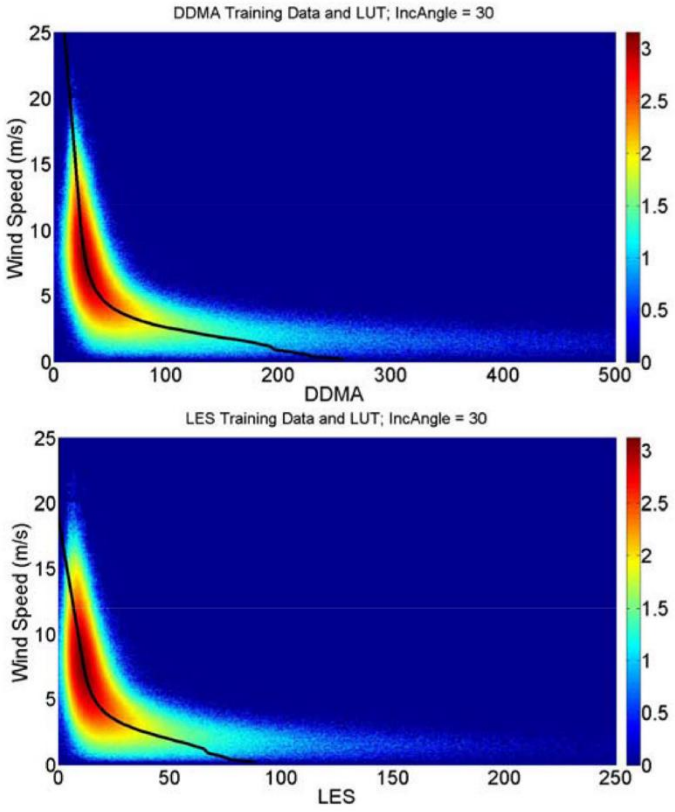

Figure 1-8: Matchups of model wind speeds against the CYGNSS observables for an incidence angle of 30 degrees. The best-fit black line is the empirically determined geophysical model function (Ruf and Balasubramaniam 2019).

mission requirements (Ruf et al. 2019). At wind speeds greater than 20 m/s, the CYGNSS retrieval uncertainty is about 11% of the retrieved wind speed which falls short of the mission requirements. At higher wind speeds, the slope of the geophysical model function becomes very flat; a very small change in DDMA causes a huge change in wind speed. This issue starts to appear above 15 m/s in Figure 1-8 and becomes much more prevalent for hurricane-force winds over 33 m/s (not shown in Figure 1-8). This makes measurements of hurricane-force wind speeds very susceptible to noise and other sources of error. Because of this loss of sensitivity at high wind speeds, CYGNSS struggles to differentiate a Category 1 from a Category 3 hurricane, or a Category 3 from a Category 5 hurricane.

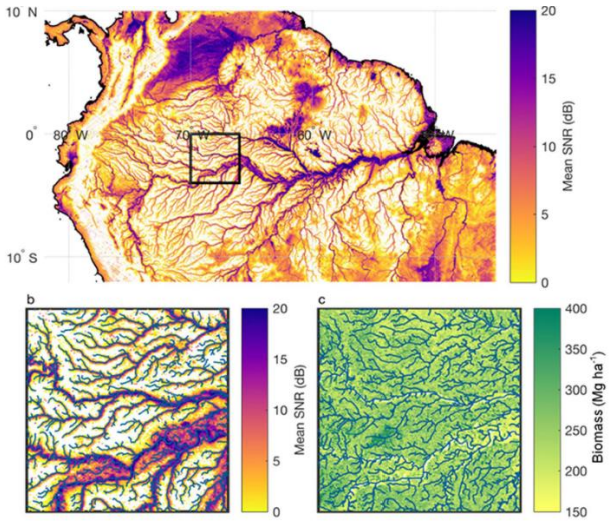

Figure 1-9: CYGNSS signal-to-noise ratio (SNR) identifies inland water (Ruf et al. 2018)

CYGNSS makes up for its shortcomings at high wind speeds by having many other uses over both ocean and land. CYGNSS is sensitive to soil moisture because the soil dielectric constant, and hence its reflectivity, is a function of the volumetric water content (Kim and Lakshmi 2018; Chew and Small 2018; 2020). The soil moisture retrieval algorithm is a function of the reflectivity (from CYGNSS) as well as the surface roughness and vegetation opacity (from ancillary sources) in order to isolate reflectivity's sensitivity to soil moisture. Soil moisture is an essential climate variable that is needed to predict runoff vs infiltration of rainfall, flooding, drought monitoring, agriculture yields, and more (Chew, Reager, and Small 2018; Kim and Lakshmi 2018; Senyurek et al. 2020; Clarizia et al. 2019). Long term monitoring of soil moisture is necessary for climate change studies. Similarly, the reflectivity changes with the phase of water in the soil. Water is much more reflective than ice so there is a stark difference when observing a frozen surface. This allows for CYGNSS to be used for freeze/thaw classification (Wu et al. 2020; Wu, Jin, and Ouyang 2020).

When the CYGNSS footprint contains a smooth water body, the reflected contributions from the water surface remain in phase (coherent reflection) and, therefore, dominate the received signal. Even a small body which only represents 1% of the footprint dominates the signal (Warnock and Ruf 2019). This property makes CYGNSS a very good detector of inland water bodies and flooding. For example, CYGNSS made multiple overpasses of Hurricane Harvey (2017) when it stalled over Taxes and unleashed as many as 60 inches of rain. The signal-to-noise ratio of the CYGNSS measurements reveals flood zones. The short revisit time of CYGNSS allows for these flood zones to be tracked in time (Morris et al. 2019). Also, because the coherent reflection is limited to the first Fresnel zone, the spatial resolution is very fine in these cases. This allows for the detection of very small water bodies (Figure 1-9) along with determination of river width and flowrate (Warnock and Ruf 2019; Chew, Reager, and Small 2018; Ruf et al. 2018).

CYGNSS has also shown promise for altimetry applications by looking at the delay between the direct and reflected signals and relating that to the system geometry. In this way, sea surface height and ice thickness can be determined (Li et al. 2020). Currently, the errors are too large to be useful. Satellites dedicated to altimetry have very precisely determined orbits, attitude control, and signals optimized for accurate timing. Because CYGNSS was not made for altimetry, there are large errors due to receiver positioning and precise delay determination (Mashburn et al. 2020). In a future Global Navigation Satellite System Reflectometry (GNSS-R) mission, there is potential for success in measuring relatively large objects with very good temporal resolution (especially compared to existing altimetry platforms).

Chapter 2 Estimating the True Maximum Sustained Wind Speed of a Tropical Cyclone from Spatially Averaged Observations

The maximum sustained wind speed (Vm) of a tropical cyclone (TC) observed by a sensor varies with its spatial resolution. If unaccounted for, the difference between the "true" and observed Vm results in an error in estimation of Vm. The magnitude of the error is found to depend on the radius of maximum wind speed (Rm) and Vm itself. Quantitative relationships are established between Vm estimation errors and the TC characteristics. A correction algorithm is constructed as a scale factor to estimate the "true" Vm from coarsely resolved wind speed measurements observed by satellites. Without the correction, estimates of Vm made directly from the observations have root-mean-squared differences (RMSD) of 1.77, 3.41, and 6.11 m/s given observations with a spatial resolution of 25, 40 and 70 km, respectively. When the proposed scale factors are applied to the observations, the errors are reduced to 0.69, 1.23, and 2.12 m/s. A demonstration of the application of the correction algorithm throughout the lifecycle of Hurricane Sergio in 2018 is also presented. It illustrates the value of having the scale factor depend on Rm and Vm, as opposed to using a fixed value, independent of TC characteristics. The material in this chapter is largely drawn from (Mayers and Ruf 2020).

2.1 Motivation

Spaceborne remote sensing is an excellent way to provide worldwide measurements of geophysical parameters, especially in remote locations. Satellite measurements are made at a variety of spatial resolutions which determines the smallest discernible feature. Spatial

resolution, defined as the diameter of the satellite footprint which contains the portion of the antenna pattern out to approximately -3 dB of the peak, is a function of antenna directivity, incidence angle, and the orbital radius. When measurements of the same scene at different resolutions are used to estimate a characteristic, how are they to be compared? This chapter examines this question for the case of measurements of ocean surface wind speed near a tropical cyclone (TC) which are used to estimate the maximum one-minute averaged wind speed ("maximum sustained wind speed" or Vm). Vm, the basis for the Saffir-Simpson Scale, is one of the primary metrics used to determine TC intensity (Simpson 1974). Scale factors are developed and used to estimate high-resolution Vm from low resolution wind speed measurements. The scale factor is shown to be a function of storm intensity as well as the size of the pocket of highest wind speeds (the radius of maximum winds will be used as a proxy for this). We examine the dependence of the scale factor on these two TC properties and consider what information about a TC is lost by measuring at low resolution.

The idea of converting TC intensity parameters between spatial scales is similar to gust factors which convert maximum sustained winds defined with respect to different temporal averaging intervals (e.g. between a 1- and 10-minute-averaged gust). Gust factor is a well-established and well-researched topic (Harper, Kepert, and Ginger 2010), but little detailed research has been done for a similar idea concerning spatial averages. Gust factor is dependent on numerous other inputs, including the roughness length (exposure), distance from an upstream terrain change, stability, height above sea level, and, potentially, the presence of convection (Paulsen and Schroeder 2005). Similarly, this paper investigates the various dependencies of a spatial scale factor for Vm.

Name	Class	Frequency	Spatial Resolution
ASCAT	Scatterometer	C band	25 km
QuikSCAT	Scatterometer	Ku band	25 km
RapidScat	Scatterometer	Ku band	20 km
CYGNSS	Bistatic radar	L band	25 km
SMAP	Radiometer	L band	40 km
SMOS	Radiometer	L band	45 km
Aquarius	Radiometer	L band	100 km
AMSR2	Radiometer	C band	50 km
WindSat	Radiometer	C/X band	35 km

Table 2-1: Examples of instruments that measure wind speeds at varying spatial resolutions.

The ideas presented in this work are relevant to remote sensing instruments which measure a spatially coarse wind speed and then attempt to estimate a "true" (i.e. very high resolution) TC parameter. These instruments could be scatterometers, radiometers, CYGNSS, or other types of satellites which are capable of measuring wind speed. Table 2-1 summarizes these satellites and their respective frequencies and spatial resolutions; these satellites typically have spatial resolutions ranging from 20 km to 50 km.

Although spatial resolution conversion hasn't been studied in detail, it has been acknowledged. Meissner et al. (2017), Reul et al. (2016), and Zabolotskikh et al. (2016) encountered issues with spatial resolution while comparing radiometer winds (SMAP, SMOS, and AMSR-2, respectively) to Best Track (Landsea and Franklin 2013) 1-minute maximum sustained winds. National Hurricane Center (NHC) Best Tracks are post-storm analyses of the intensity, position, and size of TCs and represent an official historical record for each storm. The reanalysis utilizes all available data for the storm, including data with high latency that was not available in near–real time for the original operational forecast. Vm was systematically underestimated as compared with Best Track. To improve the comparison, each of these papers utilize a 0.93 scale factor from (Harper, Kepert, and Ginger 2010). This is a gust factor which scales the 1-minute sustained winds from Best Track to a 10-minute sustained wind. Meissner

argues this is acceptable because of the way radiometers are sensitive to wind speed—they relate wind speed to the excess emissivity which is highly correlated with the roughness of the ocean. Meissner et al. (2017) argues that 10-minute sustained winds are required for the ocean surface to fully respond to the wind speed. One study (Reul et al. 2016) even admits that although the SMOS winds were calibrated using H*Wind 1-minute sustained wind speeds, the 10-minute sustained wind speeds compare better because of its coarse spatial resolution. They too applied the 0.93 gust factor. But satellite measurements of wind speed are nearly instantaneous in time and averaged spatially, so perhaps temporal scaling by the gust factor may not be appropriate. Instead, a scale factor is considered to relate Vm at coarse resolution to the high resolution Vm as reported by Best Track.

2.2 Dataset and Processing Methods

The Hurricane Weather Research and Forecasting (HWRF) system is an operational model implemented at the National Centers for Environmental Prediction (NCEP) of the National Weather Service (NWS) to provide numerical guidance to the National Hurricane Center (NHC) for the forecasting of tropical cyclone track, intensity, and structure (Biswas et al. 2018). This study will utilize HWRF wind fields from all storms in all basins in 2017 and 2018. HWRF has a parent and two nested domains. This study will use the innermost nest with the finest resolution. The inner nest domain covers about 5.9^o x 5.9^o centered on the storm with grid spacing of about 0.011^o (about 1.5 km). This study only uses the HWRF initialization (rather than including all wind fields which were propagated forward in time by the HWRF model) so that the study is less dependent on the characteristics of the HWRF simulation. HWRF is initialized by assimilating conventional observations, Tail Doppler Radar, satellite observations,

and Global Data Assimilation System (GDAS) 6-hourly forecasts. The HWRF data used in this study are the 10-meter wind speed along with the mean sea level pressure and the corresponding latitude and longitude of each grid point.

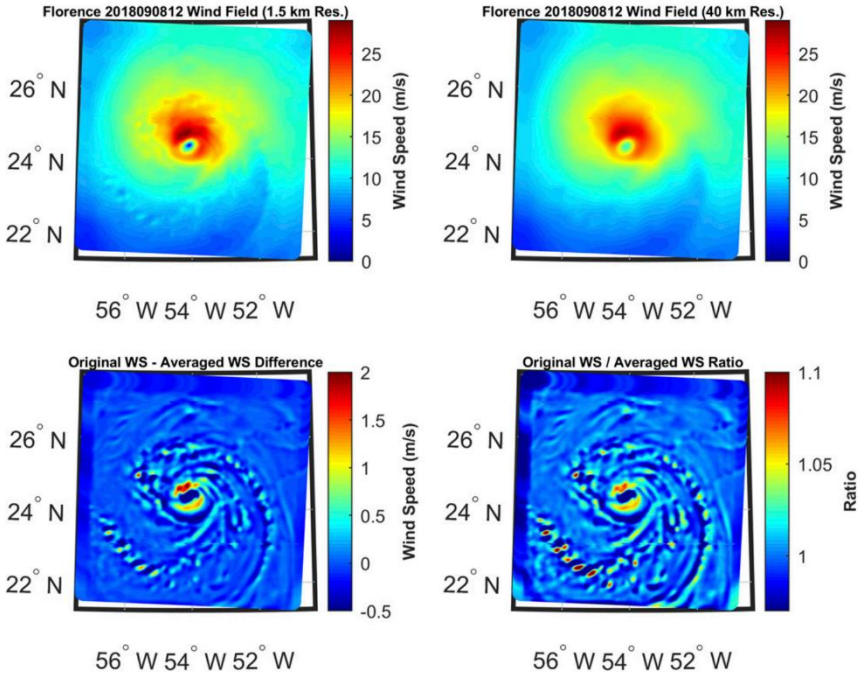

Figure 2-1: The effects of spatial averaging on a TC wind field. (top left) Image of a high-resolution wind field using HWRF inner-nest native resolution (1.5-km resolution). (top right) Image that is spatially averaged over 40 km and is equivalent to what a wind-measuring satellite with 40-km resolution would observe. Note how the lower resolution image loses the finer features that are present in the high-resolution image. (bottom left) The difference between the 40-km winds and the high-resolution winds. (bottom right) The ratio between the two wind fields in the top panels. The greatest differences occur around small-scale features such as the region of highest wind speeds, which is of particular interest for this paper.

The TC parameters used in this study are the maximum wind speed (Vm) and the radius of maximum wind speed (Rm). Vm is simply the 1-minute maximum sustained wind speed in the wind field (HWRF wind speeds are 1-minute wind speeds). Rm must be defined with respect to a storm center location. The storm center is established by identifying the point of minimum surface pressure. Rm is then calculated by averaging the distances to the ten grid points of highest wind speed surrounding the storm center position after removing all outliers. This is more robust than simply using the radial distance of the grid point with maximum wind speed.

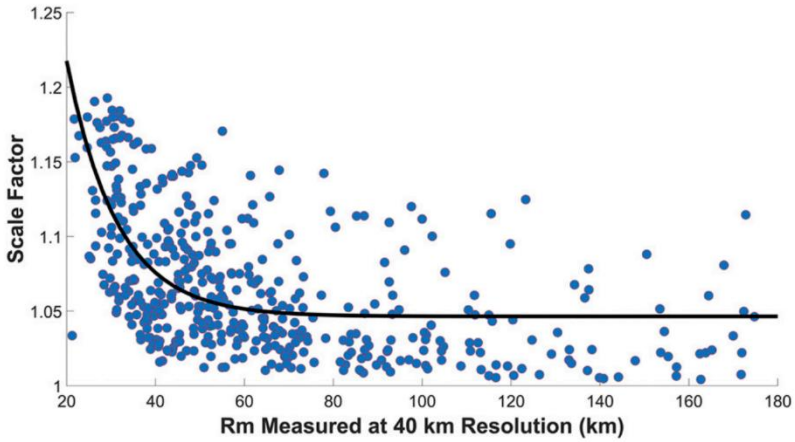

Figure 2-2: There is a strong dependence of SF on radius of maximum wind speed. When Rm is at or below the spatial resolution, the SF exponentially decays with Rm. Once Rm is significantly greater than the SF, the SF loses sensitivity to Rm.

To explore how resolution affects these TC parameters, spatial averaging is performed. The native HWRF resolution of 1.5 km is assumed to be fine enough to provide "true" Vm and Rm values. The reduced resolution cases which will be examined in this paper are 25 km, 40 km, 70 km, and 100 km. These values are representative of various spaceborne ocean wind sensors (Table 2-1). To simulate the effect of spatial averaging, a weighted average is done at each point in the wind field where weights are assigned according to the antenna pattern of the sensor. When the antenna pattern is not known, a Gaussian with standard deviation equal to the spatial resolution of the sensor is a good approximation. In this analysis, we use a simplifying approximation of a circle with diameter equal to the resolution. The results found in this paper will be slightly exaggerated compared to the exact antenna pattern due to a uniform average giving more weight to the outer part of the circle. An example of a spatially averaged wind field with 40 km resolution is shown in Figure 2-1. Note how the fine features of the wind field are lost due to spatial averaging, and the peak wind speed is reduced.

Storms near land are not included in this study. HWRF tends to produce pockets of anomalously high wind speeds on the windward side of the land feature. This can cause large

errors in wind radii and smaller, but significant, errors in Vm. For this reason, all cases with the inner nest within 20 km of land are not considered.

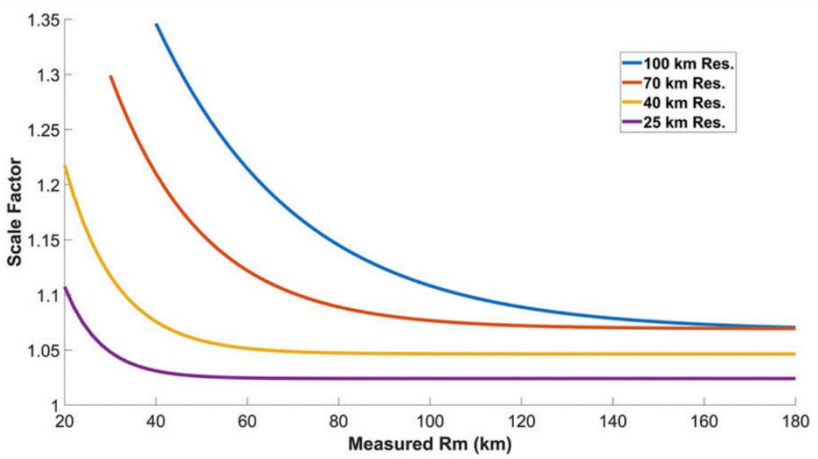

Figure 2-3: The SF varies with Rm for different spatial resolutions. For each spatial resolution, SF(Rm) follows the same general trend. When Rm is at or below the spatial resolution, SF exponentially decays with Rm. Once Rm is significantly greater than SF, SF loses sensitivity to Rm, which leads to an asymptote. Note that a coarser spatial resolution corresponds to a higher SF. Also note that SF(Rm) is not defined for Rm, 30 km at 70-km resolution and for Rm , 40 km at 100-km resolution. This is because, at coarse resolution, smaller storms become so washed out that Rm cannot be determined.

2.3 Scale Factor Dependencies

We define the scale factor SF for maximum sustained wind speed Vm as the ratio between the value when derived from HWRF inner nest wind speed data and the value when derived from spatially smoothed data at a coarser resolution. For example, the SF for spatially smoothed data with resolution *R* is given by

$$SF_R = \frac{Vm_0}{Vm_R} \quad (2.1)$$

where Vm_R is the maximum sustained wind speed value derived from the model data with spatial resolution of *R*, with Vm_0 indicating the native HWRF inner nest data value. Note that a SF close to unity indicates that Vm is not significantly impacted by spatial smoothing. When a SF deviates significantly from unity, Vm is impacted and will be estimated incorrectly from

smoothed data if no correction is made. This section examines which TC characteristics affect the SF and develops quantitative relationships to estimate Vm_0 from measurements made at coarser spatial resolution.

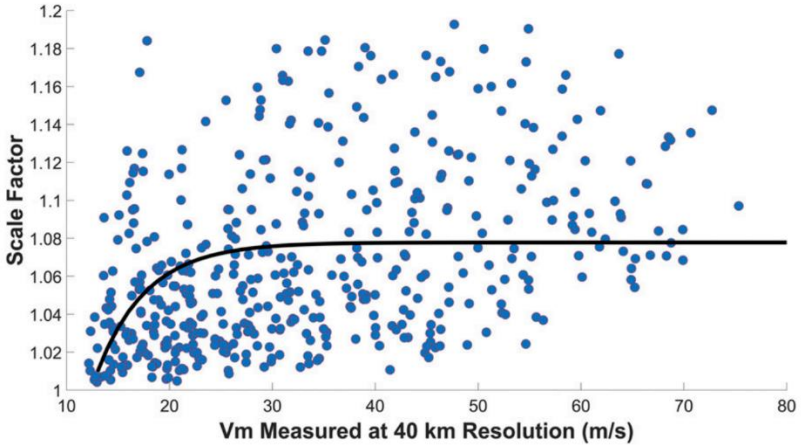

Figure 2-4: There is a weak dependence of the SF on the maximum sustained wind speed, but the general trend is noteworthy. When Vm is large, the storm is typically small and well-organized and is greatly affected by spatial averaging. When Vm is small, the storm is typically loosely organized and large and is not affected much by spatial averaging.

The relationship between the SF and the radius of maximum wind speed (Rm) is illustrated in Figure 2-2. The figure shows a population of values for SF derived empirically from individual HWRF storms, together with a parametric curve fit by least squares through the points. Keep in mind that Rm is being used as a proxy for the size of the high-wind core. The SF is largest when Rm is small because a smaller pocket of high winds is affected more by spatial averaging. SF changes rapidly with Rm until Rm is much larger than the spatial resolution, after which the SF is fairly insensitive to changes in Rm. For these reasons, we assume the following functional relationship

$$SF_R(Rm_R) = c + e^{-dRm_R} \qquad (2.2)$$

where *c* and *d* are tunable parameters. Least squares fits to the SF for 25, 40, 70, and 100 km resolution were performed and the resulting curves are displayed in Figure 2-3. SF can be seen to

exhibit similar behavior at all spatial resolutions. In each case, the sensitivity of SF to Rm decreases significantly when Rm is larger than the spatial resolution. Note that the measured Rm below 30 and 40 km is not well defined with 70 and 100 km resolution, respectively, because, with such small storms, very coarse resolution causes the maximum wind speed to lie at the storm center.

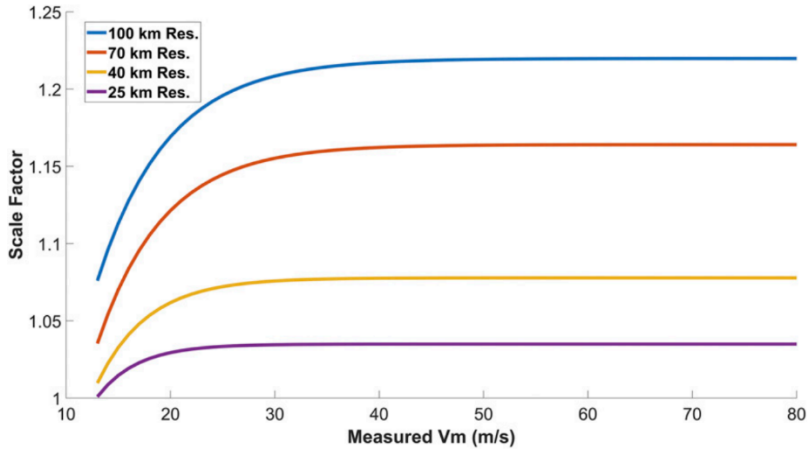

Figure 2-5: The SF varies with Vm at different spatial resolutions: SF increases as spatial resolution coarsens, it is large for high-intensity cases in which the storm is typically small and well-organized, and it is small for low-intensity cases in which the storm is typically large and disorganized with a large pocket of highest wind speeds.

The relationship between SF and Vm is shown in a similar manner to Figure 2-2 in Figure 2-4. SF can be seen to increase with Vm because Vm is correlated with storm size and organization. For example, when Vm is large, the TC tends to be intense and well-organized, with a small pocket of highest wind speeds. When Vm is small, storms tend to have a larger high wind speed area and are more loosely organized. Figure 2-4 demonstrates that SF depends strongly on Vm for weaker storms because this is where a relatively small change in Vm can drastically change the organization of the storm and, therefore, the size of the pocket of highest wind speeds. For large Vm, SF loses sensitivity to Vm. The behavior of the dependence suggests a parametric model of the form

$$SF_R(Vm_R) = a - e^{-bVm_R} \quad (2.3)$$

Figure 2-5 shows the resulting parametric model when fit to SF as a function of Vm with a spatial resolution of 25, 40, 70, and 100 km. The same general behavior is again found, with SF increasing as spatial resolution coarsens.

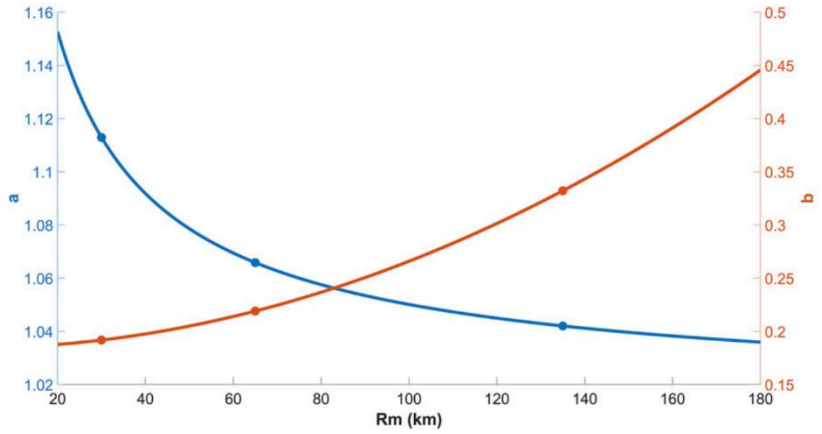

Figure 2-6: The dependence of the parameters *a* and *b* on *Rm* is used to extend the SF to three dimensions. Parameter *a* is the asymptotic value of SF and effectively shifts SF up and down; it decreases with *Rm* because, at larger *Rm*, the storm is less affected by averaging and therefore SF is small. Parameter *b* controls how quickly SF achieves its asymptotic value; it increases with *Rm*, suggesting that the asymptotic value of SF is reached more quickly for large storms. This is because *Vm* has little effect on SF when *Rm* is much larger than the spatial resolution.

The dependence of SF on *Vm* and *Rm* can be combined into a more general parametric model of the form

$$SF_R(Rm_R, Vm_R) = a(Rm_R) - e^{-b(Rm_R)Vm_R} \quad (2.4)$$

The dependence of *a* and *b* on Rm is determined by separating the dataset into Rm bins and fitting Eq. (2.3) to each group of data. A model of the form

$$a(Rm) = k(Rm^l) + m \quad (2.5)$$

is fit to each parameter (both *a* and *b*), with *k*, *l*, and *m* as constant real numbers. The resulting dependence of *a* and *b* on Rm is shown in Figure 2-6. *a* is the asymptotic value of the function and effectively shifts the scale factor up and down. *a* decreases with Rm because, at larger Rm,

the storm is less affected by averaging and therefore the SF is close to 1. *b* controls how quickly the SF achieves its asymptotic value. *b* increases with Rm, suggesting that the asymptotic value of SF is reached more quickly for storms with large high wind speed areas. This is because Vm has little effect on SF when Rm is much larger than the spatial resolution. These power series relations are used to generate a 3-D SF, which is shown in Figure 2-7 as a contour plot. The 3-D SF is maximized when Rm is small and Vm is large and SF is minimized when Rm is large and Vm is small.

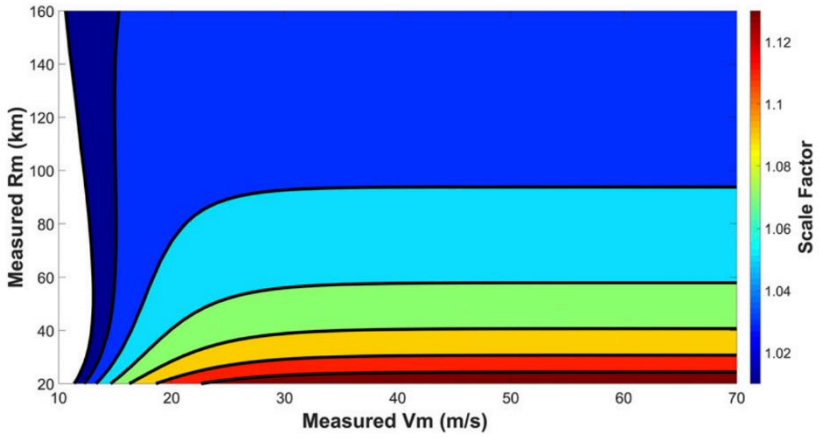

Figure 2-7: A slice of the three-dimensional SF at 40-km resolution, illustrating its dependence on Vm and Rm. The SF reaches a maximum value of 1.15 when Rm is small and Vm is large. The 3D SF combines trends seen previously in Figure 2-2 and Figure 2-4. The solid black lines indicate contours of constant SF.

The parametric relationships can be used in a correction algorithm to estimate Vm_0 from coarse measurements of the wind field. In practice, when a satellite measures the wind field of a TC at spatial resolution R, estimates of the parameters Vm_R and Rm_R can be produced directly from the measurements. Using Rm_R and/or Vm_R as inputs to the correction algorithm, the appropriate value for SF is determined. This SF corrects, or scales, the measured Vm_R to provide a better estimate of the true Vm_0. This procedure has been performed for all storms in the Atlantic, East Pacific, and West Pacific basins from 2017 and 2018. Half of the cases are randomly chosen as the training set for the parametric model. The other half are used to evaluate

Dependence	Equation no.	Resolution			
		25 km	40 km	70 km	100 km
No Correction	—	1.77	3.41	6.12	6.61
Constant	—	0.87	1.61	2.80	2.90
Vm	(3)	0.83	1.57	2.66	2.72
LMS Rm, Vm	—	0.74	1.33	2.26	—
Rm	(2)	0.75	1.28	2.16	—
Rm, Vm	(4)	0.69	1.23	2.12	—

Table 2-2: The root-mean-square difference in wind speed (m/s) between true and measured Vm with varying types of correction applied to the measured Vm, for different spatial resolution of the measurements. Cases considered are no correction, a constant SF for a particular spatial resolution, and SF corrections that depend on Vm, Rm, and both Vm and Rm. The ‘‘LMS Rm, Vm’’ row shows the results with Vm dependence for three different sizes of Rm: large, medium, and small.

the performance of the correction. The root-mean-squared difference (RMSD) between the true Vm_0 and the Vm_0 estimated from spatially smoothed measurements are summarized in Table 2-2. The first row of the table states the RMSD if no correction is made (i.e., using a SF of unity). As noted above, errors are larger with coarser spatial resolution. The second row is the RMSD for the simplest correction method—applying a constant SF, as in Eq (2.1), which is derived for a particular spatial resolution but does not depend on Rm, Vm, or any other parameter. Use of a constant SF does reduce the RMSD significantly, so it is much better than no correction. The remaining lines of Table 2 report RMSD values produced when more sophisticated versions of the SF correction are used which depend on properties of the storm that are directly measurable at the coarser resolution. Of the correction algorithms which depend on only one storm property, the one dependent on Rm performs best. This suggests that storm size is more highly correlated with changes in SF than is storm intensity. A better correction yet uses both Rm and Vm to estimate SF. For this correction method, the resulting RMSD values are listed in the last row of Table 2-2. It effectively combines both dependencies shown in Figure 2-2 and Figure 2-4. The RMSD values are 0.69, 1.23, and 2.12 m/s for 25, 40, and 70 km, respectively. Note that results requiring Rm as input are not listed for 100 km spatial resolution

because many of the individual cases have Rm values of zero due to significant averaging of the wind field. In such cases (e.g. in the case of Aquarius measurements of the wind field) (Meissner, Wentz, and Ricciardulli 2014), some other SF dependence should be considered, such as only Vm.

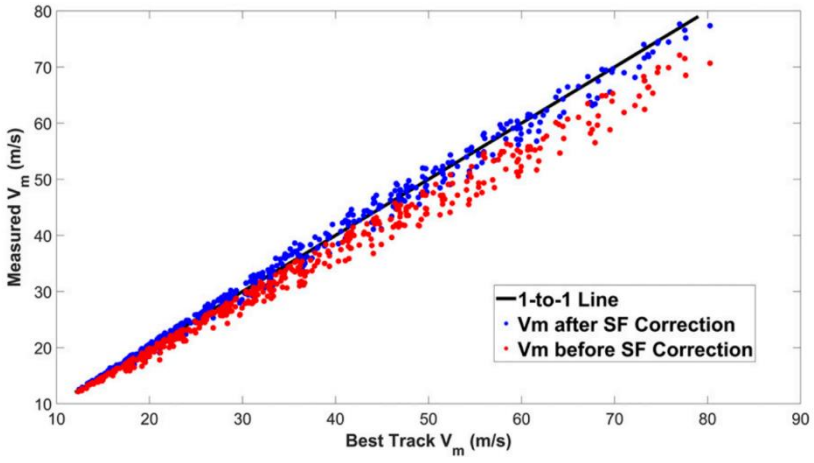

Figure 2-8: Comparison of best-track Vm with the Vm measured at 40-km spatial resolution. The red dots (before SF correction) consistently underestimate Vm. The blue dots (after SF correction) are shifted up toward the 1-to-1 line (a perfect estimate). Note the increased scatter at higher Vm. Also note that only the test cases are plotted here. None of the training cases were included in this figure.

The effect of the correction SF(Rm,Vm) is visualized in Figure 2-8. The red dots are the Best Track Vm values matched up with Vm measured by a 40 km resolution instrument (note this figure only includes the test cases—not the cases which were used to train the SF surface). These matchups typically remain under the 1-to-1 line because Vm is underestimated without a SF correction. The blue dots, the matchups after SF correction, are much closer to the 1-to-1 line. This figure shows the necessity of SF correction when estimating Vm from coarse resolution measurements. Figure 2-8 also demonstrates increased scatter at high winds. The RMS error between the Best Track Vm and the Vm estimated from 40 km wind speed measurements is 0.65, 1.42, and 1.91 m/s for Best Track Vm below 30 m/s, between 30 and 45 m/s, and greater than 45 m/s, respectively. The error increases as storm intensity increases as seen in Figure 2-8.

Similarly, the RMS error at 40 km resolution is 1.63, 1.12, and 0.69 m/s for Best Track Rm less than 50 km, between 50 and 85 km, and greater than 85 km, respectively.

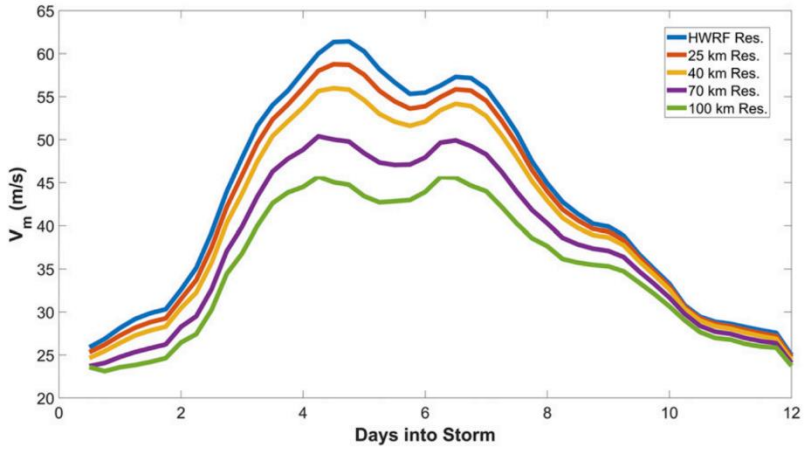

Figure 2-9: Maximum sustained wind speed observed at different spatial resolutions throughout the lifetime of Hurricane Sergio, a major hurricane in the eastern Pacific basin (2018). The wide range of observed Vm values allows for analysis of the performance of the SF correction in different situations. Note that Vm strictly decreases as the spatial resolution coarsens.

The radius of maximum wind speed, Rm, is shown to be strongly correlated with the scale factor correction. However, it is worth mentioning the deficiencies of using Rm as input in the correction algorithm. First, Rm is not included in the set of TC parameters in the Best Tracks (because Rm is primarily used to initialize models). Second, it is difficult to estimate Rm from an observed wind field that is fraught with noise and sampling gaps. This task becomes even more difficult when considering that a reliable estimate of Rm requires both an accurate storm center location and an accurate maximum wind speed location. The uncertainties of Best Track storm center locations are about 65 km, 40 km, and 27 km for tropical storms, Category 2 storms, and Category 4/5 storms, respectively (Torn and Snyder 2012). The combination of this storm center uncertainty with the uncertainty in maximum wind speed location makes estimating Rm difficult.

Despite these drawbacks, it's clear that the SF correction has improved performance when using Rm as input because Rm contains so much information about the size of the high-wind

speed core. When a precise estimate of Rm is not available, it's still best to use as much information as possible about the size of the pocket of highest wind speeds in the SF correction algorithm. To demonstrate this, we divide the population of storms into three groups of Rm: large, medium, and small. We define large Rm as Rm > 80 km, small Rm as Rm < 45 km, and medium Rm as everything in between. Each of these three groups has a different SF curve which depends on Vm. The training set determines these curves, then the resulting SF is evaluated on the test set. The resulting test set errors, shown in Table 2-2, are comparable in performance with the SF correction methods which depend on a precise value of Rm, and perform much better than the SF correction which depends only on Vm. Performance degrades when Rm is not known, but even coarse knowledge of the size of the high-wind speed core greatly improves SF performance and, therefore, estimation of a storm's maximum wind speed.

2.4 Hurricane Sergio Example

Use of the scale factor is demonstrated with East Pacific Hurricane Sergio throughout its lifecycle in 2018. The storm was chosen because it remained over open ocean for the bulk of its lifetime, which allows for a continuous analysis and no interference from land. Hurricane Sergio also went through a wide range of sizes and intensities, which provides the opportunity to examine SF performance in many different circumstances.

Figure 2-9 contains Vm estimates over the lifetime of the storm derived from HWRF winds averaged to various spatial resolutions. Note that Vm always decreases as spatial resolution becomes coarser. Also note that the ratio between the blue line (Vm at HWRF inner

nest native resolution) and the other lines (Vm at coarser resolutions) represents the exact SFs which would be needed for perfect correction of Vm to account for averaging of the TC wind

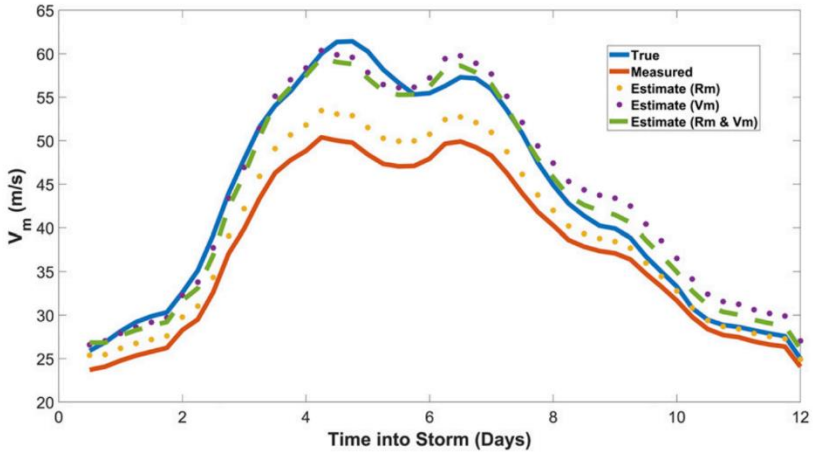

Figure 2-10: The solid blue line is the true Vm over the lifetime of Hurricane Sergio. The solid orange line is Vm after averaging the wind field down from 1.5-km resolution to 70-km resolution. The other three lines are different estimates of Vm. The purple dotted line estimates Vm by applying an SF that is a function only of Vm. The yellow dotted line estimates Vm using an SF that is a function only of Rm. The dashed green line estimates Vm using an SF that is a function only of both Rm and Vm. This last estimation technique performs best.

field. Estimates of these SFs are generated using the parametric model described above. Results are shown in Figure 2-10 for 70 km resolution. The solid lines represent Vm at 1.5 km and 70 km resolution. There is a wide gap between the two lines. Three different scale factors are applied to the 70 km estimate: 1) SF(Vm) is the purple dotted line; 2) SF(Rm) is the yellow dotted line; and 3) SF(Rm,Vm) is the green dashed line. Note that SF(Rm,Vm) provides the best correction (error of 1.43 m/s). SF(Rm) (error of 4.23 m/s) performs worse than SF(Vm) (error of 2.11 m/s), although the cumulative error analysis in the previous section showed that SF(Rm) typically outperforms SF(Vm). This discrepancy is due to the fact that Hurricane Sergio is more intense than the average TC. SF(Rm) is averaged across all Vm, so it performs the best when Vm is near its average value. Because Hurricane Sergio is a more intense storm, SF(Rm) tends to

underestimate Vm. In the later part of the storm, however, SF(Rm) performs well while SF(Vm) overestimates Vm. This is in part due to Vm becoming closer to average as the storm weakens.

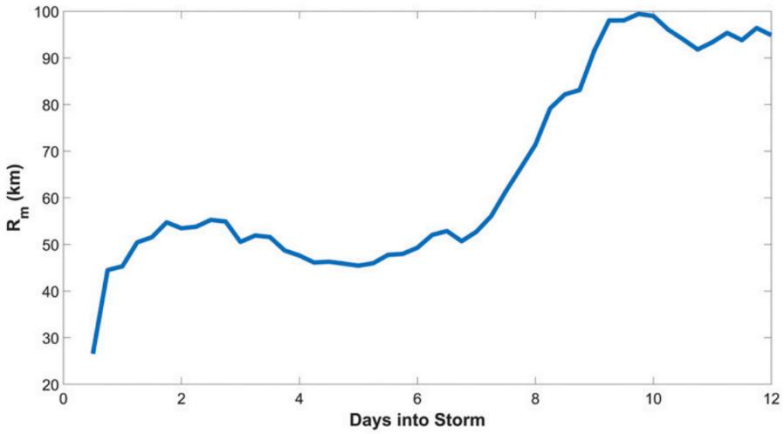

Figure 2-11: The radius of maximum wind speed for Hurricane Sergio derived from the wind field at HWRF native resolution. The Rm becomes very large toward the end of the storm, which causes large errors in the estimation of Vm when the SF is not a function of Rm.

The radius of maximum winds estimated at different spatial resolutions is shown in Figure 2-11 over the lifetime of Hurricane Sergio. In the later part of the storm, Rm is very large (near 100 km). When Rm is this large, the SF should be close to unity, but SF(Vm) does not account for storm size and overestimates Vm. Both SF(Rm) and SF(Vm,Rm) are able to give a better estimate of Vm during this stage of the storm than SF(Vm). Because SF(Vm,Rm) combines the strengths of SF(Rm) and SF(Vm), it performs well in all circumstances experienced with Hurricane Sergio.

2.5 Discussion and Implications

This work examines the effects of spatial averaging on a TC wind field and, consequently, on the maximum sustained wind speed (Vm) estimated from the smoothed

observations. Estimation of the true Vm from coarse wind measurements is improved by multiplication of the observed Vm by a Scale Factor (SF) that is greater than unity. The optimal SF is found to depend on TC parameters Vm and Rm, with the strongest dependence on Rm. Rm works well as input to the SF correction because it operates as a proxy for the size of the high-wind speed core.

The mean SF (with dependence on both Vm and Rm) across all test cases is 1.03, 1.07, 1.14, and 1.18 for spatial resolutions of 25, 40, 70, and 100 km, respectively. The gust factor conversion between a 1-minute averaged gust and a 10-minute averaged gust is 1.07 (Harper, Kepert, and Ginger 2010). This suggests that, on average, spatial smoothing over a 40 km area is roughly consistent with temporal averaging over 10 minutes in terms of their impact on Vm.

Note that the TC parameters used as input are those observed with coarse spatial resolution, so the implementation of this SF-based correction would be straightforward. When Rm is less than or equal to the spatial resolution of the measurements, SF decreases as Rm increases. When Rm is much greater than the spatial resolution, SF loses its dependence on Rm because the high wind speed region becomes large enough that the spatial averaging has negligible impact on Vm. SF, while not as dependent on Vm as Rm, increases as Vm increases. This is because intense storms tend to be small and are more affected by spatial averaging.

Application of the SF correction throughout the lifecycle of Hurricane Sergio is used to illustrate how inclusion of the dependencies on Rm and Vm improves the accuracy of the correction. When Hurricane Sergio is a major hurricane, inclusion of a Vm dependent SF prevents significant underestimation of the true Vm. When the high wind speed region of Hurricane Sergio becomes very large (Rm ~ 100 km), inclusion of an Rm dependent SF prevents a significant overestimation of the true Vm.

An additional strategy is implemented to demonstrate that precise knowledge of Rm is not necessary for the SF correction to improve Vm estimated from coarse satellite measurements. Storms are classified as having a large, medium, or small high-wind speed core, and each of these three classes has a different SF correction which is dependent on Vm. Even with using these rough estimates of Rm, there is significant improvement over both a constant SF and SF(Vm). The best SF correction uses as much information as possible about the size of Rm, or the high-wind core, but even a rough estimate of Rm can greatly improve results.

Chapter 3 Parametric Wind Speed Model: Complete Tropical Cyclone Wind Field from Sparse Measurements

Oftentimes, a TC wind field is only partially measured by an observing platform. For example, CYGNSS measures near-surface wind speed in pseudo-randomly oriented "tracks". A track is identified by a combination of one CYGNSS satellite and one GPS satellite. As these satellites move, the specular point traces out a track of measurements on the Earth's surface. A typical CYGNSS overpass of a TC looks like Figure 3-1, but the sample density and distribution vary with each overpass. While these incomplete wind speed measurements in the TC provide useful information for forecasting, some applications require a full TC wind field.

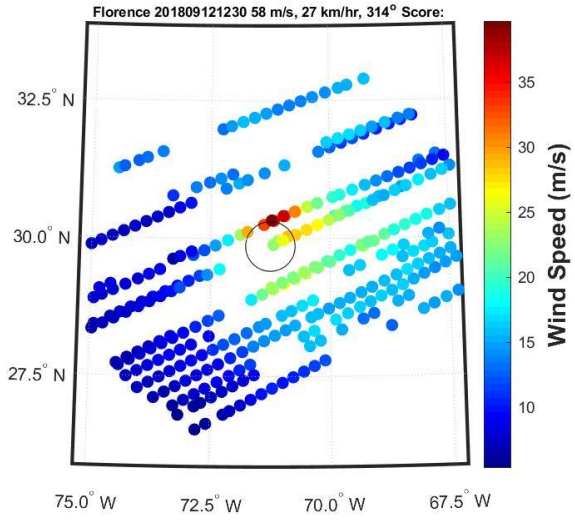

Figure 3-1: A typical CYGNSS overpass of a TC (3 hours of measurements)

The Best Tracks, U.S. National Hurricane Center's official historical record of TCs (Jarvinen, Neumann, and Davis 1984; Knapp et al. 2010), include only a few parameters that characterize the structure of the surface winds: the maximum sustained wind speed (Vm), the

radius of maximum wind speed (Rm), and the wind radii (R34, R50, and R64 corresponding to the radius of the smallest circle needed to enclose all wind speeds above 34, 50, and 64 knots, respectively). The Best Tracks are widely used in verification of model predictions of track and intensity, development of forecasting techniques, setting building codes of coastal zones, risk assessment for emergency managers and insurance interests, and climate change studies (Landsea and Franklin 2013). Given the widespread use of the Best Tracks and these TC wind field parameters, it is important that they are estimated as accurately as possible. However, these TC parameters can only be determined if a full wind field is available.

The integrated kinetic energy (IKE) of a TC is a metric which is sometimes used to quantify the damage potential of a storm (Morris and Ruf 2017b). IKE is computed by integrating over the square of the wind speed field. It is an improved estimate of the storm's threat to land because it captures both the storm's intensity (in terms of peak wind speed) and the storm's size. Again, it is not possible to calculate the IKE of a storm without an estimate of the surface wind speed everywhere in the storm.

Assimilation of the CYGNSS wind speed data is ongoing to determine if and to what degree the CYGNSS measurements have a positive impact on TC forecasts (Cui et al. 2019). For example, to examine how the addition of CYGNSS wind speed measurements affects a TC storm surge forecast, the Advanced Circulation 2-Dimension Depth Integrated model (ADCIRC-2DDI) is used and requires a full near-surface wind field to force the waves and simulate the surge (Warnock, Ruf, and Morris 2017). This work and others are not possible with measurements of only a portion of the wind field. For CYGNSS measurements to be used in these applications, there must be a way to estimate a complete TC wind field from the scattered CYGNSS measurements. A TC parametric wind speed model makes this possible.

3.1 Overview of Existing Parametric Wind Models

A TC parametric wind speed model defines the surface wind speed everywhere as a function of a few tunable parameters. The best-fit parameters are the set of parameters which minimizes a particular cost function. One cost function is the sum of the squared wind speed differences

$$f = \sum_{i=1}^{N} (v_i - \hat{v}_i)^2 \tag{3.1}$$

where v_i is the measured surface wind speed at a location and $\hat{v}_i$ is the wind speed estimated by the parametric model at the same location. A location in a storm is referenced by its polar coordinates, r_i and ϕ_i, which are the distance from the storm center and azimuth angle from north, respectively, for the ith sample. By minimizing the cost function, wind speed measurements can be used to tune the parametric wind model. The best-fit parameters are used to generate a full, gap-free TC wind field from the incomplete measurements which enables the applications discussed in the previous section.

Parametric wind speed models for TCs are developed from meteorological relationships combined with simplifying assumptions. One of the most popular models (Holland 1980) approximates the radial surface pressure profile $p(r)$ as a rectangular hyperbola then substitutes the result into the cyclostrophic wind equations (cyclostrophic wind balances the pressure gradient force with the centrifugal force). This model contains three free parameters and has been used extensively (Holland, Belanger, and Fritz 2010). Another model (Willoughby, Darling, and Rahn 2006) takes a piecewise approach; instead of attempting to model the full wind profile with one continuous function, three piecewise functions are used to describe different regions of the storm more accurately. These equations are common mathematical

functions that were chosen because they resemble a typical TC wind profile—they were not derived from physical principles. Another model (Emanuel 2010) acknowledges that the wind structure is determined by different mechanisms in different regions. The inner region is described by equations resulting from a balance of sinking air (subsidence) in the eye and inward diffusion of angular velocity from the eyewall. The wind profile of the outer region is determined by thermal wind balance and assumptions about the boundary layer entropy. The wind profiles of these two regions are extended asymptotically and patched together to form one equation to describe the full wind profile. Then an assumption of a critical Richardson Number is made to reduce the equation to only two parameters.

A study comparing the performance of these three models for a variety of TCs found that the model by Emanuel (Emanuel 2010) has the best performance in estimating both wind speed and storm surge (N. Lin and Chavas 2012).

3.2 Improving the Model

The model by Emanuel (Emanuel 2010) was chosen as a starting point for this work because it was found to perform better than other existing models (N. Lin and Chavas 2012), it is relatively simple, and it is derived from physical principles. This parametric wind model takes the form

$$v(r) = \frac{2r(R_m V_m + 0.5 f R_m^2)}{R_m^2 + r^2} - \frac{fr}{2} \tag{3.2}$$

where Vm, the maximum wind speed, and Rm, the radius of maximum wind speed, are the two parameters that define the wind field structure. f is the Coriolis parameter: a simple function of degrees-latitude from the equator. $v(r)$ is the wind speed a distance r from the storm center.

Note that this simple model is azimuthally symmetric since it is not a function of ϕ. The two free parameters, Rm and Vm, are set by minimizing the residual between the model and the measured wind speeds. A general cross section of this model is shown in Figure 3-2.

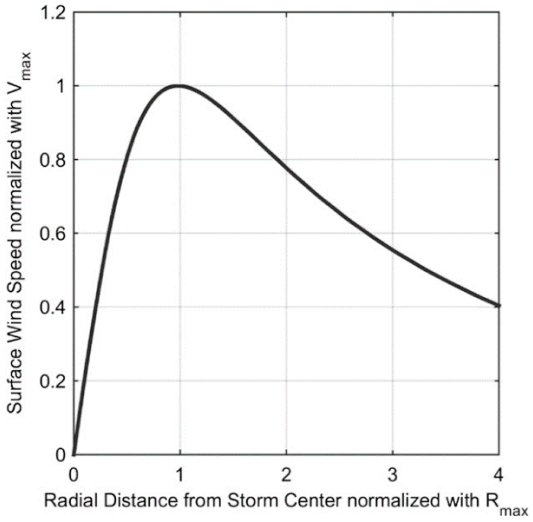

Figure 3-2: A cross section of the 2-parameter wind speed model given by Eq. (3.2) (Morris and Ruf 2017b)

This model, limited by only 2 parameters, can only capture first-order characteristics of the wind field. If there is sufficient information from the input wind speed measurements, the wind model can be made more complex by the addition of new parameters. As seen in Figure 3-2, this model only has one roll-off rate, or rate at which the wind speeds decrease with increasing radial distance from the storm center. The roll-off rate can vary widely in TCs and this model is found to generally underestimate the outer wind radii (Chavas, Lin, and Emanuel 2015). Two new parameters, *a* and *b*, are added to the parametric wind model to improve the roll-off rate and estimates of the wind radii (Morris and Ruf 2017a). The new model is given by

$$v(r) = \frac{2r(R_m V_m + 0.5 f R_m^2)}{R_m^2 + a r^b} - \frac{fr}{2} \tag{3.3}$$

Figure 3-3 shows how including *a* and *b* adds flexibility to the model. By tuning *a* and *b* to the wind speed measurements, the roll-off rate can be adjusted to match the wind speed measurements without altering the best-fit Rm andVm.

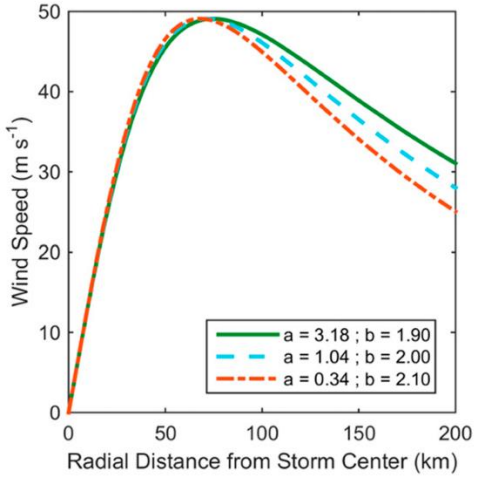

Figure 3-3: Parameters *a* and *b* allow for a tunable roll-off rate

While this four-parameter model is more complex and can capture more wind field characteristics, it still assumes azimuthally symmetry. Major hurricanes (defined as Category 3 or greater by the Saffir Simpson scale) are the most well-organized with the most azimuthal symmetry, but even these storms tend to have higher wind speeds in the northeast quadrant (of northern hemisphere storms) than in other quadrants. Very few storms can be accurately represented by an azimuthally symmetric model. The simplest azimuthal dependence is to add a first order harmonic scale factor. The resulting 6-parameter model is given by

$$V(r,\phi) = \left(\frac{2r(R_m V_m + .5fR_m^2)}{R_m^2 + ar^b} - \frac{fr}{2}\right)\left(1 - \frac{A}{2}(\cos(\phi - \phi_{max}) + 1)\right) \qquad (3.4)$$

The first term in large parentheses is simply the 4-parameter wind model from Eq. (3.3). It is scaled by the next term which varies sinusoidally between 0 and 1 as seen in Figure 3-4. The azimuthal scale factor contains two new parameters, *A* and ϕ_{max}. The parameter *A* denotes the

degree of asymmetry and ϕ_{max} denotes the azimuthal direction of maximum winds, where $\phi_{max} = 0$ is north of the storm center. A is a number between 0 and 1 where $A = 0$ returns the 4-parameter model and $A = 1$ has a wind speed of zero on the side of the storm oppositeVm.

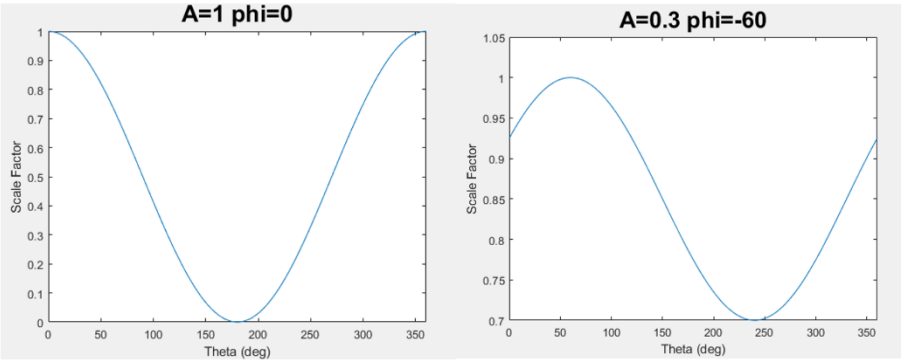

Figure 3-4: The azimuthal scale factor in an extreme case (left) and a typical case (right)

Figure 3-5 shows how the 6-parameter wind model in Eq. (3.4) is used to construct a full wind field from CYGNSS-like wind speed measurements of the storm. The top-left wind field is the full inner-nest wind field taken from the model HWRF. The bottom-left image is the HWRF wind field sampled in a CYGNSS-like fashion. The top-right wind field is constructed from the best-fit parameters which result from fitting the 6-parameter wind model to the "measurements" in the bottom-left. Note that a gradient descent approach is used to minimize the cost function in Eq. (3.1). The 6-parameter model gets the direction and magnitude of maximum wind speed correct, but other features of the true HWRF wind field are lost due to limited CYGNSS sampling in the bottom-left image and model limitations. The example in Figure 3-5 is an intense TC with a well-organized, typical wind structure so the model is able to represent the storm fairly well even with sparse measurements as input.

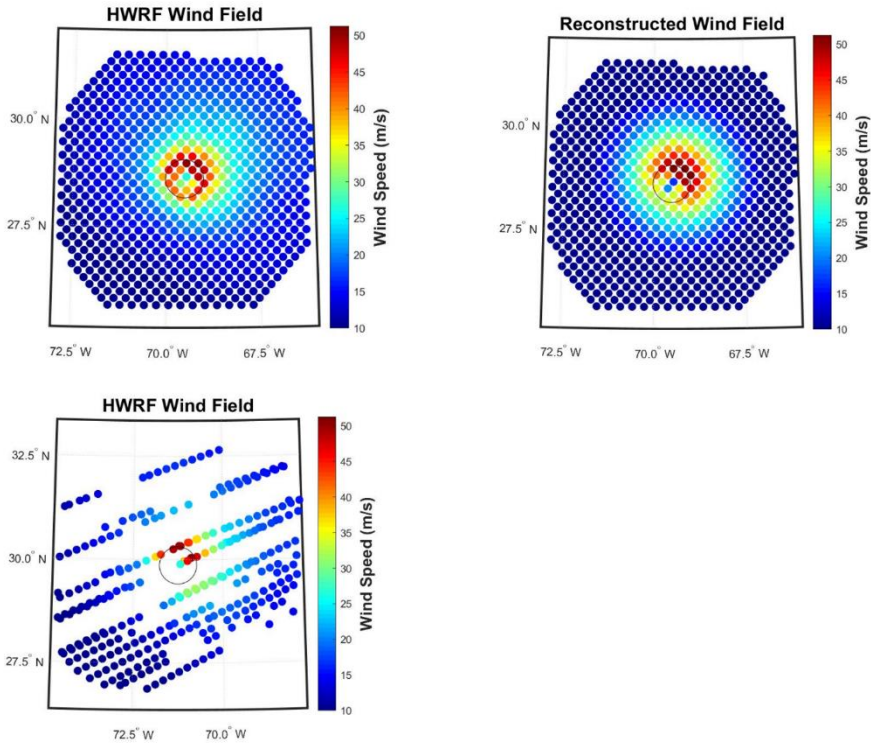

Figure 3-5: The upper-left image is a plot of the wind field from the model HWRF. The lower-left image samples the upper-left image in a CYGNSS-like fashion. The top-right image is the resulting wind field using the best-fit parameters and the 6-parameter model. The black circle represents the location of minimum surface pressure in HWRF.

The 6-parameter model is much improved due to the addition of the azimuthal parameters, but there a few remaining limitations. Figure 3-6 shows how this parametric wind model handles a weak TC with a less organized wind field. The left panel shows the true wind field which has a strong azimuthal dependence; the south side of the storm has very weak winds compared to the north side. In the right panel of Figure 3-6, the 6-parameter wind model identifies Vm and Rm correctly as well as the direction of the strongest winds. However, this model is not able to capture that the roll-off rate is very slight on the north side of the storm compared with everywhere else. Getting this right requires that the *a* and *b* parameters have their own azimuthal dependence. The model is also unable to represent the swirl of high wind speeds which wrap around to the southeast part of the storm but not the southwest. Many TCs which are

disorganized or at higher latitudes can have a more complex azimuthal dependence like this. To capture this type of behavior, the model would need a more complex azimuthal dependence (e.g., a second harmonic scale factor). Rm could also be given an azimuthal dependence for this model to represent a wider variety of TCs.

For many applications, this azimuthal dependence, despite its simplicity, is a significant improvement. For example, it is crucial for accurately predicting storm surge when the coast has varying levels of susceptibility to flooding and the storm surge forecast depends on an accurate landfall location and distribution of high wind speeds. However, for computing the integrated kinetic energy of the storm, there is little change when using the 6-parameter model instead of the 4-parameter model. The 4-parameter model typically underestimates the maximum wind speed because the parameter Vm is the azimuthally averaged Vm. The 6-parameter model more accurately estimates Vm but scales down the wind speed in most parts of the storm resulting in one quadrant with wind speeds greater than the 4-parameter model, one quadrant with wind speeds similar to the 4-parameter model, and two quadrants that are very similar to the 4-parameter model. The net effect is that there is little change in the computed integrated kinetic energy.

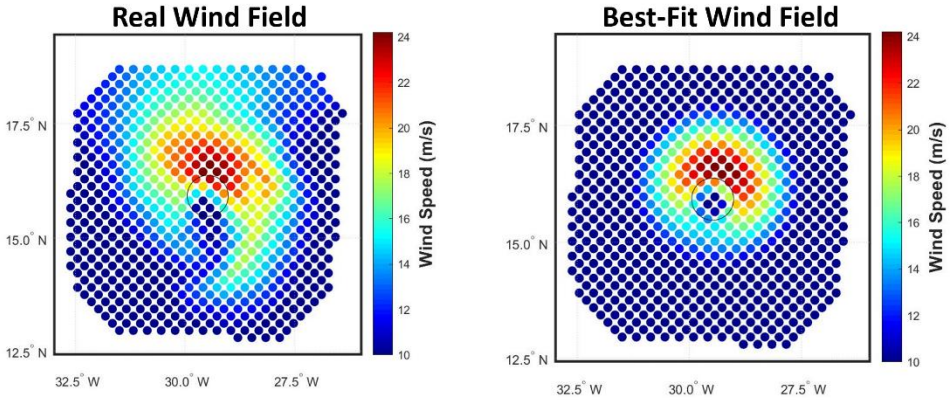

Figure 3-6: A real TC wind field is on the left. The 6-parameter model's attempt to represent this storm is on the right.

There are numerous ways to improve the performance of this model by adding new parameters and complexity. However, the performance of the model also depends on the number of wind speed measurements. If the number of wind speed observations is very limited, there may not be enough information to properly tune the model parameters. This issue becomes more prevalent as more parameters are introduced. For example, some CYGNSS overpasses do not have sufficient sampling density to identify the azimuthal dependence in the 6-parameter model. But when using measurements from a satellite which makes measurements in a large swath, there is plenty of input information to tune 6 parameters or more. Fitting a 10-parameter model using a CYGNSS overpass with only a handful of tracks would likely result in overfitting errors.

3.3 Error Sources

There are several sources of error which contribute to the difference between the model-generated wind field and the true TC wind field. There are errors due to the accuracy of the measurements. Any bias in the wind speed measurements will translate to the parametric model fit. However, errors due to zero-mean additive noise tend to be small. To examine this, we perturb the HWRF wind field with zero-mean Gaussian noise. Any difference between the HWRF wind field and the model wind field which used the perturbed winds as input is due to measurement noise. Generally, the difference is very small as long as the noise is zero-mean and the impact of noise lessens as the number of samples increases.

In many cases, the largest source of error is the number and distribution of samples. It is crucial that there be measurements near the center of the storm where the maximum wind speed is located and where the wind field is changing most quickly. It is also important for the wind

speed measurements to be distributed in all quadrants of the storm to get sufficient azimuthal information for the 6-parameter model. To isolate the error due to the sample distribution of a particular overpass, we sample a full HWRF wind field with the given sampling pattern. Next, we fit the parametric wind model to both the full HWRF wind field and the HWRF wind field that is sampled with this pattern. Any difference between the two reconstructed wind fields is due to the sample distribution. By using the parametric wind model in both cases, that error source is removed. For satellite systems like CYGNSS which often contain large gaps in sampling, the sample distribution is typically the largest source of error. For satellites that measure in swaths such as SMAP, there can still be error due to sampling if the storm is on the swath edge or if the storm is near land where there are gaps in the measurements. Another consideration is the spacing between samples. For example, there is 0.25-degree spacing between the wind speeds reported by SMAP. Even if there are no data gaps present, there could be information lost due to spatial smoothing across the reporting interval.

Error also occurs due to limitations in the parametric wind model. As was discussed above, the model is only able to capture first-order azimuthal asymmetries and there could be unmodeled azimuthal dependencies on *a*, *b,* and Rm. To isolate the error due to model limitations for a particular wind field, we fit the parametric model to the full HWRF wind field. The wind field constructed from best-fit parameters is compared to the original HWRF wind field. Any differences are due to the inability of the model to represent the storm's wind structure.

There could also be error due to the minimization algorithm which fits the parametric wind model to the measurements. In the search for a global minimization of the cost function, the algorithm could converge to a saddle point or other local minimum of the cost function. This has

not been an issue with the 6-parameter model, but it could become a problem if more parameters are added.

A full error analysis could be done to determine the average contribution of each error source. This has not been done because there are infinite possible sampling distributions for CYGNSS overpasses. In practice, it would be most useful to know if the sampling of any given overpass is sufficient to construct a wind field that is accurate to within a threshold. This could potentially be done with machine learning by using many HWRF cases and many sampling patterns as training data. To this point, however, each case of interest has been analyzed individually to estimate the error due to sampling using the method that was described previously.

Chapter 4 MTrack: Tropical Cyclone Center Fix from Satellite Wind Speed Observations

Accurate knowledge of a TC's center location, or the center fix, is critical for forecasting and reanalysis studies. The Dvorak intensity estimation technique, a frequently used TC monitoring method, requires a storm center fix as its first step (Olander and Velden 2007; Dvorak 1975). The accuracy of quadrant-specific wind radii estimates depends on storm center accuracy. For example, if the storm center is placed too far to the northeast, then the northeast quadrant's wind radii will be too small and the southwest quadrant's wind radii will be overestimated. Most TC modeling applications require a center location as input as well. However, for all its importance, storm centers can vary between different World Meteorological Organization (WMO) regional centers as indicated by the WMO International Best Track Archive for Climate Stewardship (IBTrACS) (Knapp et al. 2010). There is need for an automated center fix algorithm which can perform with more consistency.

The Automated Rotational Center Hurricane Eye Retrieval (ARCHER) TC center fix technique fits spiral and ring shapes to satellite imagery of the TC (Wimmers and Velden 2016). ARCHER works best for well-organized storms with a clear eye, but only 12.6% of satellite imagery contain a detectable eye (Knapp, Velden, and Wimmers 2018). Spiral shapes are matched to the rainbands of the TC, but this can be difficult for disorganized storms with poorly defined bands. Both ring and spiral fitting are limited by storm organization and the lack of visible satellite imagery at night.

Another technique traces scatterometer wind vectors inward to the storm center, but the quality of these winds is known to degrade in heavy precipitation (Hilburn et al. 2006; Portabella et al. 2012). The method is most used in weak storms that are not well-suited for spiral or ring fitting; however, scatterometer winds struggle with directional ambiguity at lower wind speeds (W. Lin et al. 2013). Current scatterometers are also limited by relatively long revisit times, especially for measurements of TCs. Ground-based radars and aircraft reconnaissance are the preferred data sources for storm center fixing, but the former can only be done at or near landfall, and the latter is only available for about 30% of storms in the Atlantic basin and even more rarely in the East and Central Pacific (Rappaport et al. 2009).

MTrack, a new storm center fix technique, was developed to overcome these issues. MTrack is an automated algorithm which determines the center location of a TC from a scalar wind field derived from satellite observations. The foundation of MTrack is fitting a TC parametric wind speed model (as described in Chapter 3) to a satellite-observed wind field and computing the root-mean-square difference, or residual, between model and measurement. The converged model parameters and the residual depend on the assumed storm center location. The assumed TC center is varied systematically over a wide gridded domain containing the storm. The MTrack fix is the TC center location at which the residual is minimized.

Much of this chapter is taken from (Mayers and Ruf 2019) as well as another publication (Mayers and Ruf 2021) which has been accepted for publication (in press) by the *Bulletin of the American Meteorological Society*.

4.1 MTrack with SMAP

MTrack can use any wind speed measurements as input, but this section will focus on wind speed measurements made by the NASA Soil Moisture Active Passive (SMAP) microwave radiometer because it has very different sampling properties than CYGNSS.

SMAP is a NASA satellite launched on 31 January 2015 which includes an L-band imaging radiometer. Its primary mission objective is to observe soil moisture and freeze/thaw state from space to improve estimates of water, energy, and carbon transfers between the land and atmosphere (Entekhabi et al. 2010). SMAP also observes over the oceans and can estimate near-surface wind speed from the thermal emission of the wind-roughened ocean surface. This is done in all precipitating conditions and the measurements show no sign of saturation at high wind speed (Meissner, Ricciadulli, and Wentz 2017). SMAP makes measurements in a 1000 km swath with an orbit that repeats every 8 days (though a TC is measured by SMAP more frequently than this). Compared to CYGNSS, SMAP makes relatively infrequent measurements but provides more complete coverage since there are typically no gaps in the SMAP swath. SMAP data used in this work were taken from the Remote Sensing Systems gridded product which is available at http://www.remss.com/missions/smap/.

An MTrack fix can be made for each SMAP overpass of a TC. First, a search grid is established around the interpolated Best Track storm center location. For each assumed storm center location in the grid, the parametric wind model is fit to the SMAP wind speed measurements using a gradient descent algorithm to minimize the residual difference. The wind model used with SMAP is the 6-parameter wind model (Eq. 3.4) described in Chapter 3. The full storm coverage provided by SMAP allows for detailed information about the storm's wind field, including azimuthal variation and roll-off rate, to be input to the model fit. It should be noted that

at each gradient descent iteration the parametric wind field is smoothed using a Gaussian filter with standard deviation equal to the spatial resolution of SMAP (40 km). This is done so the model is more representative of the observations which undergo a sort of spatial averaging due to the antenna as discussed in Chapter 2. Smoothing of the parametric model is especially important for accurate representation of small storms where the eye is not resolved by SMAP.

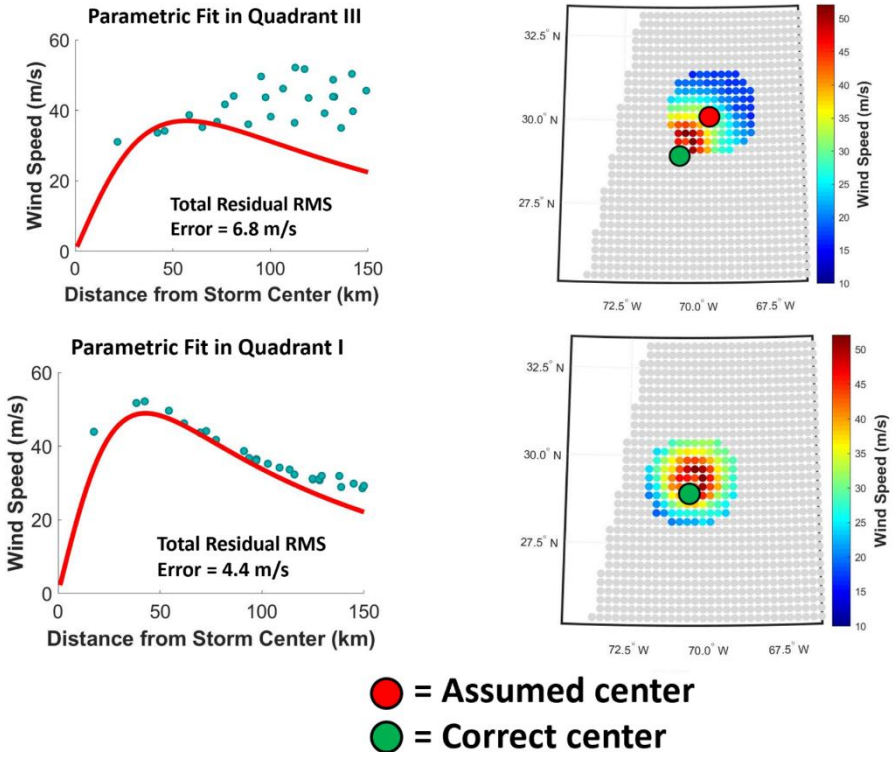

Figure 4-1: The top panel shows a poor fit of model to measurements when the wrong storm center is assumed. The bottom panel shows a much lower residual when the correct storm center is used. Note that the 6-parameter model with azimuthal variation is used with SMAP. The plots on the left use the average of the parametric model in that quadrant.

An example of the process by which MTrack locates the TC center using SMAP winds is shown in Figure 4-1. In the upper half of Figure 4-1, an incorrect storm center is assumed which is about 150 km northeast of the correct location. The wind speed observations are highlighted in a 150 km radius around the assumed center. In the southwest quadrant, the wind speed increases out to 150 km with no sign of decay. This is not characteristic of a typical TC. The parametric

model is fit to the measurements, but it does a poor job because the model is constrained to a radially decaying TC wind profile. This is seen in the top-left of Figure 4-1. The residual (root-mean-square difference) between the measurements and the model is 6.8 m/s.

Next, in the lower half of Figure 4-1, a storm center is assumed which is close to the correct location. Again, all wind speed observations within 150 km of this assumed center are highlighted. Note that the algorithm uses all samples within Rm + 150 km to tune the parametric wind model to allow for large storms. Focusing on the northeast part of the storm in the lower left part of Figure 4-1, the wind speed is maximized around 50 km from the assumed center and decays radially out from there. This is representative of a typical TC wind field, and the parameters of the wind model can be adjusted to produce a model wind field that closely matches the observations. The residual in this case is 4.4 m/s, which is much lower than for the previous center.

The MTrack storm center search is performed over a grid of assumed centers around a first guess location. Typically, this results in a grid of residuals which are lowest near the MTrack center, with a gradual increase in all directions away from it. A second search takes place over a finer grid centered on the lowest residual from the previous search. The minimum residual in the second search is the MTrack center. The assumed center in the lower half of Figure 4-1 is the MTrack center.

Figure 4-2 shows MTrack results using SMAP wind speed measurements of well-organized Category 4 Hurricane Florence on 12 September 2018 at 1050 UTC. The red dot in the figure represents the time-interpolated storm center generated in near-real-time (NRT) and posted on the U.S. Naval Research Laboratory (NRL) website (very similar to TCVitals). For NRT processing there are often less data available for determining the storm center location

compared with the reanalysis Best Track storm center fix. In this case, the NRT storm center does not agree with the position of the eye in the SMAP wind field. MTrack uses the NRT center

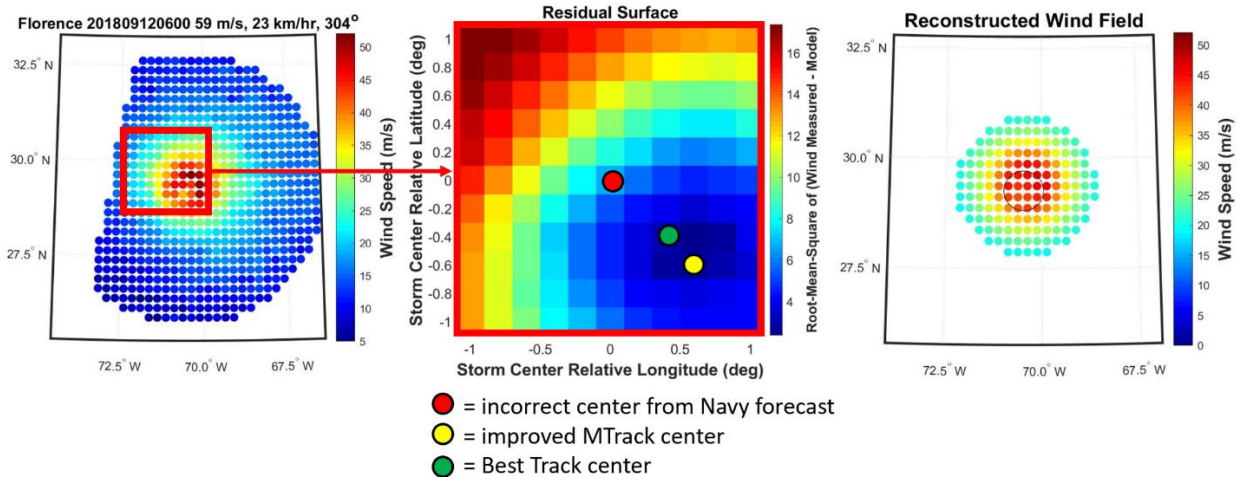

Figure 4-2: SMAP wind speeds of Hurricane Florence are used as input to MTrack. The MTrack center fix offers an improvement over the near-real-time storm center estimate from the Navy forecast.

as a first guess location and estimates an improved center located about 50 km to the Southeast—in very good agreement with the Best Track center fix. The right panel of Figure 4-2 shows the wind field constructed by the parametric wind model using the best-fit parameters and MTrack storm center location. The black circle is a 50 km radius centered around the Best Track center. A strong, organized storm with an eye visible in the satellite-measured wind field is the easiest case for MTrack or any center fix method. Unsurprisingly, MTrack finds the correct center, and the parametric wind model matches the SMAP wind field very well.

Figure 4-3 demonstrates that MTrack works well even when a storm is on the edge of the SMAP swath. This is also Category 4 Hurricane Florence but a day earlier than the previous example—11 September 2018 at 1014 UTC. In this case, the eye of the storm is about 30 km outside of the swath. The time-interpolated Best Track center is used as the first guess instead of the NRT Navy center as in the last example. It is important to note that the MTrack center

solution is independent of the first guess as long as the search grid is large enough to capture the storm center. Shifting the first guess simply shifts the search grid and the resulting storm center fix is unchanged. While MTrack iterates over the search grid (red box in Figure 4-3), some

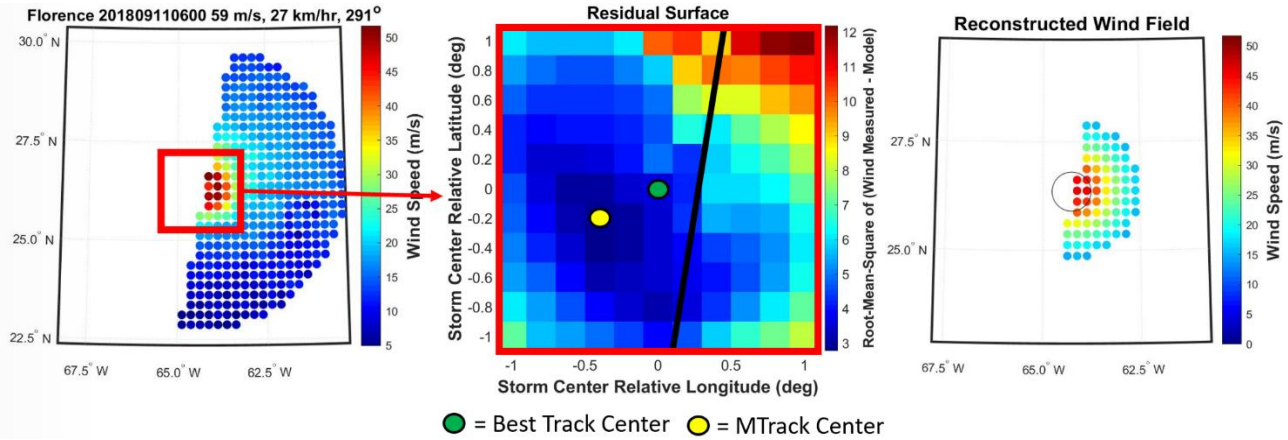

Figure 4-3: MTrack can find the storm center when the storm is only partially on the SMAP swath

assumed storm center locations are off the swath edge so there are no SMAP wind speed measurements in the immediate vicinity. In these cases, it is still possible to fit the parametric wind model to measurements and report a residual as long as there are measurements within a 150 km radius of the assumed center. MTrack finds a center about 40 km west of the swath edge which is very close to the time-interpolated Best Track center, the best estimate of truth. The right panel of Figure 4-3 shows that the MTrack wind field is very similar to the SMAP wind field. Again, this is a good way to check that MTrack is performing as intended.

Figure 4-4 shows the SMAP wind field of Category 3 Hurricane Dorian on 3 September 2019 when it was stalled over Grand Bahama. Much of the storm's core is not measured by SMAP in this case due to the presence of land. Despite the missing wind speeds, MTrack is able to find a storm center solution very close to the Best Track center as seen in the residual error surface in the right panel of Figure 4-4. The wind field in the middle panel is constructed from

the MTrack parametric wind model using best-fit parameters and MTrack center location. The wind field that is "seen" by MTrack is very similar to the SMAP wind field, which suggests that MTrack is working as intended (the parametric wind model is able to represent the primary features of the SMAP wind field) and the storm center solution is reliable. In this reanalysis case,

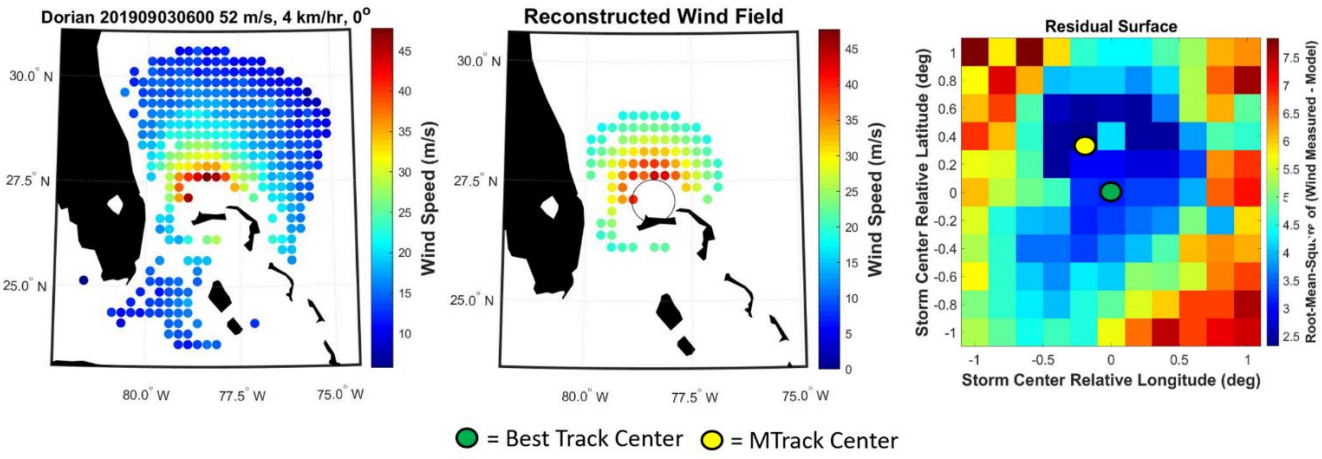

Figure 4-4: MTrack can find the storm center when there are data gaps due to land

there is a Best Track fix available for comparison to confirm that the MTrack fix is accurate. However, comparison of the MTrack wind field to the SMAP wind field is a useful alternative way to determine how much confidence should be placed in the MTrack fix in NRT operation when a Best Track fix is not available.

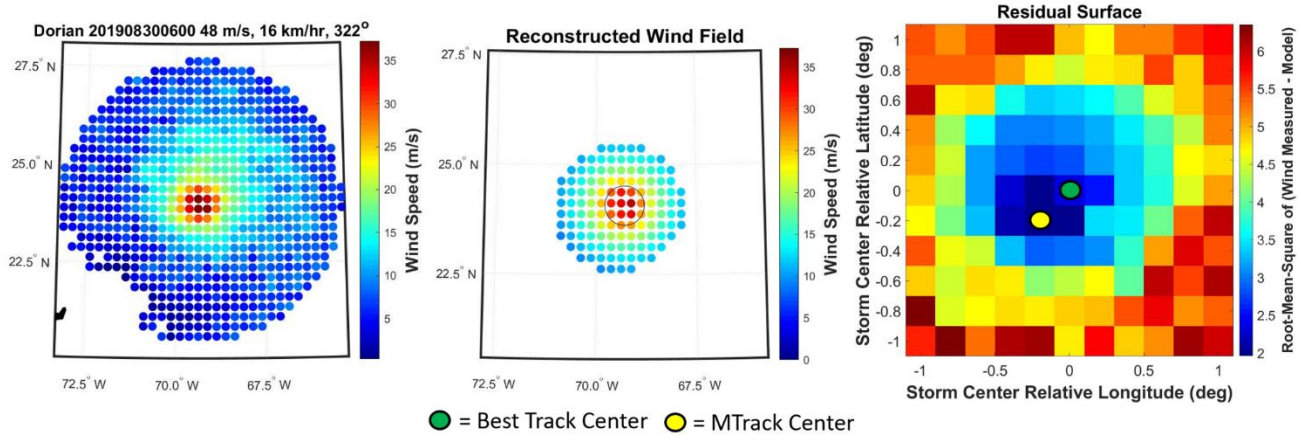

Figure 4-5: Small TCs can be represented by the parametric model due to the averaging that is done at each iteration

Figure 4-5 shows a SMAP wind field of Category 2 Hurricane Dorian on 30 August 2019. At this point, Dorian is very small and SMAP is not able to resolve the lower wind speeds in the eye. Although the eye is not visible in the SMAP wind field, MTrack is still able to operate successfully because of the spatial smoothing that is applied at each iteration. This allows the MTrack wind field to better simulate what SMAP sees at 40 km resolution. The right panel of Figure 4-5 shows that MTrack finds a storm center location very close to the Best Track center. The center panel of the same figure shows that the parametric wind model is able to capture the behavior of this very small storm, with small Rm, *a* and *b* parameters tuned to match the roll-off rate, and the smoothing filter able to remove any evidence of the eye to match the SMAP measurements.

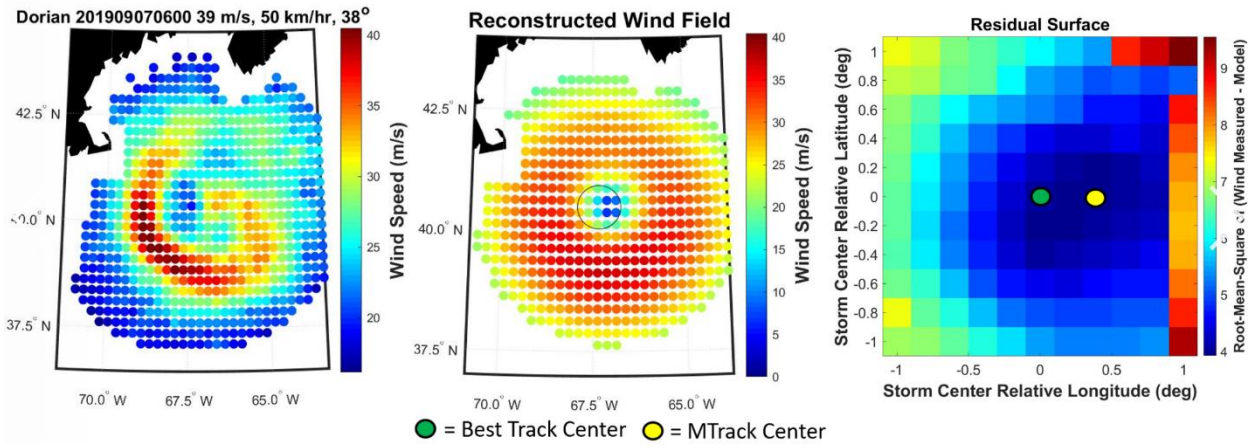

Figure 4-6: The parametric wind model is unable to represent unusual wind fields like this

Figure 4-6 and Figure 4-7 demonstrate some of the limitations of MTrack. Figure 4-6 shows Category 1 Hurricane Dorian at a higher latitude on 7 September 2019. The SMAP wind field reveals an unusual spiral shape which cannot be represented by the MTrack parametric wind model. When the primary features of the wind field cannot be captured by the wind model, the storm center solution generally cannot be trusted because MTrack is not operating as

intended. However, in this case, the MTrack storm center solution is in good agreement with Best Track as seen in the right panel of Figure 4-6. The center panel of Figure 4-6 shows that the best-fit Rm is very large so that the MTrack wind field has high wind speeds almost everywhere in the domain. This does not represent the SMAP wind field very well, but this pattern has the lowest residual compared with SMAP when the assumed storm center is at the center of the spiral, which happens to be close to the Best Track center. In this case, MTrack is fortunate to be fairly accurate.

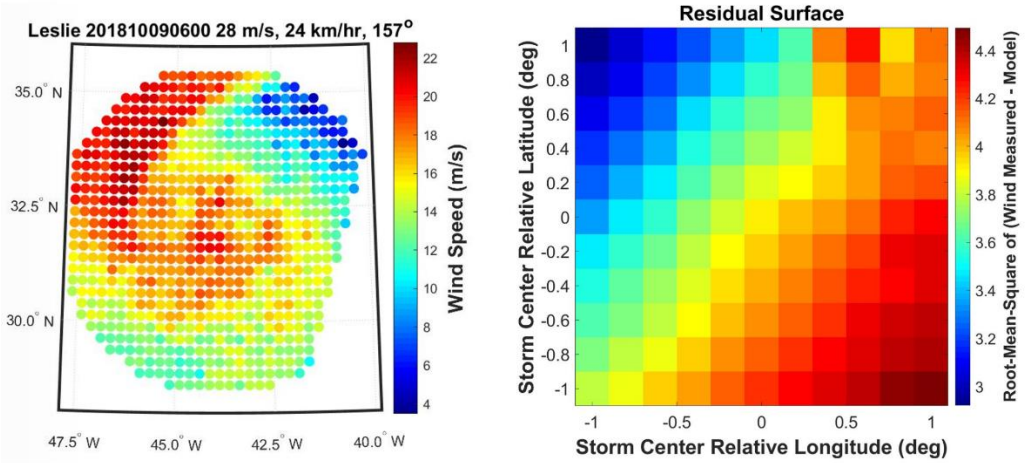

Figure 4-7: MTrack does not work when there is little structure in the measured wind field

Figure 4-7 shows the SMAP wind field of a very weak and disorganized Tropical Storm Leslie on 9 October 2018. There is little discernible structure in the measured wind field, which makes it difficult for MTrack to function properly. As a result, the right panel of Figure 4-7 shows that the MTrack residual error map does not have a clear minimum in the search domain, meaning that MTrack fails to find a storm center location. The MTrack search domain is large enough (2x2 degrees) that a search initialized by a NRT center fix will always have the Best Track center contained within the search domain (Trahan and Sparling 2012). Therefore, storm center locations outside of the 2x2 degree search grid are not considered.

4.2 MTrack with CYGNSS

Using CYGNSS data in TCs is not as straightforward as it is for SMAP. SMAP measures wind speed across a 1000 km wide swath that passes over a storm in less than 10 minutes. Because of this, the SMAP wind speeds can be considered an instantaneous snapshot of the storm's wind field without introducing significant error. SMAP also generally produces gap-free sampling across its swath. CYGNSS consists of 8 satellites which make measurements of a storm in bursts which vary in duration from minutes to several hours. The time between bursts as well as the number of CYGNSS tracks in each burst is random. To identify a storm center at just one time with CYGNSS, the samples must be framed in storm-centric coordinates with respect to the time at the center of the chosen time interval. A 3-hour duration is chosen, and the window is aligned to include as many CYGNSS samples as possible. Best Track storm centers are needed on either side of the time interval. These storm centers are linearly interpolated to produce a storm center that is continuous in time for the transformation to storm-centric coordinates. Also, the spatial coverage provided by CYGNSS is inherently "gappy" in that measurements are made along specular point tracks and no measurements are present between the tracks.

Once the CYGNSS wind speeds are selected and are represented in storm-centric coordinates, the parametric wind model is fit to them (the same process as Figure 4-1). Note that the 4-parameter model is typically used for CYGNSS rather than the 6-parameter model that was used for SMAP. This is because there is less information about TC structure available from a CYGNSS overpass compared to a gap-free SMAP overpass. It can be difficult to avoid overfitting when using the 6-parameter model with CYGNSS measurements. The RMS difference between the parametric model and the data constitutes one point on the residual error surface. This process is repeated over a two-dimensional grid of possible storm center locations

to generate the residual error surface. Note that all CYGNSS data within 400 km of the assumed storm center are used, with the result that some new samples may be added and others removed from the sample population for each iteration.

The storm center location is found by fitting a 2-D Gaussian function to the error surface. Simple, direct selection of the minimum value in the error surface is not done to limit the impact of measurement noise and the presence of outliers. This is not a problem with SMAP—the gap-free wind field makes the surface of residuals more well-behaved and less sensitive to measurement noise or outlier samples. Points in the error surface for which the corresponding parametric fit radius of maximum wind speed (Rm) is greater than 100 km are considered non-physical and are not used in the Gaussian fit because TCs typically have Rm well below 100 km (Lajoie and Walsh 2008). The storm center location is given by the minimum of the 2-D Gaussian fit to the error surface.

MTrack assumes a storm velocity by linearly interpolating between Best Track fixes. When testing different storm center locations while generating the residual error surface, the assumed trajectory of the storm is unchanged. Effectively, in each grid cell of the residual surface, MTrack is testing a translation of the storm's path. To reduce the impact of Best Track errors on the MTrack storm center, an ensemble averaging approach is used, similar to how TC paths are forecast (Zhang and Krishnamurti 1997). The Best Track fixes are randomly perturbed in each trial, resulting in an ensemble of storm center estimates. The radial perturbation about the Best Track centers is a zero mean Gaussian with a specified standard deviation, and the azimuthal angle is uniformly distributed between 0 and 360 degrees. The standard deviation of the perturbing Gaussian varies between 10 and 70 km, which is consistent with the errors seen in Best Track fixes (Landsea and Franklin 2013). Each Best Track storm center is perturbed

independently. The final storm center estimate is the average over the ensemble. We refer to this as the MTrack estimate.

Two examples of MTrack operating with CYGNSS input are given to demonstrate some characteristics of its performance. The first, with Atlantic Hurricane Jose on 17 Sep 2017, is for a weakly organized storm where the fix changes significantly from the interpolated Best Track location. The second example, for Pacific Hurricane Sergio on 7 Oct 2017, is a case where the MTrack fix is consistent with Best Track.

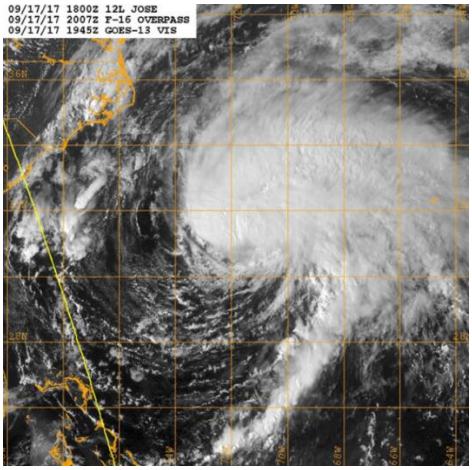

Figure 4-8: Satellite imagery of Hurricane Jose at 2015 UTC 17 Sep 2017 (Category 1 storm) shows disorganization and no visible eye. Since other storm center fix algorithms struggle in these cases, this is an opportunity for MTrack to improve upon performance.

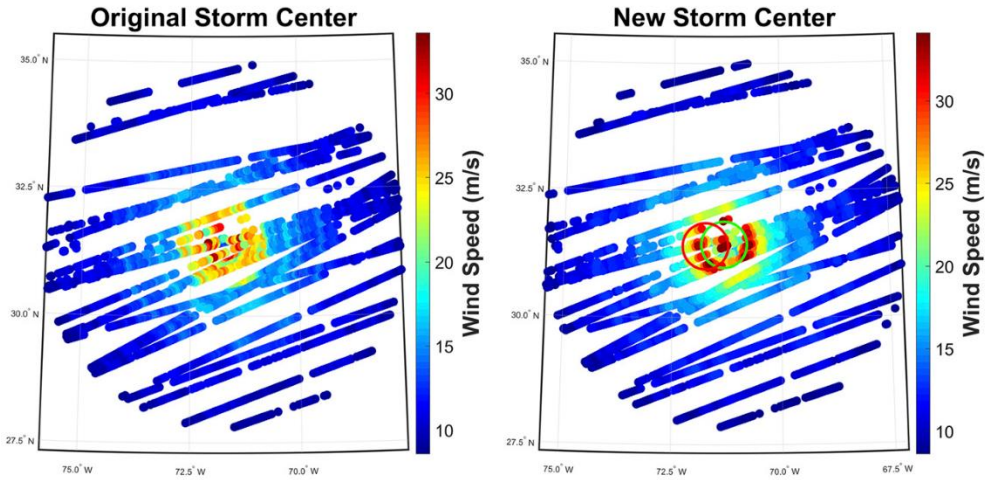

Figure 4-9: The left panel shows the CYGNSS measurements when an incorrect storm center location is used to place the samples in storm-centric coordinates. The right panel uses an improved storm center location from MTrack. The resulting wind field looks much more like a typical TC.

Hurricane Jose is considered for the 3-hour interval centered on 20:15 UTC on 17 September 2017 (Category 1 storm). This is a high latitude case (~32 deg) for which CYGNSS has many samples. Satellite imagery at this time (Figure 4-8) shows weak organization and lack of a clear eye, both of which can limit the accuracy of a conventional storm center fix. This is an opportunity for CYGNSS to improve upon the storm center location. The left panel of Figure 4-9 shows the wind field measured by CYGNSS in storm-centric coordinates, assuming the interpolated NHC storm center fix is correct, and using a 10 km radial smoothing to reduce measurement noise. The inner core has fairly uniform wind speeds over more than a 150 km extent. This wind structure is highly atypical and suggests that the interpolated NHC storm center fix may be incorrect.

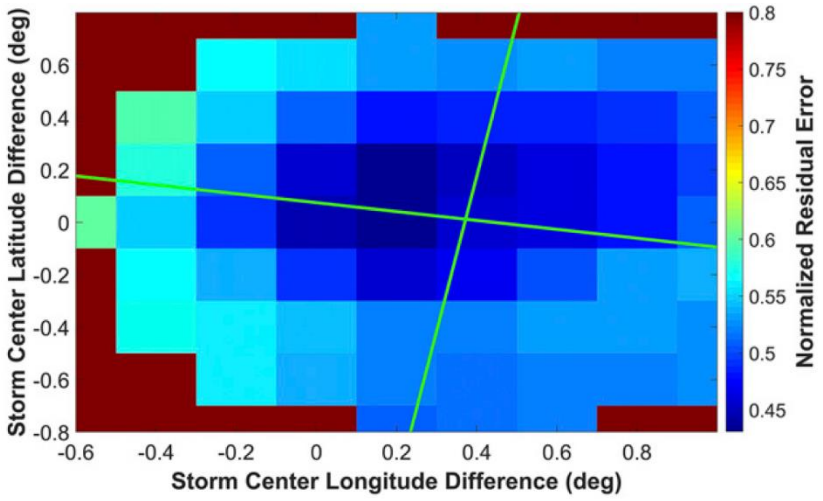

Figure 4-10: a typical residual surface for Hurricane Jose at 2015 UTC 17 Sep 2017. The cell at (0,0) is the first guess location give by interpolation of the Best Track fixes. Each grid cell shows the normalized residual between parametric wind model and CYGNSS measurements for the assumed storm center location. The red cells are removed from consideration because they have unrealistic Rm values. The green intersecting lines represent the 2D Gaussian fit.

Figure 4-10 shows the residual error surface for a range of possible storm center locations, together with the 2-D Gaussian fit to the surface. Each point in the grid is the RMS difference between the parametric fit and the CYGNSS wind speed data which is then

normalized by the maximum wind speed. The crosshairs in the figure indicate the location of the minimum in the Gaussian fit, which would be the estimated storm center location without ensemble averaging. The red grid cells indicate cases for which Rm > 100 km in the best-fit parametric model. Those points are not considered by the Gaussian fit. Note that the center location is about 0.2 deg away from the grid point with minimum RMS error.

Figure 4-11 shows the results after ensemble averaging. 100 trials were performed with Best Track storm center locations perturbed by a zero mean Gaussian with a standard deviation of 10 km, and the resulting storm center for each trial is indicated by a black 'x'. The average over all trials is the MTrack fix. Note that the individual storm center fixes are fairly insensitive to perturbations in the Best Track centers, as indicated by their tight clustering. This suggests that the ensemble averaged storm center should not be affected much by Best Track errors. This is very important in producing an *independent* estimate of the storm center location (i.e., not influenced by Best Track or its errors).

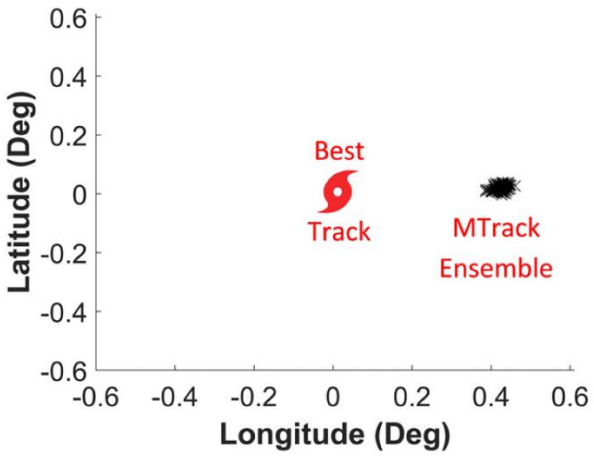

Figure 4-11: Ensemble of storm centers for Hurricane Jose at 2015 17 Sep 2017: 100 trials were run with perturbed NHC Best Track fixes used as input (radially perturbed by a Gaussian with a standard deviation of 10 km). The first guess, which is at 08, 08, is given by linear interpolation of the NHC Best Track fixes. Each black cross is the refined storm center location for each of the 100 trials. The lack of scatter in the results of the 100 trials demonstrates how MTrack is insensitive to error in Best Track input.

A new storm-centric, radially smoothed wind field is constructed using the MTrack storm center location and is shown in the right panel of Figure 4-9. The wind field now has its highest winds concentrated around the center and the winds decay radially as expected. The radius of maximum winds in this image is about 80 km, which is close to the operational estimate: 90 km. Within Rm, there are lower wind speeds which is also characteristic of a TC. This is a significant improvement over the original wind field in the left panel and is strong evidence in support of the improvement in accuracy of the new storm center location.

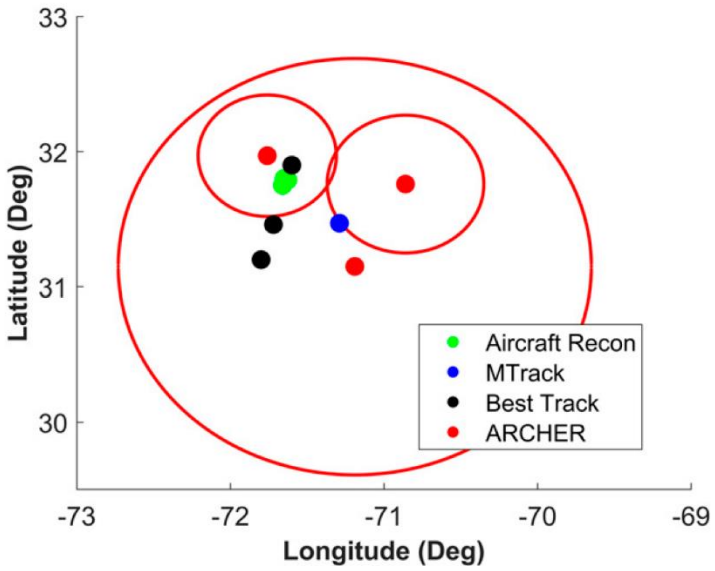

Figure 4-12: Comparison between the storm center locations of MTrack, Best Track, ARCHER, and aircraft recon for Hurricane Jose on 17 Sep 2017. The storm is moving to the northeast. The three Best Track fixes are at 1800 and 0000 UTC, with the intermediate point as the center linearly interpolated to the CYGNSS time. The MTrack fix is at 2015 UTC. The ARCHER fixes are at 1745, 2008, and 2258 UTC. The aircraft recon fixes are at 2207, 2313, and 2329 UTC. The circles around the ARCHER fixes are the 95% confidence radii.

The new CYGNSS center fix can be independently validated by aircraft recon and ARCHER. Figure 4-12 plots the new MTrack storm center together with the ARCHER, aircraft recon, and NHC Best Track fixes. The aircraft recon and Best Track centers agree very well (Best Track probably used the aircraft recon fixes as input after all). Two ARCHER fixes are over half a degree to the east of the Best Track fixes, and one Best Track fix even lies outside of

the 95% confidence radius of the ARCHER fix. The CYGNSS storm center location is not quite as far East as ARCHER. It represents a compromise between all available fixes since it is between Best Track and ARCHER, while still inside ARCHER's 95% confidence radius. A third estimate of the storm center can help disambiguate the fix in cases where ARCHER and Best Track do not agree, or in cases like this it can indicate that the answer is in the middle.

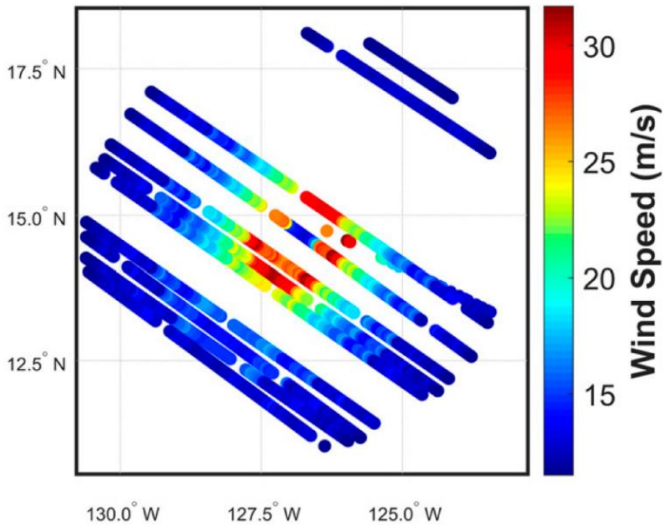

Figure 4-13: CYGNSS wind speeds in storm-centric coordinates over a 3-hour period for Hurricane Sergio at 1330 UTC 7 Oct 2018. This TC has a large eye which is resolved in the CYGNSS measurements.

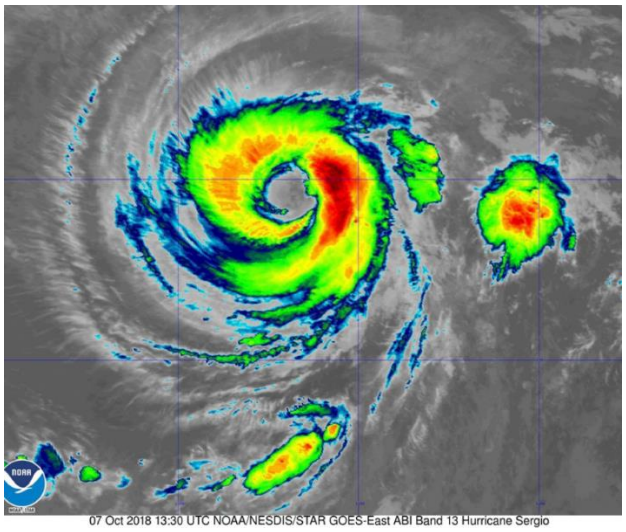

Figure 4-14: Satellite imagery of Hurricane Sergio at 1330 UTC 7 Oct 2018 shows an organized storm with a very large eye. This explains why CYGNSS, which has a spatial resolution of 25 km, can resolve the eye in Figure 4-13.

The second example considers Category 2 Hurricane Sergio in the Pacific using 3 hours of CYGNSS measurements centered on 13:30 UTC on 7 Oct 2017. The latitude of this storm is about 15 deg N so there is a lower spatial density of CYGNSS samples. Figure 4-13 shows the initial wind field (assuming the interpolated Best Track fix is correct) with highest winds near the eyewall and radial decay away from the center. CYGNSS resolves the eye in this case because Sergio has an unusually large eye, as seen in the satellite imagery in Figure 4-14. Since the first guess of the storm center appears to be quite good, this case can be used to test whether the MTrack algorithm estimates a storm center location close to the first guess. The large eye also ensures high confidence in both the Best Track and ARCHER fixes. The MTrack fix should be in close agreement with the others.

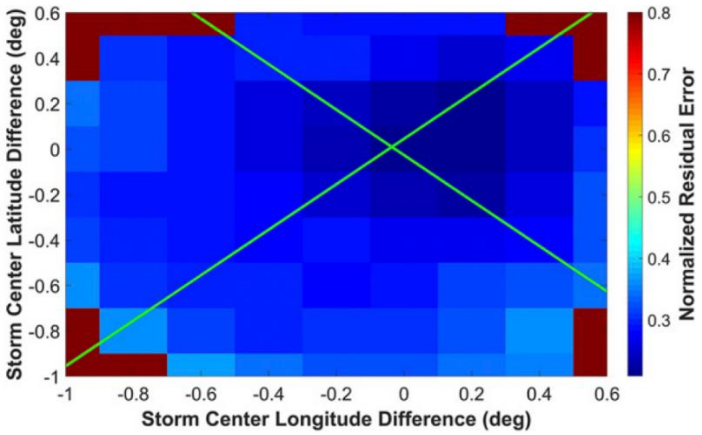

Figure 4-15: a typical residual surface for the case of Hurricane Sergio at 1330 UTC 7 Oct 2018. The point (0,0) is the first guess location given by interpolation of the Best Track fixes. Each grid point is the normalized residual between parametric model and CYGNSS wind speeds. The red points are masked out because Rm is unphysical. The green intersecting lines represent the 2D Gaussian fit to the residual surface. The intersection point shows the MTrack fix is very close to the first guess storm center location.

The residual error surface and its 2-D Gaussian fit are shown in Figure 4-15. A distinct minimum in the error surface reveals the storm center location less than 4 km from the first guess location. Figure 4-16 combines the CYGNSS, Best Track, and ARCHER storm center locations. Because the eye is so clear, there is little uncertainty in the ARCHER fix. Between 12 and 18

UTC on 7 October, both the Best Track centers and the CYGNSS MTrack center fall within the 95% confidence radii of ARCHER.

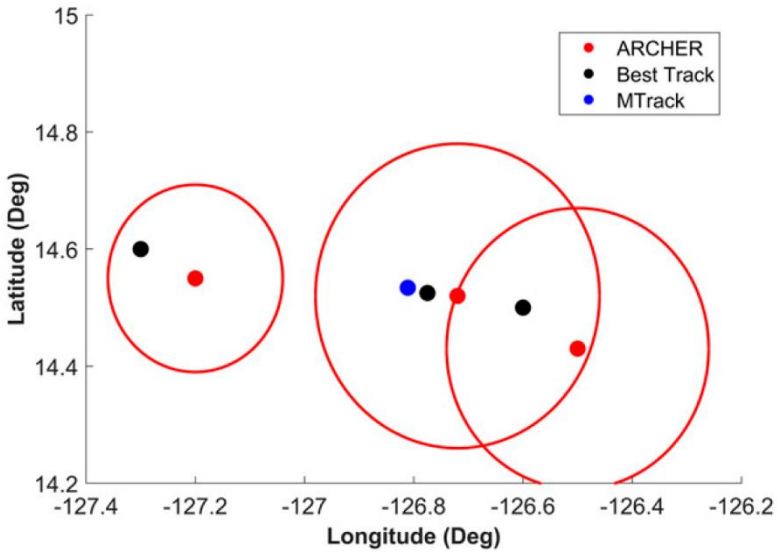

Figure 4-16: Comparison of storm center locations from MTrack, Best Track, and ARCHER for Hurricane Sergio on 7 Oct 2018. The storm is moving to the northwest. The black dots are Best Track fixes at 1200, 1330, and 1800 UTC with the intermediate point obtained by linear interpolation of the other two to the CYGNSS time. The blue dot is the MTrack center at 1330 UTC. The red dots are ARCHER fixes at 1200, 1411, and 1800 UTC. The red circles around the ARCHER fixes are the 95% confidence radii. All three storm center sources agree, which is expected for a storm with such a clear eye.

4.3 MTrack Performance Analysis

To evaluate the accuracy of MTrack, there must be a true storm center fix for comparison. However, there is no truth available for storm centers—the closest thing is Best Track, a 6-hourly reanalysis summary of all TCs. In 2012, Best Track storm center fix uncertainties were independently estimated by 10 experts, then the numbers were averaged together. According to (Landsea and Franklin 2013), “the results obtained should be considered ‘ballpark’ estimates of uncertainty where virtually none have existed previously”. MTrack storm center fixes are compared to Best Track and the average distance between the two can be

considered an upper bound on the MTrack uncertainty (since a component of the difference is also due to Best Track error).

Storm Strength	Best Track Uncertainty (km) (only satellite observations available)	Average Difference between Best Track and MTrack TC Centers (km)	MTrack Success Rate
Tropical Storms	53	46	82%
Cat 1-2	40	36	96%
Cat 3-5 (major hurricanes)	27	21	99%

Table 4-1: Comparison between Best Track and MTrack uncertainties (using SMAP input)

MTrack was run for all SMAP overpasses of 2018 storms in the Atlantic, West Pacific, and East Pacific basins (296 overpasses). First, overpasses with a minimum residual on the edge of the search grid were removed. When MTrack fails to find an optimal center due to a disorganized wind field, the lowest residual is most frequently on the edge of the search grid (as in Figure 4-7). For tropical storms (< 33 m/s), Category 1 and 2 storms (33-49 m/s), and major hurricanes (> 49 m/s), the percentage of cases removed for this reason are 18%, 4%, and 1%, respectively. The difference between the MTrack and Best Track center fixes are calculated for the remaining cases, binned by storm intensity, and averaged together. The results are displayed in Table 4-1. For tropical storms, Category 1 and 2 storms, and major hurricanes, the MTrack error upper bounds are 46 km, 36 km, and 21 km, respectively. This is an upper bound on MTrack error because a component of the difference is due to Best Track error. Best Track uncertainties, binned the same way by intensity, are approximately 53, 40, and 27 km (Landsea and Franklin 2013). Both the MTrack and Best Track errors decrease with intensity because intense hurricanes are typically better organized with an easily identifiable eye, while weak storms are disorganized and do not have an obvious center of circulation. Note that MTrack errors are within the estimated Best Track uncertainty for all storm intensities.

The MTrack fix uncertainty with CYGNSS wind speeds is defined as the standard deviation of the ensemble fixes. This interpretation is borrowed from the concept of "cone of uncertainty" in ensemble forecasting of TC track. The uncertainty will depend on the standard deviation of the Gaussian perturbations made to the Best Track fixes when generating the ensemble population. Because the accuracy of the Best Track fix is a function of the storm's intensity and the available observations, these things also impact the accuracy of the MTrack fix. A second MTrack performance characteristic is the ratio between the assumed error in the Best Track fix (the standard deviation of the perturbing Gaussian) and the resulting uncertainty in the MTrack fix. This ratio, henceforth called the uncertainty reduction factor, represents the reduction in storm center fix uncertainty that results with the MTrack algorithm. This is a unitless value. A tight cluster of fixes in the MTrack ensemble means that there is high confidence in the solution and that it is only slightly affected by Best Track errors.

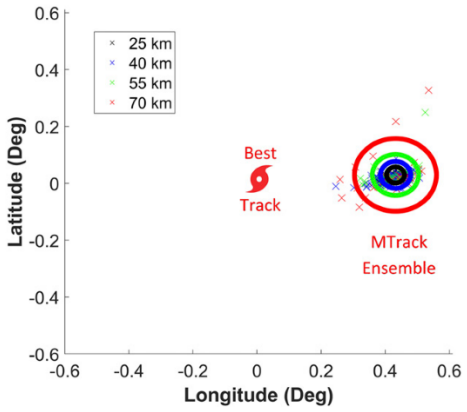

Figure 4-17: An MTrack storm center fix varies as the Best Track centers are perturbed. The perturbations are made with zero mean Gaussians with standard deviations of 25, 40, 50, and 70 km. As the perturbations grow larger, the spread of the MTrack centers (given by 'x's) increases as well. However, the variance of the MTrack fixes is small compared with the variance of the Best Track fixes. This shows that the solution is not affected much by the Best Track fixes.

An example of MTrack performance with CYGNSS wind speeds is Hurricane Jose at a 3-hour interval centered on 17 September 2017 at 2015 UTC. The corresponding MTrack fix was

computed in the previous section. This case is reconsidered with larger perturbations in the Best Track fixes. The standard deviation of the perturbations is increased from 10 km to 25, 40, 55 and 70 km. These values correspond to the levels of uncertainty in the Best Track fix associated with varying levels of storm organization and with the different types of observations used to produce the fix. An ensemble of 100 trials was assembled for each value of standard deviation. The resulting distributions of individual CYGNSS storm center fixes are shown graphically in Figure 4-17. The red symbol in the figure is the storm center estimated by linear interpolation of the unperturbed Best Track fixes without consideration of the CYGNSS measurements. As the perturbations grow larger, the spread of the resulting MTrack fixes becomes greater, but the average of the fixes remains the same. The MTrack uncertainty and uncertainty reduction factor are computed from the ensembles in Figure 4-17. The results are tallied in Table 4-2. The MTrack uncertainty increases monotonically with that of the NHC fix and the ratio between the two (the uncertainty reduction factor) is relatively constant once the NHC uncertainty is 25 km or greater. This suggests that the MTrack algorithm produces a consistent improvement in confidence even at the highest values of NHC uncertainty.

Perturbation std dev (km)	Uncertainty of fix (km)	Uncertainty reduction factor
10	1.73	5.78
25	3.10	8.06
40	5.49	7.28
55	6.77	8.12
70	7.45	9.39

Table 4-2: The MTrack uncertainty and uncertainty reduction factor (compared with Best Track) for each of the ensembles in Figure 4-17. As the perturbations grow larger, the MTrack uncertainty also becomes larger. However, MTrack produces a consistent improvement in confidence compared with Best Track for even the largest perturbations.

The above performance assessment was repeated for other storm cases: Hurricane Sergio on 7 Oct 2018 at 1200 UTC; Hurricane Maria on 17 Sept 2017 at 2300 UTC; Hurricane Jose on

16 Sept 2017 at 1830 UTC; Hurricane Florence on 12 Sept 2018 at 1730 UTC. These cases were chosen because they are well-sampled by CYGNSS and are on the weaker end of the hurricane spectrum (Category 1-3). The MTrack uncertainty and uncertainty reduction factor in each case are listed in Table 4-3 for a Best Track fix uncertainty of 40 km (a typical uncertainty value according to (Landsea and Franklin 2013)). The resulting MTrack uncertainties range from 5.49 km to 8.97 km and the average uncertainty reduction factor across all storm cases is 5.56. The variation in MTrack uncertainty is likely due to several factors, including differences in CYGNSS sampling density and distribution, degree of storm organization, and storm center movement during the time interval of data collection.

Case	MTrack uncertainty (km)	Uncertainty reduction factor	Hurricane category
Hurricane Jose at 2015 UTC 17 Sep 2017	5.49	7.28	1
Hurricane Maria at 0030 UTC 18 Sep 2017	8.97	4.46	1
Hurricane Sergio at 1330 UTC 7 Oct 2018	7.61	5.25	2
Hurricane Jose at 2000 UTC 16 Sep 2017	8.26	4.84	1
Hurricane Florence at 1900 UTC 12 Sep 2018	6.68	5.98	3

Table 4-3: MTrack performance metrics with CYGNSS wind speeds as input for five cases. The hurricane category, according to the Saffir Simpson scale, is included because there is a correlation between storm intensity and center fix accuracy. The uncertainty reduction factor is much greater than 1 in all cases, meaning that MTrack always has a much lower uncertainty than Best Track.

The MTrack uncertainty has thus far been considered as a scalar, averaged over all directions without regard for possible azimuthal dependence. As Figure 4-17 suggests, however, there is an asymmetric spread in the individual storm center fixes about the ensemble average. The asymmetry manifests itself as a larger uncertainty in the component of the storm center fix that is perpendicular to the direction of storm center motion (henceforth referred to as cross-path). The component of uncertainty parallel to the direction of storm center motion, or along-path, is typically one to two times smaller. Table 4-4 summarizes the cross-path/along-path asymmetry in uncertainty for several cases considered. In all cases, the cross-path uncertainty is greater than the along-path uncertainty, with the ratio varying between 1.3 and 2.2. The

asymmetry appears to stem from a similar asymmetry in the residual surface and is directly related to the wind field measured by CYGNSS.

Case	MTrack uncertainty (km)	Ratio of cross-path uncertainty to along-path uncertainty
Hurricane Jose at 2015 UTC 17 Sep 2017	5.49	1.29
Hurricane Maria at 0030 UTC 18 Sep 2017	8.97	1.49
Hurricane Sergio at 1330 UTC 7 Oct 2018	7.61	1.54
Hurricane Jose at 2000 UTC 16 Sep 2017	8.26	2.16
Hurricane Jose at 0500 UTC 9 Sep 2017	22.4	1.35
Typhoon Shanshan at 1915 UTC 7 Aug 2018	18	1.72

Table 4-4: Comparison of cross-path and along-path uncertainty. The cross-path uncertainty is greater than the along-path uncertainty in all cases. This seems to stem from a similar eccentricity in the residual surface

MTrack performance was also examined with respect to the uncertainty in the CYGNSS wind speeds themselves via another Monte Carlo simulation. For each of 100 trials, CYGNSS wind measurements were perturbed by zero mean Gaussian random noise with standard deviation given by the uncertainty value reported in the wind speed data files. For more information on how CYGNSS uncertainties are determined, see (Gleason et al. 2019) and (Ruf, Gleason, and McKague 2019). The storm center was estimated for each trial, and the standard deviation of the fix was computed for the 100 trials. This process was done for the 5 cases previously described. Table 4-5 summarizes the results. The standard deviation ranges from 3 to 9 km for these cases, with an average value of 5.7 km. This represents the uncertainty in MTrack due to CYGNSS wind speed measurement uncertainty, suggesting that the wind speed measurement noise introduces little if any bias in the MTrack fix.

Case	Uncertainty (km)
Hurricane Maria at 0045 UTC 20 Sep 2017	3.71
Hurricane Jose at 2015 UTC 17 Sep 2017	4.94
Hurricane Maria at 0030 UTC 18 Sep 2017	5.11
Hurricane Sergio at 1330 UTC 7 Oct 2018	4.64
Hurricane Jose at 2000 UTC 16 Sep 2017	7.33
Hurricane Florence at 1900 UTC 12 Sep 2018	9.01

Table 4-5: MTrack uncertainties due to CYGNSS wind speed errors for a few cases. The CYGNSS wind speeds were randomly perturbed over many trials, and the average error which propagated to MTrack is in this table.

4.4 Future Use of MTrack

One potential use of MTrack is to create a database of TC properties. For example, each time a satellite makes an overpass of a TC, its wind speed measurements can be used as input to MTrack and a storm center location is determined. Data can be used from any satellite which measures wind speed, and wind speed measurement from different platforms can be combined as input to MTrack. Automatic quality control using the shape of the residual error map and the residual between satellite wind speeds and the best-fit model wind speeds can determine the confidence in the fix. Each MTrack center fix also generates parameters that characterize the TC wind field such as the maximum wind speed, radius of maximum wind speed, and azimuthal variation characteristics. These storm parameters can be reported along with the satellite wind speed product. They can also be used to generate a gridded wind speed product of the storm, even if the overpass coverage is incomplete. The above can be done at regular time intervals (e.g. every 6 hours) using surface wind speed input from many different satellites for each MTrack fix.

MTrack can also assist expert forecasters at an agency such as the National Hurricane Center (NHC) to make a center fix decision. In this scenario, MTrack would be one of many tools available to the forecaster. The MTrack center fix would be automated, but there needn't be automatic quality control. Instead, an expert user could look at the satellite-measured wind field, the MTrack residual error map, and the MTrack reconstructed wind field. In a typical case, the MTrack residual error map has a well-defined minimum residual with increasing error on all sides (e.g. the middle panel of Figure 4-2). The depth and size of this minimum are indications of the confidence in the MTrack center fix solution. Next, the forecaster could compare the satellite-measured wind field to the MTrack reconstructed wind field. In a typical case, the

MTrack wind field which is generated from the best-fit parametric wind model will look very similar to the measured wind field. If there are large differences in wind structure, it is likely that the complex wind field was not well-represented by the parametric wind model (e.g. Figure 4-6). In this case, it is possible that the MTrack center fix is accurate, but it is not a guarantee because the model does not agree with the measurements. In this way, an expert user can look at these three components of an MTrack output to determine how much confidence to place in the storm center solution when comparing it to information from other available tools and data.

Chapter 5 New CYGNSS Level 3 Gridded Wind Speed Product with Storm-Centric Averaging

A Level 3 wind speed product takes the individual Level 2 wind speed measurements and organizes them in a regular grid. If a grid cell contains multiple measurements, these measurements are combined into one wind speed estimate through some sort of average. The primary purpose of a gridded product is to report the wind speed estimates in a way that is easier for data users. The existing CYGNSS Level 3 wind speed product divides the Earth into a 0.2x0.2-degree grid. All wind speed samples which fall into a grid cell in an hour are combined via an inverse-variance weighted average of the wind speeds (Ruf 2018). This product is available globally and is only restricted to where CYGNSS can make wind speed measurements.

In contrast, the new CYGNSS Level 3 wind speed product with storm-centric averaging described here is only available near tropical cyclones (TCs). The primary function of this new product is to use inter-track comparisons to identify and remove outlier tracks while reporting wind speeds in a way that is most convenient for users focused on TC winds. Note that a track is defined as a particular combination of GPS and CYGNSS satellite whose specular point on the ocean's surface traces a continuous curved path or 'track'. Inter-track comparisons are valuable if a GPS/CYGNSS satellite combination has an unforeseen bias or calibration issue. To perform inter-track comparisons, samples from multiple tracks must fall within a grid cell. For the standard CYGNSS Level 3 product, there are typically between 1 and 4 samples in each grid cell, as shown in Figure 5-1. 1-4 samples typically corresponds to just one track, but occasionally

there is a second track depending on the orientations of the tracks relative to the center of the cell.

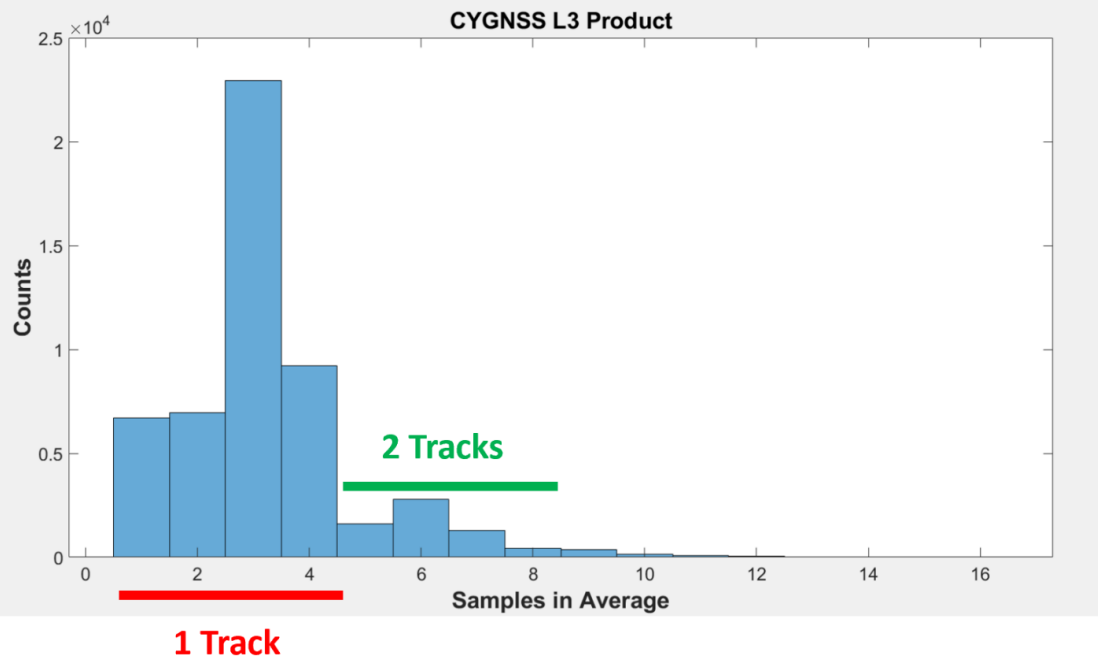

Figure 5-1: Histogram of number of wind speed samples per cell in the original global CYGNSS dataset (not the TC product). Most cells contain samples from only 1 track, so the averaged wind speed of the cell is simply along-track averaging.

More than 4 samples in a cell indicates 2 or more tracks in the cell. Figure 5-1 indicates that the primary function of the standard L3 product is along-track averaging because very few grid cells contain samples from multiple tracks. Along-track averaging reduces the effective spatial resolution of the reported wind speed while reducing noise in the measurement, but it does nothing to check for bias in the track. Even when there are multiple tracks present, there is no inter-track comparison to see if the tracks agree—the wind speeds from each track are simply averaged together using the inverse-variance weighted average. There is an opportunity for a more complex algorithm which combines the CYGNSS measurements in a smarter way, providing the users with more confidence in the reported wind speed values.

5.1 Establishing a Storm-Centric Grid

The spatial averaging window is defined as the extent of the region from which CYGNSS samples are drawn for a particular grid cell. Note that this is different from the reporting interval (Figure 5-2). The reporting interval is a 0.2-degree box in latitude/longitude, just like the original CYGNSS Level 3 product. For each grid cell, samples are taken from a +/- 0.4-degree latitude/longitude box (0.8 deg spatial averaging window) to populate the cell. This means there is overlap between cells, i.e., the same CYGNSS samples are used in multiple grid cells. The spatial averaging window must be wide enough such that many grid cells contain multiple tracks for inter-track comparisons, but it should not be too wide because spatial information about the wind field must be preserved. This tradeoff determined the size of the spatial averaging window: 0.8 degrees.

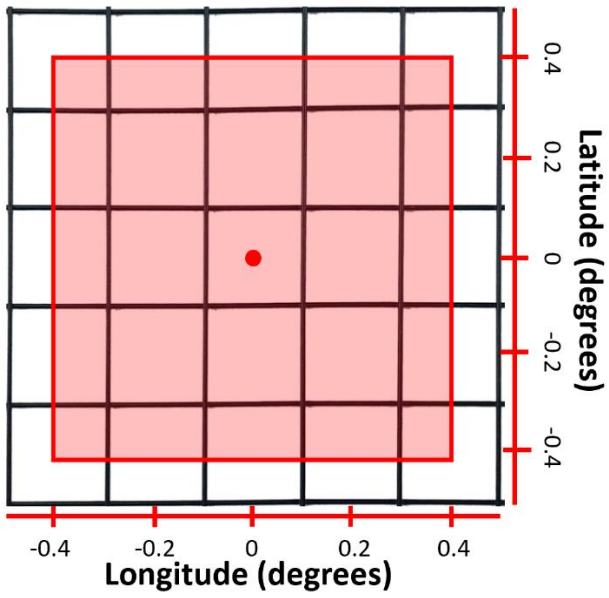

Figure 5-2: The red dot is the center of an arbitrary grid cell. The reporting interval is 0.2 degrees and is represented by the black squares. Each black square is a different grid cell which contains its own set of CYGNSS samples and its own averaged wind speed. The red square represents the spatial averaging window: the 0.8 deg x 0.8 deg area from which the center grid cell derives its CYGNSS samples.

Another way to increase the average number of tracks per cell is to increase the temporal averaging window. The temporal averaging window defines the duration of time over which samples are combined to provide a single wind speed estimate for each cell. For example, a 12-hour temporal averaging window means that samples from 6 hours before and 6 hours after the grid's reported time will be combined. Again, note that this is different from the time between reported wind speed grids. Wind speed grids are reported every 6 hours while each of those grids contains wind speeds from a 12-hour temporal averaging window. This means that the same CYGNSS samples contribute to multiple wind speed grids. The standard CYGNSS Level 3 product has a one-hour window which is the maximum allowable window without smearing the wind field. A typical TC travels around 20 km per hour (Lanzante 2019), so it travels the width of the standard grid cell size (0.2 degrees or about 23 km) in an hour. Any widening of the one-hour window would smear the wind field. The use of storm-centric coordinates allows for widening of the temporal window while minimizing smearing effects (Figure 5-3).

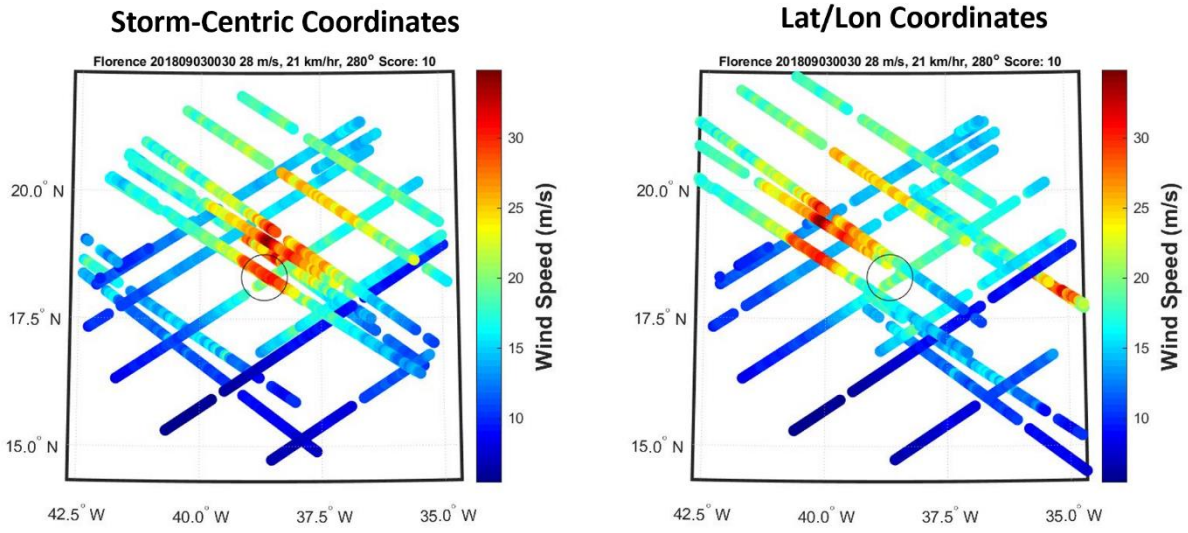

Figure 5-3: CYGNSS wind speeds in Hurricane Florence from a 24-hour duration centered on 03 September 2018 at 00:30 UTC. The left image is plotted in storm-centric coordinates while the right image is plotted with the regular latitude/longitude of each wind speed. When the movement of the storm is not accounted for, the storm structure is smeared over time. A 24-hour window is used to exaggerate this effect for illustrative purposes.

Storm-centric coordinates use (r, ϕ) pairs instead of (latitude, longitude) pairs to locate a sample, where r is the distance from the storm center and ϕ is the azimuth angle relative to north of the storm center. By definition, a storm-centric coordinate system requires knowledge of a storm center location that varies continuously in time. The official NHC TC records (Best Tracks) include a 6-hourly storm center location which is available at 0, 6, 12 , 18, and 24 UTC (Knapp et al. 2010). The Best Track fixes are linearly interpolated to provide a continuous storm center location for each storm.

Each 6-hourly grid is populated in storm-centric coordinates with a 12-hour temporal averaging window, a 0.8-degree spatial averaging window, and a 0.2-degree reporting interval. To be precise, this means that all samples +/- 6 hours from the center time and +/- 0.4 degrees from the grid center are included together. The combination of the larger spatial averaging window and the wider temporal window typically allows for multiple tracks to be present in each cell. Figure 5-4 shows that, with the new gridding process, there are typically 20-60 samples per cell or 2-5 tracks per cell. Compare this to Figure 5-1 which shows that the standard Level 3 product usually contains only 2-4 samples per cell and these samples are typically from only 1 track. In the new Level 3 gridded wind speed product, there are 2 or more tracks in a cell 66% of the time (of cells which contain at least one CYGNSS sample).

The co-location of multiple tracks allows for powerful inter-track comparisons and quality control to make sure that each reported L3 wind speed is an average of samples that come from consistent tracks. The inter-track comparison process varies depending on the number of tracks in a grid cell.

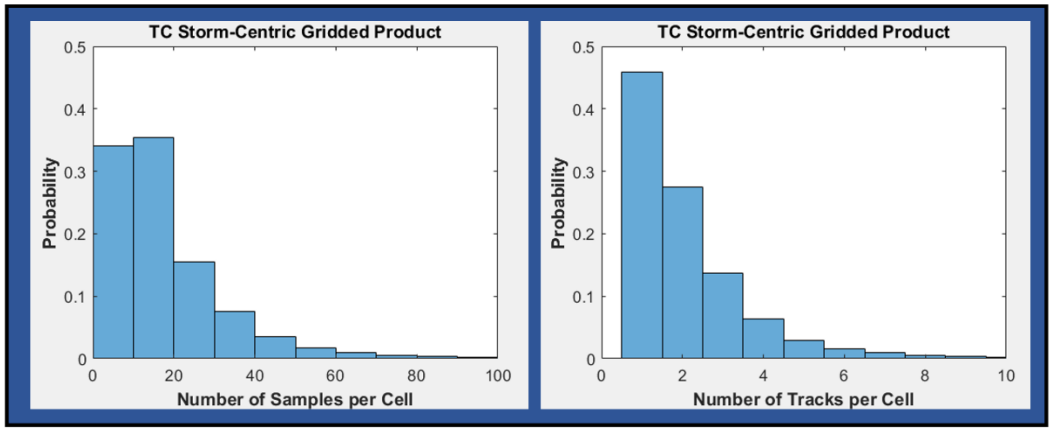

Figure 5-4: The probabilities of the number of wind speed samples and tracks per grid cell in the TC storm-centric gridded product. Compared with the original CYGNSS global gridded wind speed product (Figure 5-1), there are now many more wind speeds in each cell which allows for more complex quality control. This image was generated using a temporal averaging window of +/- 6 hours and data is collected from a +/- 0.4-degree area for each grid cell.

5.2 Inter-Track Comparisons and Averaging

Inter-track comparisons are performed for each grid cell before reporting a wind speed value to ensure reliability of the data. The reported wind speed of a cell and the handling of multiple tracks is determined by the number of tracks, *T*, in the cell. Each cell must contain wind speed measurements ("samples") from at least two tracks for a cell-averaged wind speed to be reported. If there is only one track in a cell, then a consistency check is not possible and there is no way to verify that the wind speeds for that track are not problematic. When there are two tracks or more in the cell, the mean track wind speed $\bar{u}_t$ is computed for each track. There are *N* samples in the cell and *T* tracks with N_t samples in the t^{th} track. The mean track wind speed for the t^{th} track is given by

$$\bar{u}_t = \frac{1}{N_t}\sum_{j=1}^{N_t} u_j \tag{5.1}$$

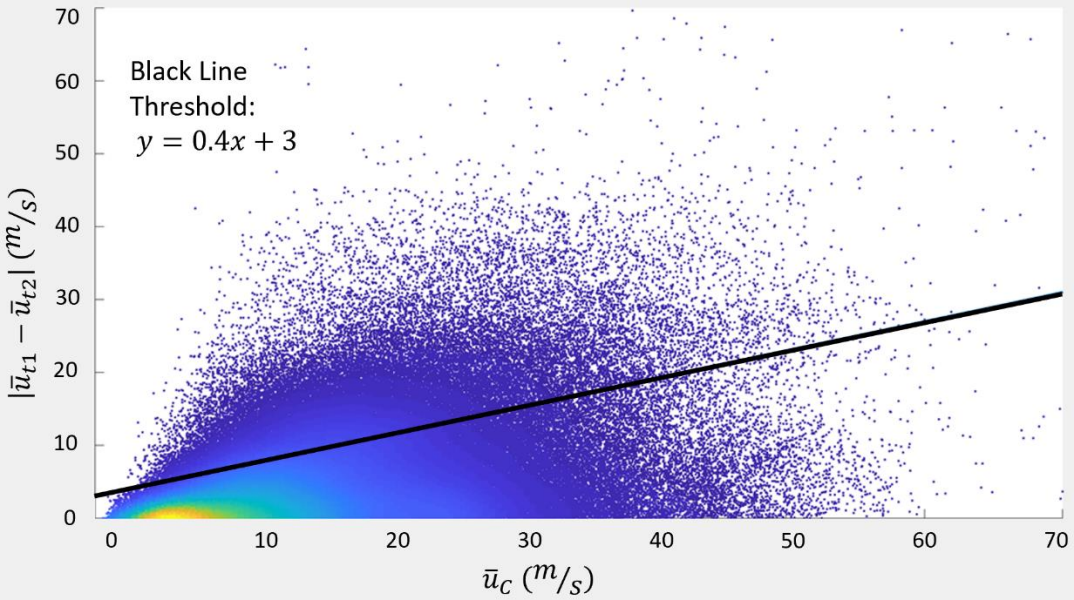

Figure 5-5: When there are 2 tracks in a cell, the black line is a threshold for whether tracks agree well enough to report a wind speed for the cell. The scatter plot is the difference between the two mean track wind speeds against the average wind speed of the cell for all storms in CY2018. For those cases, 80% of 2-track cells are within the threshold.

where u_j is the wind speed of the j^{th} sample in the t^{th} track. All wind speeds within a cell are averaged to give the mean cell wind speed $\bar{u}_C$:

$$\bar{u}_C = \frac{1}{N}\sum_{t=1}^{t=T} N_t \bar{u}_t \tag{5.2}$$

For the case $T = 2$ when there are two tracks in a cell, the mean track wind speeds $\bar{u}_t$ should be compared to see how well the tracks agree. It is expected that the difference between the two mean track wind speeds tends to be larger when higher wind speeds are present. To account for this, the difference between the mean track wind speeds $|\bar{u}_{t1} - \bar{u}_{t2}|$ is plotted against the mean cell wind speed $\bar{u}_C$ in Figure 5-5. As expected, the difference $|\bar{u}_{t1} - \bar{u}_{t2}|$ tends to increase with $\bar{u}_C$. To exclude cells which do not agree, we must establish a threshold or come up with a systematic way to remove cells which contain tracks with a large mean track wind speed difference. The first attempt to do this involved color coding Figure 5-5 as either green or red

representing good or bad data, where good/bad is determined by HWRF matchups with mean cell wind speeds $\bar{u}_C$. There was no clustering of "bad" cells or any sort of distribution of bad cells which allows for a large fraction of bad data to be removed while keeping most of the good data. This process was repeated for a few different classifications of good/bad data based on CYGNSS and HWRF matchups and there was still no way to separate the good and bad data based on the mean track wind speed difference $|\bar{u}_{t1} - \bar{u}_{t2}|$. The reason for this likely due to errors in the matchup process as well as the errors in the HWRF winds themselves. The lack of widely available truth data for wind speeds in TCs along with the difficulties of finding a large dataset of matchups that are close in time and space makes it difficult to classify data as "good" or "bad" based on matchups. Instead, the focus becomes forcing CYGNSS to be self-consistent within a grid cell. There is still a lot of value in ensuring that each reported wind speed in this data product combines at least two CYGNSS tracks which are shown to be self-consistent. This makes for a much more reliable data product.

Now, a threshold is chosen in Figure 5-5 to balance how many cells are thrown out with how different the tracks can be. The threshold is linear with $\bar{u}_C$ to allow for a larger difference between tracks at high wind speeds. For the case $T = 2$, $\bar{u}_{t1}$ must agree with $\bar{u}_{t2}$ to within the threshold

$$|\bar{u}_{t1} - \bar{u}_{t2}| < 0.4\bar{u}_C + 3 \tag{5.3}$$

The threshold in Eq. (5.3) is derived from Figure 5-5 which relates $|\bar{u}_{t1} - \bar{u}_{t2}|$ to $\bar{u}_C$. The data in Figure 5-5 is from all 2018 TCs. All data points below the black line, the threshold in Eq. (5.3), are considered to be in sufficient agreement. If the difference between the two mean track wind speeds is below the threshold, the mean cell wind speed $\bar{u}_C$ is reported as Eq. (5.2) directly above. If there is a large difference between two tracks and the difference exceeds the threshold,

no wind speed is reported for the cell because there is no way to determine if one, the other, or both tracks are problematic (this happens for 20% of 2-track cells).

When there are more than two tracks in a cell ($T > 2$), an outlier test is done to check if any mean track wind speeds $\bar{u}_t$ are anomalous. Track *x* is not an outlier if its mean track wind speed is within 3x standard deviations of the mean cell wind speed computed without track *x*. This is represented by the condition

$$\bar{u}_C^{-x} - 3\sigma_C^{-x} < \bar{u}_x < \bar{u}_C^{-x} + 3\sigma_C^{-x} \tag{5.4}$$

where the superscript -*x* indicates that track *x* is excluded when computing the term and where

$$\sigma_C^{-x} = \sqrt{\frac{1}{(T-1)-1}\sum_{t\neq x}|\bar{u}_t - \mu|^2} \tag{5.5}$$

and

$$\mu = \frac{1}{T-1}\sum_{t\neq x}\bar{u}_t \tag{5.6}$$

Any outlier tracks that are flagged by this method are removed from further consideration.

Before proceeding, the algorithm checks if the removal of outlier track(s) removed all the samples within +/- 3 hours. If there are no remaining samples within +/- 3 hours, no wind speed is reported for the cell. If a wind speed were reported in this case, it would be the same as the adjacent 6-hourly wind speed grid. This duplicated information is not useful to users. However, if there is one track within +/- 3 hours which agrees with another track more than 3 hours away, then a wind speed is reported since there is new information obtained in the +/-3 hours interval around the grid.

Next, the variation of the mean track wind speeds $\bar{\mu}_t$ is examined to see if the spread of the 3+ tracks is typical. This is done whether outliers were found or not. First, the expected standard deviation is computed from the relation

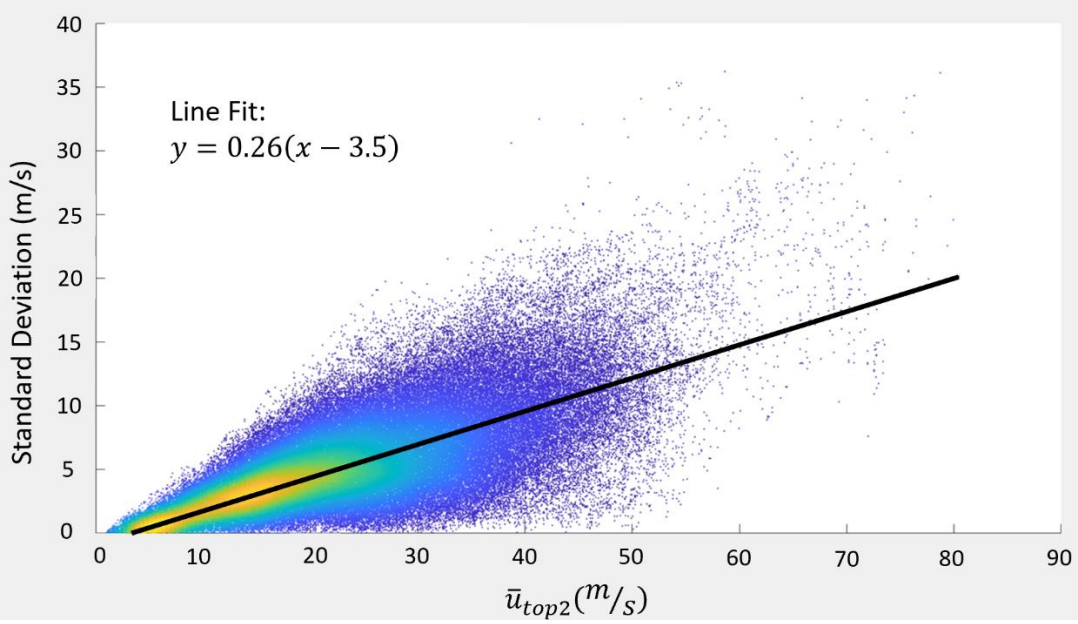

Figure 5-6: The standard deviation of the mean track wind speeds ($\bar{u}_t$) are plotted against the mean of the two highest mean track wind speeds for all 2018 storms. The line fit is used to estimate a typical standard deviation value given $\bar{u}_{top2}$. When there are 3+ tracks in a cell, this relation is used to determine whether the tracks agree well enough to report an averaged wind speed for that cell.

$$\sigma_{Expected} = 0.26\ x\ (\bar{u}_{top2} - 3.5) \tag{5.7}$$

where $\bar{u}_{top2}$ is the average of the two highest mean track wind speeds $\bar{\mu}_t$ after removal of outlier track(s). Eq (5.7) is derived from a best-fit line to data from the 2018 hurricane season which is shown in Figure 5-6. If the standard deviation of the mean track wind speeds is more than 3 m/s greater than the typical standard deviation estimated from Eq. (5.7), no wind speed is reported for the cell. This is expressed mathematically as

$$\sigma_C^{-Outliers} > \sigma_{Expected} + 3\ m/s \tag{5.8}$$

If the condition in Eq. (5.8) is not met, then the wind speed for the cell is reported as Eq (5.3) but with outlier track(s) excluded.

This inter-track comparison algorithm is done for all grid cells. When complete, a typical final gridded wind field looks like Figure 5-7. All empty cells in the square grid are due to less

than two tracks in a cell or inter-track quality control. A wind field like this is available every 6 hours near every TC.

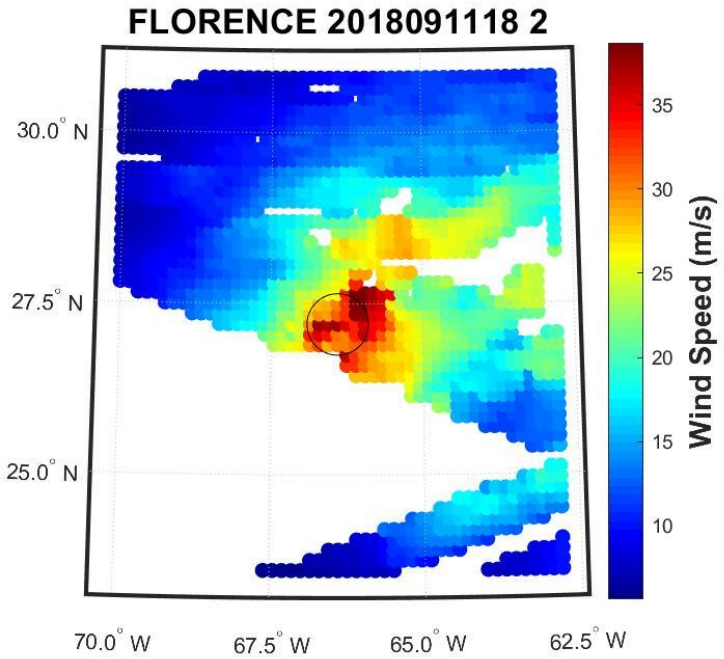

Figure 5-7: A typical storm-centric Level 3 gridded wind field which combines data from +/- 6 hours of the grid time. The grid spacing is 0.2 degrees with each cell taking data from +/- 0.4 degrees as in Figure 5-2. The black circle indicates the storm center location. The gaps are either cells which do not contain CYGNSS samples from multiple tracks or which have disagreement between tracks.

5.3 Performance Assessment

One way to assess how the CYGNSS Level 3 storm-centric gridded wind speeds perform in TCs is to compare the winds to a well-established data product. Figure 5-8 shows the CYGNSS wind speeds matched up with the inner nest of the HWRF wind field in 2018 TCs. Both CYGNSS and HWRF are available 6-hourly and HWRF wind fields are gap free. This seemingly makes the matchup process straightforward, but there are errors inherent in this process. The gridded CYGNSS wind speeds are derived from individual measurements over a

period of +/- 6 hours and measurements within a +/- 0.4-degree box are averaged together. These temporal and spatial differences can cause differences between CYGNSS and HWRF. The black line in Figure 5-8 is the 1-to-1 line which represents a perfect matchup. The black dots are median CYGNSS wind speeds in bins of width 10 m/s. These median values make it clear that CYGNSS tends to overestimate low wind speeds and underestimate high wind speeds. It should be noted that HWRF is a TC-specific product and is not very reliable below about 10 m/s. The CYGNSS underestimation at high wind speeds has been reported in other analyses, however (Ruf and Balasubramaniam 2019).

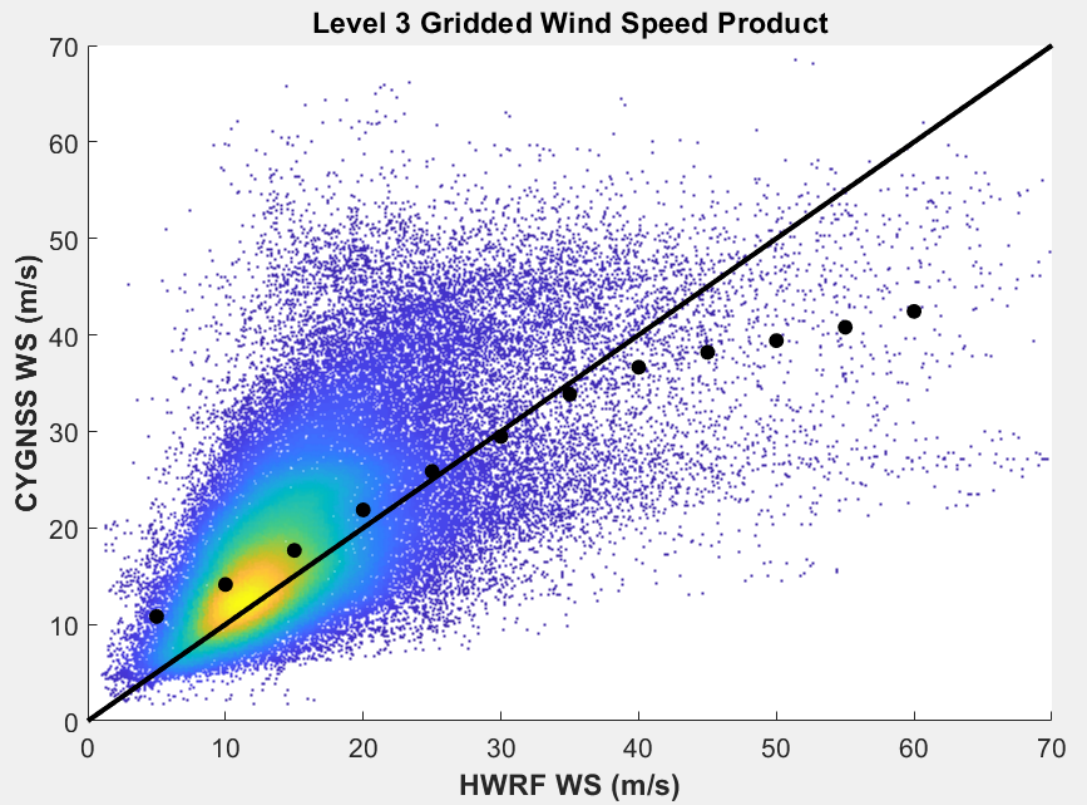

Figure 5-8: CYGNSS Level 3 gridded wind speeds with inter-track quality control matched up with model HWRF wind speeds in 2018 TCs. The black line is the 1-to-1 line which represents a perfect matchup. The black dots are the median CYGNSS wind speeds in bins of 10 m/s width that are spaced in 5 m/s intervals. CYGNSS tends to overestimate low wind speeds and underestimate high wind speeds.

There is considerable spread in these matchups which can be attributed to several factors. First, HWRF has its own uncertainties and is not “the truth”. For many storms, there is little knowledge of the wind field except for the maximum wind speed estimate from cloud top temperatures. Again, HWRF is not very accurate at low wind speeds. There are also errors in the conversion to storm-centric coordinates and the gridding process. There is significant spatial averaging due to the large grid cell size which can exacerbate the wind speed underestimation at high wind speeds. In the conversion to storm-centric coordinates, linear storm motion is assumed. Any deviation from linearity could cause errors, especially in regions where the wind speed is quickly changing (i.e., near the eyewall). Another error source is the temporal averaging window. Inter-track comparisons are performed, and samples are averaged together over a 12-hour time. Over these 12 hours, it is likely the wind field is changing. In extreme cases, rapid intensification of the storm can cause large differences between tracks. The inter-track quality control removes many of these large differences, but some of these instances can make it through quality control and introduce errors.

One of the primary benefits of using storm-centric coordinates and inter-track comparisons is the additional consistency it imposes on the reported wind speeds. The standard deviation of the wind speeds within each cell can be used to quantify the consistency of the winds which are used to generate the reported cell wind speed. Figure 5-9 shows the probability distribution function (PDF) for the standard deviation of individual wind speed samples which are averaged together to produce a grid cell’s wind speed before and after applying inter-track quality control. The average standard deviation is 4.53 without the inter-track quality control and this is reduced to 3.53 with inter-track QC applied. As outlier tracks are removed in the inter-track comparison process, the variance within each grid cell decreases. Because of this, there is a

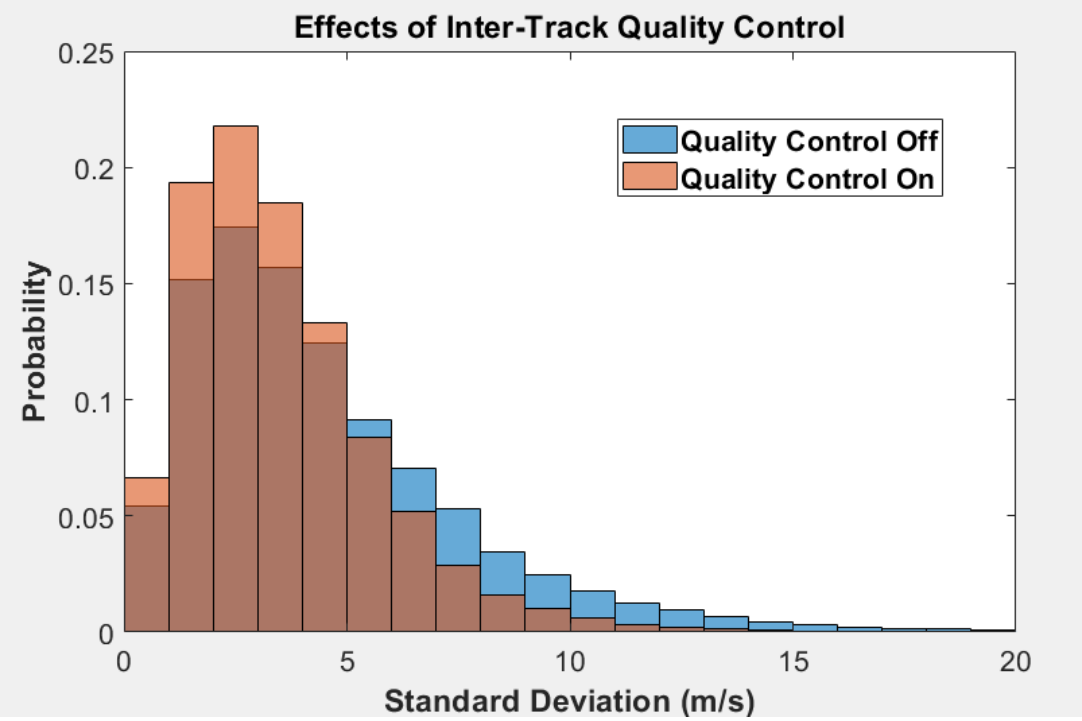

Figure 5-9: The probability distribution of wind speed standard deviation within a grid cell with 2 or more tracks. Each grid cell contains many wind speed measurements. The standard deviation of those wind speeds tends to be lower after the inter-track quality control is applied. The average standard deviation is 4.53 and 3.53 without and with quality control, respectively. The skewness is 1.85 without inter-track quality control and 1.40 with.

much smaller tail of high standard deviations in the distribution when inter-track quality control is applied. The skewness of the distribution decreases from 1.85 to 1.40 which means that more samples are closer to the mean and fewer are in the high standard deviation tail with inter-track quality control.

To check that this process of combining wind speeds in storm-centric coordinates is yielding reasonable results, comparisons with SMAP, which has been shown to be very reliable in measuring hurricane wind speeds (Meissner, Ricciadulli, and Wentz 2017), are provided. Figure 5-10 shows Hurricane Leslie at three different stages of its life. The top panel compares CYGNSS-measured wind speeds with SMAP-measured wind speeds on the morning of 28 September 2018. These wind fields are only three hours apart, so the storm is likely to have a

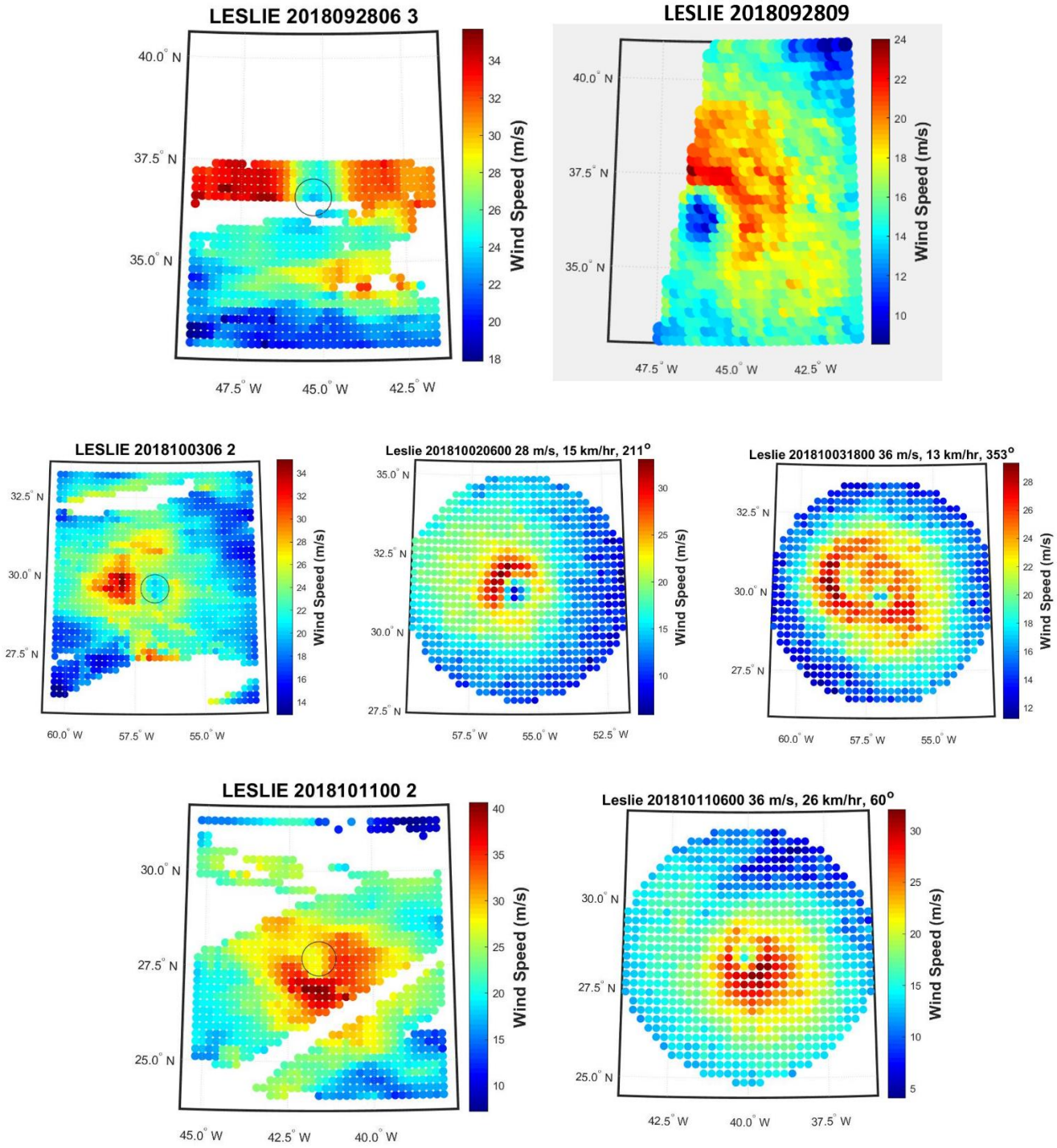

Figure 5-10: Comparisons of CYGNSS storm-centric gridded wind fields (left) and SMAP wind fields at similar times (right) for three cases of Hurricane Leslie. The middle case shows two SMAP wind fields at nearby times because there is not a SMAP wind field within 6 hours of the CYGNSS overpass. The black circle in the left figures represents the time-interpolated Best Track storm center location. The speed in m/s in the title of the figures on the right is the time-interpolated Best Track maximum sustained wind speed.

similar wind structure at the time of each overpass. A distinctive feature in the CYGNSS wind field is a very large eye. The SMAP wind field confirms that Leslie had a very large eye at this time, since it was able to make many measurements around 10 m/s near the center of the storm at 40 km spatial resolution. For many storms, the SMAP sensor is too coarse to resolve the eye, so it is significant that the eye appears so large in the SMAP wind field. SMAP also agrees with CYGNSS that the region of maximum wind speeds to the east of the eye has a slow roll-off rate. CYGNSS also captures the asymmetry in the southern part of the storm which is present in the SMAP wind field as well; the wind speeds are higher to the southeast than in the region directly south of the eye. These wind fields agree very well except in peak wind speed—CYGNSS shows maximum wind speeds of about 30 m/s on the east side of the storm while SMAP only measures wind speeds of about 22 m/s in that region. This overestimation of wind speed is consistent with Figure 5-8 which shows CYGNSS overestimating wind speeds compared with HWRF when the HWRF wind speed is around 20 m/s. At 6 UTC on 28 September 2018, Best Track estimates the maximum wind speed of Leslie to be 25 m/s, which is in agreement with SMAP.

The middle panel of Figure 5-10 shows Hurricane Leslie a few days later. The CYGNSS wind field is at 6 UTC on 3 October 2018. The two SMAP overpasses nearest in time are about 12 hours later and about 24 hours earlier. Though these time differences are significant, the SMAP wind fields support the storm structure shown by the CYGNSS wind field. CYGNSS measures the highest wind speeds to the west of the storm which is consistent with both SMAP overpasses. CYGNSS and SMAP (particularly the overpass on 2 Oct) both show lower wind speeds on the east side of the storm compared with the other regions. The one-minute average maximum wind speed according to Best Track is 31 m/s at the time of the CYGNSS overpass—this agrees well with the CYGNSS and SMAP measurements.

The bottom panel of Figure 5-10 shows Hurricane Leslie about a week later on 11 October 2018. The SMAP overpass is only a few hours later than CYGNSS so the storm's wind structure should be similar at these times. Again, the storm structures measured by SMAP and CYGNSS are in excellent agreement. The maximum wind speeds are to the south of the storm and there are lower wind speeds to the northwest of the eye. At this time, Best Track estimates a maximum wind speed of 36 m/s which falls between the SMAP and CYGNSS maximum values of 31 m/s and 40 m/s, respectively. CYGNSS also shows lower wind speeds far to the northeast of the storm compared with the far northwest part of the storm—this trend is also seen in the SMAP winds.

The excellent agreement between SMAP and CYGNSS wind fields and measured storm structures gives confidence to the process used to combine the CYGNSS measurements in storm-centric coordinates. Both satellite sensors are able to capture the evolution of Hurricane Leslie over a two-week period while maintaining consistency with one another. There are many cases from other TCs where SMAP and CYGNSS show similar storm structure. For example, Figure 5-11 compares CYGNSS and SMAP overpasses on 27 September 2018 in the West Pacific Ocean for Typhoon Trami. These overpasses are very close in time, so the storm structure is expected to be similar. This CYGNSS overpass has quite a few gaps, but enough of the center of the storm is measured to see storm structure which strongly resembles the SMAP overpass. The SMAP wind field reveals a very large eye which also appears in the CYGNSS overpass. Again, the CYGNSS wind speeds do not get as low as SMAP in the eye because of the size of the grid cells (+/- 0.4 degrees). SMAP and CYGNSS agree that Trami has higher wind speeds in the northeast part of the storm compared with the southwest region. The maximum wind speed at this time is 46 m/s. CYGNSS and SMAP both measure a maximum wind speed of about 41 m/s.

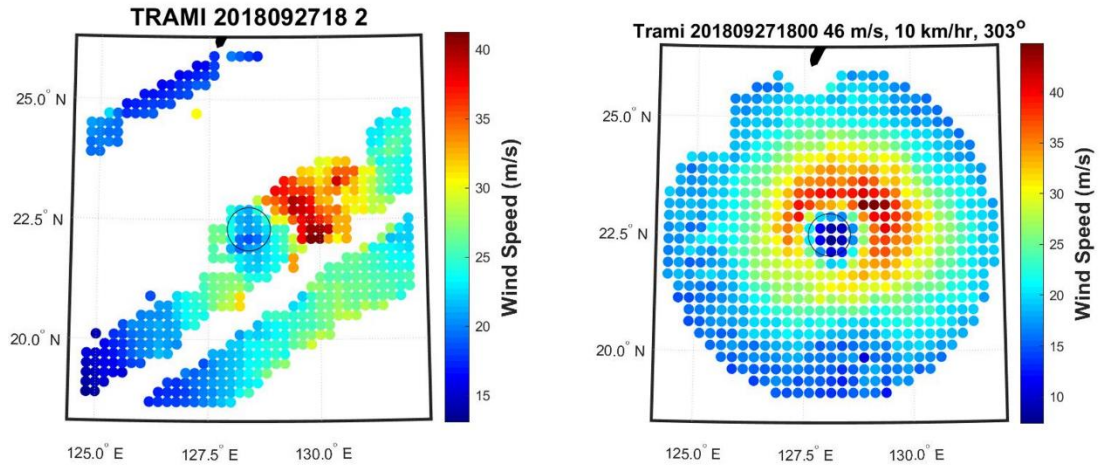

Figure 5-11: The CYGNSS storm-centric TC gridded wind speed product (left) shows a storm structure which is very similar to SMAP (right). Typhoon Trami is a very large storm with a huge eye at the time of measurement.

Figure 5-12 compares the SMAP and CYGNSS wind speed measurements of a very intense Hurricane Florence (Vm = 59 m/s) on the morning of 12 September 2018. SMAP measured a maximum wind speed of about 51 m/s which is only a slight underestimation at 40 km spatial resolution for such a small storm. CYGNSS, however, greatly underestimates Vm to be 36 m/s—this amount of underestimation is typical according to Figure 5-8. The wind field structure is very similar between SMAP and CYGNSS. Each overpass reveals a very small storm where the reduced wind speeds in the eye cannot be resolved, a small, concentrated region of high wind speeds, and the maximum wind speed is to the northeast of the storm.

Converting CYGNSS wind speeds to storm-centric coordinates, applying inter-track quality control, and averaging samples together allows for the removal of outlier tracks, improved noise resistance, and better overall consistency in the reported wind speeds. Figure 5-9 confirms that the wind speeds within each cell are much more consistent after inter-track quality control. This product is also in a format that is very convenient for users who are focusing on CYGNSS winds in TCs; wind speed grids are available 6-hourly (which allows for easy match

ups with other data products like HWRF) and in regular 0.2x0.2-degree grids. Figure 5-8 shows that the CYGNSS storm-centric TC product matches up reasonably well with HWRF wind speeds. Figure 5-10, Figure 5-11, and Figure 5-12 show examples where the CYGNSS storm-centric gridded wind speeds agree very well with SMAP to verify that this data processing chain yields reasonable wind fields. These examples are evidence that CYGNSS wind speeds over a +/- 6-hour time period can be combined in many cases. However, users of this data should remain cautious of storms which are rapidly intensifying. In cases where the storm is quickly changing, a greater fraction of CYGNSS data is thrown out due to tracks not agreeing. However, when high wind speed tracks are present, the cell is allowed a larger track variance before removal as seen in Figure 5-6. When a storm is rapidly intensifying, there is a greater possibility that a high wind speed track measured later in the time window is averaged together with lower wind speeds earlier in the time window.

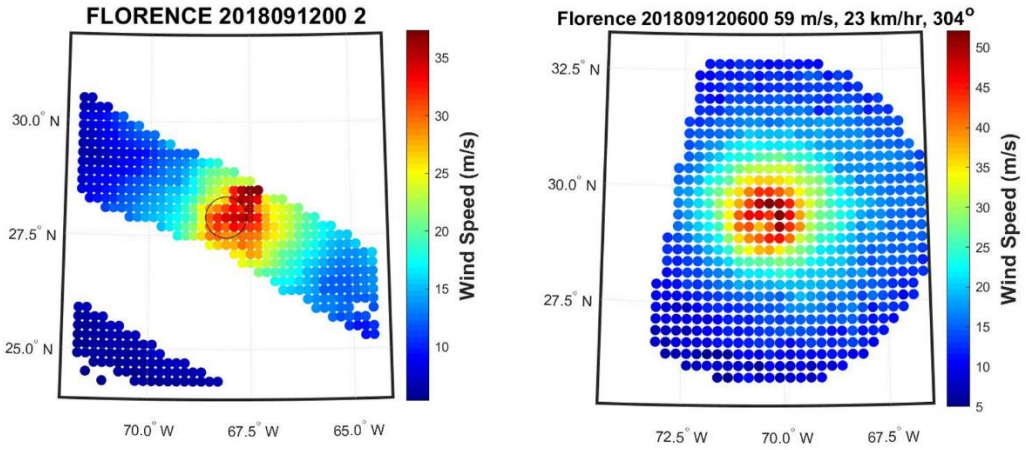

Figure 5-12: A CYGNSS wind field (left) compared with SMAP (right) for a very intense Hurricane Florence. CYGNSS and SMAP reveal similar surface wind speed structure, but CYGNSS greatly underestimates the intensity of the storm. This is typical of CYGNSS because of its reduced sensitivity to wind speed at high wind speeds.

The +/- 6-hour window, despite being shown to work well in many cases, is still larger than we hope to use in the future. This window size is necessary for the current CYGNSS

constellation to have enough wind speed measurements in each cell on average. Future missions, which have an even shorter revisit time than CYGNSS, may allow for a shorter temporal averaging window. If surface wind speed measurements from many platforms are combined, then the data density may allow for a shorter temporal averaging window as well.

This storm-centric TC gridded wind speed product will be publicly released to the NASA PODAAC in early 2021.

Chapter 6 Summary and Future Work

This dissertation looks at new ways to use and interpret remotely sensed wind speeds in tropical cyclones. First, we look at how estimated storm intensity is affected by the spatial averaging that occurs within the antenna. Storm intensity is often reported using the Saffir Simpson scale where intensity is determined by the one-minute-average maximum sustained wind speed (Vm). We find that the measured Vm is lower than the true Vm due to the coarse spatial resolution of the sensor. Without a proper correction, tropical cyclone (TC) intensity from satellite-measured wind speeds is systematically underestimated. A scale factor can be applied to the measured Vm to correct this underestimation; the scale factor is found to be a function of the measured radius of maximum wind speed (Rm) and the measured Vm (Mayers and Ruf 2020). This is a practical result which can be applied to any satellite which measures wind speed. This is the first time this topic has been explored—a similar topic of how to convert maximum sustained winds defined with respect to different temporal averaging intervals (e.g. between a 1- and 10-minute-averaged gust) is well-researched (Harper, Kepert, and Ginger 2010), but little has been done for spatial averages. The correction scale factor is most strongly related to Rm, but Rm is difficult to accurately determine from a measured wind field and it is not kept in the Best Track TC records. There is more work to be done to find a more accessible characteristic in the measured wind field which represents the size of the pocket of highest wind speeds and is strongly correlated with the intensity scale factor.

Next, TC parametric wind speed models are examined. Parametric wind models are established using meteorological principles combined with simplifying assumptions about the

environment or storm structure. These models tune several free parameters to wind speed measurements to minimize the difference between the measurements and the wind field "seen" by the model. Parametric wind models are especially useful for filling in gaps between measurements—once the free parameters are set, the model is able to report a wind speed estimate everywhere in the storm. Hurricane wind field characteristics such as maximum wind speed, radius of maximum wind speed, azimuthal information, and more are easily determined from a full wind field but are more difficult to estimate from a gap-filled wind field. Also, many modeling applications are enabled by having a full wind field. For example, models such as ADCIRC-2DDI require a full near-surface wind field to force the waves and simulate the surge. Without parametric wind models, this application and others would not be possible. Existing TC parametric wind models are very limited in how they can represent TCs. For example, all existing models assume azimuthal symmetry which is not true for any storm—it is a good approximation for only the most intense, well-organized TCs. I added an azimuthally varying scale factor which allows the model to accurately characterize simple azimuthal asymmetries in the wind field. Improved representation of the storm by the parametric model improves the performance of all applications including estimation of hurricane wind field characteristics and data assimilation research. In the future, more degrees of freedom could be added to the model to allow for even better fits. The azimuthal scale factor could be more complex than a simple first-order harmonic, or Rm, *a*, and *b* could be azimuthally dependent. Another approach is to use an arbitrary set of orthogonal functions instead of a parametric wind model which has a physical basis. The advantage to using a set of orthogonal function is that the degrees of freedom can be set to any value. This allows for the parametric model to extract as much information as possible from the measurements without overfitting. Another advantage to using orthogonal function is

that the errors in the parameter values are not correlated with one another. This approach could be used in the future with an input wind field such as SMAP which has a surplus of information compared with what is captured by the 6-parameter parametric wind model.

The parametric wind model is then used to find the center location of a TC using the principle that the model fit is best when the correct storm center is assumed, and the model fit is very poor at the wrong center location. By searching through a grid of all possible storm centers, the best storm center fix can be found at the minimum residual in the model fit (Mayers and Ruf 2019; 2021). Most storm center fixes are done manually—MTrack is one of few automated storm center fix techniques and the only one not using cloud structure seen in satellite imagery. MTrack could have improved performance when the cloud structure is poorly defined and in other cases when the other methods struggle. Accurate storm center locations are necessary for forecasting hurricanes, hurricane research, and historical record keeping. More analysis is needed to see how MTrack performance improves using the 6-parameter model instead of the 4-parameter model. There is also the potential that using a model with more than 6 parameters (i.e., with the improvements from the previous paragraph) could improve MTrack performance further.

When using MTrack with CYGNSS wind speeds, the largest source of error is the spatial density of wind speed samples. Wind speed measurements must be sufficient in both number and distribution to provide enough information to the parametric wind model for MTrack to find an accurate storm center location. It would be useful to have an automated way to determine if the CYGNSS sampling pattern is sufficient for MTrack and to estimate how much error should be expected due to the gaps in sampling. This analysis would require machine learning with many cases with different sample patterns to train the model. It would also require a model wind field

to be available. By running MTrack with the full wind field and with the wind field sampled by a CYGNSS-like sampling pattern, we can isolate the error due to sampling. Another situation which should be examined more closely is when there are gaps in sampling near the region of the maximum winds. Can the parametric model predict that there are higher wind speeds in the gap by using only the surrounding wind speeds? And how does this affect the accuracy of MTrack? This could be examined by carving out the high wind speed region of a model wind field and running the remaining winds through the parametric wind model and MTrack.

Lastly, a new CYGNSS data product (which will be released to the public in early 2021) is introduced which reports gridded surface wind speeds with increased convenience and reliability for users of tropical cyclone-specific data. The CYGNSS data is collected over a 12-hour window, converted to storm-centric coordinates, and organized into 0.2x0.2-degree grid cells. If the measured wind speeds in a grid cell are self-consistent to within the established thresholds, the grid cell reports a wind speed that is the average of all contained samples. Inter-track comparison methods and thresholds are described which lead to more reliability in the reported wind speeds. This Level 3 algorithm is able to gather enough co-located wind speeds to perform inter-track comparisons by using a very wide temporal window of +/- 6 hours. Further analysis is required to see how often large errors are induced by this window and if large errors can be predicted using metrics that track how quickly the storm is changing. For example, if a storm is undergoing rapid intensification, it is less likely that the 12-hour window would contain many self-consistent wind speeds. These errors could be predicted by looking at Vm in the Best Track files. Similarly, the wind radii (e.g. R34) could be monitored for rapid change in a storm's wind field. For now, users must be cautious of storms undergoing rapid change.

Another consideration with the Level 3 product is the grid cell size. The grid cells are very large (0.8x0.8-degree boxes which are about 100 km across on a diagonal). Work could be done to optimize the grid cell size by better balancing the tradeoff between spatial resolution and the number of cells with two or more tracks. Also, this grid cell size could be too large near the center of the storm. Wind speed changes very quickly near the eyewall so there could be cases where two CYGNSS tracks have very different wind speeds in the same cell and are removed by quality control, but the measurements are accurate and are only so different because they are 80 km apart near the eyewall.

Chapter 5 compares SMAP wind fields, which have been shown in the literature to be very reliable (Meissner, Ricciadulli, and Wentz 2017), to the CYGNSS storm-centric gridded wind fields. In many cases, CYGNSS and SMAP are in excellent agreement on the surface wind speed characteristics. This is evidence in support of the large temporal and spatial averaging windows used in processing the CYGNSS data.

All topics in this dissertation could be combined to construct a TC database. Wind speed measurements from all available sensors could be combined in storm-centric coordinates. The Level 3 gridded wind speed algorithm could perform a similar inter-satellite comparison before averaging wind speeds. The increased spatial density (due to the inclusion of many other platforms) would allow for a better parametric model fit and MTrack storm center fix. The inclusion of measurements from additional platforms could allow for wind speed grids to be reported more frequently or for the temporal window to be smaller. Currently, the +/- 6-hour window is too large for certain storms which are changing quickly. Every 6 hours (or less), a storm-centric gridded wind field would be available along with an MTrack storm center fix,

parametric model best-fit parameters, and wind field metrics such as storm intensity and wind radii. All this information in one place would be very useful for forecasters and researchers alike.

Bibliography

Bacmeister, Julio T., Kevin A. Reed, Cecile Hannay, Peter Lawrence, Susan Bates, John E. Truesdale, Nan Rosenbloom, and Michael Levy. 2018. "Projected Changes in Tropical Cyclone Activity under Future Warming Scenarios Using a High-Resolution Climate Model." *Climatic Change* 146 (3–4): 547–60. https://doi.org/10.1007/s10584-016-1750-x.

Biswas, Mrinal, Laurie Carson, Kathryn Newman, Don Stark, Evan Kalina, Evelyn Grell, and James. Frimel. 2018. "Community HWRF Users' Guide v4.0a." https://dtcenter.org/community-code/hurricane-wrf-hwrf/documentation.

Bosma, Christopher D., Daniel B. Wright, Phu Nguyen, James P. Kossin, Derrick C. Herndon, and J. Marshall Shepherd. 2020. "An Intuitive Metric to Quantify and Communicate Tropical Cyclone Rainfall Hazard." *Bulletin of the American Meteorological Society* 101 (2). https://doi.org/10.1175/BAMS-D-19-0075.1.

Chavas, Daniel R., Ning Lin, and Kerry Emanuel. 2015. "A Model for the Complete Radial Structure of the Tropical Cyclone Wind Field. Part I: Comparison with Observed Structure." *Journal of the Atmospheric Sciences* 72 (9): 3647–62. https://doi.org/10.1175/JAS-D-15-0014.1.

Chen, Tsing Chang, Shih Yu Wang, and Adam J. Clark. 2008. "North Atlantic Hurricanes Contributed by African Easterly Waves North and South of the African Easterly Jet." *Journal of Climate* 21 (24): 6767–76. https://doi.org/10.1175/2008JCLI2523.1.

Chew, Clara, John T. Reager, and Eric Small. 2018. "CYGNSS Data Map Flood Inundation during the 2017 Atlantic Hurricane Season." *Scientific Reports* 8 (1): 1–8. https://doi.org/10.1038/s41598-018-27673-x.

Chew, Clara, and Eric Small. 2018. "Soil Moisture Sensing Using Spaceborne GNSS Reflections: Comparison of CYGNSS Reflectivity to SMAP Soil Moisture." *Geophysical Research Letters* 45 (9): 4049–57. https://doi.org/10.1029/2018GL077905.

———. 2020. "Description of the UCAR/CU Soil Moisture Product." *Remote Sensing* 12 (10). https://doi.org/10.3390/rs12101558.

Clarizia, Maria Paola, Nazzareno Pierdicca, Fabiano Costantini, and Nicolas Floury. 2019. "Analysis of Cygnss Data for Soil Moisture Retrieval." *IEEE Journal of Selected Topics in Applied Earth Observations and Remote Sensing* 12 (7): 2227–35. https://doi.org/10.1109/JSTARS.2019.2895510.

Clarizia, Maria Paola, and Christopher S. Ruf. 2016. "Wind Speed Retrieval Algorithm for the

Cyclone Global Navigation Satellite System (CYGNSS) Mission." *IEEE Transactions on Geoscience and Remote Sensing* 54 (8). https://doi.org/10.1109/TGRS.2016.2541343.

Clarizia, Maria Paola, Christopher S. Ruf, Philip Jales, and Christine Gommenginger. 2014. "Spaceborne GNSS-R Minimum Variance Wind Speed Estimator." *IEEE Transactions on Geoscience and Remote Sensing* 52 (11). https://doi.org/10.1109/TGRS.2014.2303831.

Cui, Zhiqiang, Zhaoxia Pu, Vijay Tallapragada, Robert Atlas, and Christopher S. Ruf. 2019. "A Preliminary Impact Study of CYGNSS Ocean Surface Wind Speeds on Numerical Simulations of Hurricanes." *Geophysical Research Letters* 46 (5). https://doi.org/10.1029/2019GL082236.

DeMaria, M., J. A. Knaff, and C. Sampson. 2007. "Evaluation of Long-Term Trends in Tropical Cyclone Intensity Forecasts." *Meteorology and Atmospheric Physics* 97 (1–4): 19–28. https://doi.org/10.1007/s00703-006-0241-4.

Donelan, M. A., B. K. Haus, Nicolas Reul, W. J. Plant, M. Stiassnie, H. C. Graber, O. B. Brown, and E. S. Saltzman. 2004. "On the Limiting Aerodynamic Roughness of the Ocean in Very Strong Winds." *Geophysical Research Letters* 31 (18). https://doi.org/10.1029/2004GL019460.

Draper, David W., and David G. Long. 2002. "An Assessment of SeaWinds on QuikSCAT Wind Retrieval." *Journal of Geophysical Research: Oceans* 107 (12). https://doi.org/10.1029/2002jc001330.

Durden, Stephen L., and Dragana Perkovic-Martin. 2017. "The RapidScat Ocean Winds Scatterometer: A Radar System Engineering Perspective." *IEEE Geoscience and Remote Sensing Magazine*. https://doi.org/10.1109/MGRS.2017.2678999.

Dvorak, Vernon F. 1975. "Tropical Cyclone Intensity Analysis and Forecasting from Satellite Imagery." *Monthly Weather Review* 103 (5). https://doi.org/10.1175/1520-0493(1975)103<0420:TCIAAF>2.0.CO;2.

Emanuel, Kerry. 2010. "Tropical Cyclone Energetics and Structure." In *Atmospheric Turbulence and Mesoscale Meteorology*, 165–92. https://doi.org/10.1017/cbo9780511735035.010.

Emanuel, Kerry, and Fuqing Zhang. 2016. "On the Predictability and Error Sources of Tropical Cyclone Intensity Forecasts." *Journal of the Atmospheric Sciences* 73 (9): 3739–47. https://doi.org/10.1175/JAS-D-16-0100.1.

Entekhabi, Dara, Eni G. Njoku, Peggy E. O'Neill, Kent H. Kellogg, Wade T. Crow, Wendy N. Edelstein, Jared K. Entin, et al. 2010. "The Soil Moisture Active Passive (SMAP) Mission." *Proceedings of the IEEE* 98 (5). https://doi.org/10.1109/JPROC.2010.2043918.

Figa-Saldaña, J., J. J.W. Wilson, E. Attema, R. Gelsthorpe, M. R. Drinkwater, and A. Stoffelen. 2002. "The Advanced Scatterometer (Ascat) on the Meteorological Operational (MetOp) Platform: A Follow on for European Wind Scatterometers." *Canadian Journal of Remote Sensing* 28 (3). https://doi.org/10.5589/m02-035.

Gaiser, Peter W., Karen M. St. Germain, Elizabeth M. Twarog, Gene A. Poe, William Purdy, Donald Richardson, Walter Grossman, et al. 2004. "The WindSat Spaceborne Polarimetric Microwave Radiometer: Sensor Description and Early Orbit Performance." *IEEE Transactions on Geoscience and Remote Sensing* 42 (11). https://doi.org/10.1109/TGRS.2004.836867.

Galvin, J.F.P. 2015. *An Introduction to the Meteorology and Climate of the Tropics*.

Gleason, Scott. 2006. "Remote Sensing of Ocean, Ice and Land Surfaces Using Bistatically Scattered GNSS Signals from Low Earth Orbit." *Ph. Thesis from University of Surrey*.

Gleason, Scott, Christopher S. Ruf, Andrew J. O'Brien, and Darren S. McKague. 2019. "The CYGNSS Level 1 Calibration Algorithm and Error Analysis Based on On-Orbit Measurements." *IEEE Journal of Selected Topics in Applied Earth Observations and Remote Sensing* 12 (1). https://doi.org/10.1109/JSTARS.2018.2832981.

Goldenberg, Stanley B., Sundararaman G. Gopalakrishnan, Vijay Tallapragada, Thiago Quirino, Frank Marks, Samuel Trahan, Xuejin Zhang, and Robert Atlas. 2015. "The 2012 Triply Nested, High-Resolution Operational Version of the Hurricane Weather Research and Forecasting Model (HWRF): Track and Intensity Forecast Verifications." *Weather and Forecasting* 30 (3): 710–29. https://doi.org/10.1175/WAF-D-14-00098.1.

GRAY, WILLIAM M. 1968. "Global View of the Origin of Tropical Disturbances and Storms." *Monthly Weather Review* 96 (10): 669–700. https://doi.org/10.1175/1520-0493(1968)096<0669:gvotoo>2.0.co;2.

Green, Benjamin W., and Fuqing Zhang. 2013. "Impacts of Air-Sea Flux Parameterizations on the Intensity and Structure of Tropical Cyclones." *Monthly Weather Review* 141 (7). https://doi.org/10.1175/MWR-D-12-00274.1.

Harper, B A, J D Kepert, and J D Ginger. 2010. "WMO Guidelines For Converting Between Various Wind Averaging Periods In Tropical Cyclone Conditions." *World Meteorological Organization*.

Hilburn, Kyle A., F. J. Wentz, D. K. Smith, and P. D. Ashcroft. 2006. "Correcting Active Scatterometer Data for the Effects of Rain Using Passive Radiometer Data." *Journal of Applied Meteorology and Climatology* 45 (3). https://doi.org/10.1175/JAM2357.1.

Holland, Greg J. 1980. "An Analytic Model of the Wind and Pressure Profiles in Hurricanes." *Monthly Weather Review* 108: 1212–18.

Holland, Greg J., James I. Belanger, and Angela Fritz. 2010. "A Revised Model for Radial Profiles of Hurricane Winds." *Monthly Weather Review* 138 (12): 4393–4401. https://doi.org/10.1175/2010MWR3317.1.

Hwang, Paul A., Derek M. Burrage, David W. Wang, and Joel C. Wesson. 2013. "Ocean Surface Roughness Spectrum in High Wind Condition for Microwave Backscatter and Emission Computations." *Journal of Atmospheric and Oceanic Technology* 30 (9).

https://doi.org/10.1175/JTECH-D-12-00239.1.

Jarvinen, B. R., C. J. Neumann, and M. A.S. Davis. 1984. “Tropical Cyclone Data Tape for the North Atlantic Basin, 1886- 1983: Contents, Limitations and Uses.”

Kerr, Yann H., Philippe Waldteufel, Jean Pierre Wigneron, Steven Delwart, François Cabot, Jacqueline Boutin, Maria José Escorihuela, et al. 2010. “The SMOS L: New Tool for Monitoring Key Elements Ofthe Global Water Cycle.” *Proceedings of the IEEE* 98 (5). https://doi.org/10.1109/JPROC.2010.2043032.

Kim, Hyunglok, and Venkat Lakshmi. 2018. “Use of Cyclone Global Navigation Satellite System (CyGNSS) Observations for Estimation of Soil Moisture.” *Geophysical Research Letters* 45 (16): 8272–82. https://doi.org/10.1029/2018GL078923.

Knapp, Kenneth R., Michael C. Kruk, David H. Levinson, Howard J. Diamond, and Charles J. Neumann. 2010. “The International Best Track Archive for Climate Stewardship (IBTrACS).” *Bulletin of the American Meteorological Society* 91 (3): 363–76. https://doi.org/10.1175/2009BAMS2755.1.

Knapp, Kenneth R., Christopher S. Velden, and Anthony J. Wimmers. 2018. “A Global Climatology of Tropical Cyclone Eyes.” *Monthly Weather Review* 146 (7): 2089–2101. https://doi.org/10.1175/MWR-D-17-0343.1.

Lagerloef, Gary, F. Raul Colomb, David le Vine, Frank Wentz, Simon Yueh, Christopher S. Ruf, Jonathan Lilly, et al. 2008. “The Aquarius/SAC-D Mission: Designed to Meet the Salinity Remote-Sensing Challenge.” *Oceanography* 21 (SPL.ISS. 1). https://doi.org/10.5670/oceanog.2008.68.

Lajoie, France, and Kevin Walsh. 2008. “A Technique to Determine the Radius of Maximum Wind of a Tropical Cyclone.” *Weather and Forecasting* 23 (5). https://doi.org/10.1175/2008WAF2007077.1.

Landsea, Christopher W., and James L. Franklin. 2013. “Atlantic Hurricane Database Uncertainty and Presentation of a New Database Format.” *Monthly Weather Review* 141 (10): 3576–92. https://doi.org/10.1175/MWR-D-12-00254.1.

Lanzante, John R. 2019. “Uncertainties in Tropical-Cyclone Translation Speed.” *Nature* 570 (7759). https://doi.org/10.1038/s41586-019-1223-2.

Li, Weiqiang, Estel Cardellach, Fran Fabra, Serni Ribo, and Antonio Rius. 2020. “Assessment of Spaceborne GNSS-R Ocean Altimetry Performance Using CYGNSS Mission Raw Data.” *IEEE Transactions on Geoscience and Remote Sensing* 58 (1): 238–50. https://doi.org/10.1109/TGRS.2019.2936108.

Lin, Ning, and Daniel Chavas. 2012. “On Hurricane Parametric Wind and Applications in Storm Surge Modeling.” *Journal of Geophysical Research Atmospheres* 117 (9): 1–19. https://doi.org/10.1029/2011JD017126.

Lin, W., M. Portabella, A. Stoffelen, and A. Verhoef. 2013. “On the Characteristics of ASCAT Wind Direction Ambiguities.” *Atmospheric Measurement Techniques* 6 (4): 1053–60. https://doi.org/10.5194/amt-6-1053-2013.

Mashburn, Jake, Penina Axelrad, Cinzia Zuffada, Eric Loria, Andrew Obrien, and Bruce Haines. 2020. “Improved Gnss-r Ocean Surface Altimetry with Cygnss in the Seas of Indonesia.” *IEEE Transactions on Geoscience and Remote Sensing* 58 (9): 6071–87. https://doi.org/10.1109/TGRS.2020.2973079.

Mayers, David, and Christopher S. Ruf. 2019. “Tropical Cyclone Center Fix Using CYGNSS Winds.” *Journal of Applied Meteorology and Climatology* 58 (9). https://doi.org/10.1175/JAMC-D-19-0054.1.

———. 2020. “Estimating the True Maximum Sustained Wind Speed of a Tropical Cyclone from Spatially Averaged Observations.” *Journal of Applied Meteorology and Climatology* 59 (2). https://doi.org/10.1175/JAMC-D-19-0177.1.

———. 2021. “MTrack: Improved Center Fix of Tropical Cyclones from SMAP Wind Observations.” *Bulletin of the American Meteorological Society*. https://doi.org/10.1175/BAMS-D-20-0068.1.

Meissner, Thomas, Lucrezia Ricciadulli, and Frank J. Wentz. 2017. “Capability of the SMAP Mission to Measure Ocean Surface Winds in Storms.” *Bulletin of the American Meteorological Society* 98 (8). https://doi.org/10.1175/BAMS-D-16-0052.1.

Meissner, Thomas, and Frank J. Wentz. 2009. “Wind-Vector Retrievals under Rain with Passive Satellite Microwave Radiometers.” *IEEE Transactions on Geoscience and Remote Sensing* 47 (9). https://doi.org/10.1109/TGRS.2009.2027012.

Meissner, Thomas, Frank J. Wentz, and Lucrezia Ricciardulli. 2014. “The Emission and Scattering of L-Band Microwave Radiation from Rough Ocean Surfaces and Wind Speed Measurements from the Aquarius Sensor.” *Journal of Geophysical Research C: Oceans* 119 (9). https://doi.org/10.1002/2014JC009837.

Misra, Pratap, and Per Enge. 2012. *Global Positioning System: Signals, Measurements, and Performance*. 2nd ed. Ganga-Jamuna Press.

Morris, Mary, Clara Chew, John T. Reager, Rashmi Shah, and Cinzia Zuffada. 2019. “A Novel Approach to Monitoring Wetland Dynamics Using CYGNSS: Everglades Case Study.” *Remote Sensing of Environment* 233. https://doi.org/10.1016/j.rse.2019.111417.

Morris, Mary, and Christopher S. Ruf. 2017a. “Determining Tropical Cyclone Surface Wind Speed Structure and Intensity with the CYGNSS Satellite Constellation.” *Journal of Applied Meteorology and Climatology* 56 (7): 1847–65. https://doi.org/10.1175/JAMC-D-16-0375.1.

———. 2017b. “Estimating Tropical Cyclone Integrated Kinetic Energy with the CYGNSS Satellite Constellation.” *Journal of Applied Meteorology and Climatology* 56 (1): 235–45.

https://doi.org/10.1175/jamc-d-16-0176.1.

Mouche, Alexis A., Bertrand Chapron, Biao Zhang, and Romain Husson. 2017. “Combined Co- A Nd Cross-Polarized SAR Measurements under Extreme Wind Conditions.” *IEEE Transactions on Geoscience and Remote Sensing* 55 (12). https://doi.org/10.1109/TGRS.2017.2732508.

Murakami, Hiroyuki, Yuqing Wang, Hiromasa Yoshimura, Ryo Mizuta, Masato Sugi, Eiki Shindo, Yukimasa Adachi, et al. 2012. “Future Changes in Tropical Cyclone Activity Projected by the New High-Resolution MRI-AGCM.” *Journal of Climate* 25 (9): 3237–60. https://doi.org/10.1175/JCLI-D-11-00415.1.

“NOAA National Centers for Environmental Information (NCEI) U.S. Billion-Dollar Weather and Climate Disasters.” 2020. 2020. https://doi.org/10.25921/stkw-7w73.

NOAA, Office of Marine & Aviation Operations. 2017. “Lockheed WP-3D Orion.” 2017. https://www.omao.noaa.gov/learn/aircraft-operations/aircraft/lockheed-wp-3d-orion.

Olander, Timothy L., and Christopher S. Velden. 2007. “The Advanced Dvorak Technique: Continued Development of an Objective Scheme to Estimate Tropical Cyclone Intensity Using Geostationary Infrared Satellite Imagery.” *Weather and Forecasting* 22 (2). https://doi.org/10.1175/WAF975.1.

Paulsen, Becca M., and J. L. Schroeder. 2005. “An Examination of Tropical and Extratropical Gust Factors and the Associated Wind Speed Histograms.” *Journal of Applied Meteorology* 44 (2). https://doi.org/10.1175/JAM2199.1.

Portabella, Marcos, Ad Stoffelen, Wenming Lin, Antonio Turiel, Anton Verhoef, Jeroen Verspeek, and Joaquim Ballabrera-Poy. 2012. “Rain Effects on ASCAT-Retrieved Winds: Toward an Improved Quality Control.” *IEEE Transactions on Geoscience and Remote Sensing* 50 (7 PART1). https://doi.org/10.1109/TGRS.2012.2185933.

Powell, Mark D., and T. A. Reinhold. 2007. “Tropical Cyclone Destructive Potential by Integrated Kinetic Energy.” *Bulletin of the American Meteorological Society* 88 (4). https://doi.org/10.1175/BAMS-88-4-513.

Rappaport, Edward N. 2014. “Fatalities in the United States from Atlantic Tropical Cyclones: New Data and Interpretation.” *Bulletin of the American Meteorological Society* 95 (3). https://doi.org/10.1175/BAMS-D-12-00074.1.

Rappaport, Edward N., James L. Franklin, Lixion A. Avila, Stephen R. Baig, John L. Beven, Eric S. Blake, Christopher A. Burr, et al. 2009. “Advances and Challenges at the National Hurricane Center.” *Weather and Forecasting* 24 (2): 395–419. https://doi.org/10.1175/2008WAF2222128.1.

Reul, Nicolas, B. Chapron, E. Zabolotskikh, C. Donlon, Y. Quilfen, S. Guimbard, and J. F. Piolle. 2016. “A Revised L-Band Radio-Brightness Sensitivity to Extreme Winds under Tropical Cyclones: The Five Year SMOS-Storm Database.” *Remote Sensing of*

Environment 180. https://doi.org/10.1016/j.rse.2016.03.011.

Reul, Nicolas, Joseph Tenerelli, Bertrand Chapron, Doug Vandemark, Yves Quilfen, and Yann Kerr. 2012. "SMOS Satellite L-Band Radiometer: A New Capability for Ocean Surface Remote Sensing in Hurricanes." *Journal of Geophysical Research: Oceans* 117 (2). https://doi.org/10.1029/2011JC007474.

Rohde, Robert A. 2006. "Historic Tropical Cyclone Tracks." 2006. https://earthobservatory.nasa.gov/images/7079/historic-tropical-cyclone-tracks.

Ruf, Christopher S. 2018. "Algorithm Theoretical Basis Document Level 3 Gridded Wind Speed." https://podaac.jpl.nasa.gov/CYGNSS?tab=documentation.

Ruf, Christopher S., Shakeel Asharaf, Rajeswari Balasubramaniam, Scott Gleason, Timothy Lang, Darren McKague, Dorina Twigg, and Duane Waliser. 2019. "In-Orbit Performance of the Constellation of CYGNSS Hurricane Satellites." *Bulletin of the American Meteorological Society* 100 (10). https://doi.org/10.1175/BAMS-D-18-0337.1.

Ruf, Christopher S., and Rajeswari Balasubramaniam. 2019. "Development of the CYGNSS Geophysical Model Function for Wind Speed." *IEEE Journal of Selected Topics in Applied Earth Observations and Remote Sensing* 12 (1): 66–77. https://doi.org/10.1109/JSTARS.2018.2833075.

Ruf, Christopher S., Paul Chang, Maria-Paola Clarizia, and Scott Gleason. 2016. *CYGNSS Handbook*. Michigan Publishing.

Ruf, Christopher S., Clara Chew, Timothy Lang, Mary G. Morris, Kyle Nave, Aaron Ridley, and Rajeswari Balasubramaniam. 2018. "A New Paradigm in Earth Environmental Monitoring with the CYGNSS Small Satellite Constellation." *Scientific Reports* 8 (1): 1–13. https://doi.org/10.1038/s41598-018-27127-4.

Ruf, Christopher S., Scott Gleason, and Darren S. McKague. 2019. "Assessment of CYGNSS Wind Speed Retrieval Uncertainty." *IEEE Journal of Selected Topics in Applied Earth Observations and Remote Sensing* 12 (1). https://doi.org/10.1109/JSTARS.2018.2825948.

Senyurek, Volkan, Fangni Lei, Dylan Boyd, Ali Cafer Gurbuz, Mehmet Kurum, and Robert Moorhead. 2020. "Evaluations of a Machine Learning-Based Cygnss Soil Moisture Estimates against Smap Observations." *Remote Sensing* 12 (21): 1–21. https://doi.org/10.3390/rs12213503.

Simpson, R.H. 1974. "The Hurricane Disaster—Potential Scale." *Weatherwise* 27 (4). https://doi.org/10.1080/00431672.1974.9931702.

Stiles, Bryan W., and Simon H. Yueh. 2002. "Impact of Rain on Spaceborne Ku-Band Wind Scatterometer Data." *IEEE Transactions on Geoscience and Remote Sensing* 40 (9). https://doi.org/10.1109/TGRS.2002.803846.

Teng, Chung-Chu. 2010. "Ocean Observation from NOAA National Data Buoy Center's

Platforms." *Ocean Sensing and Monitoring II* 7678 (April 2010): 76780E. https://doi.org/10.1117/12.849778.

Thorncroft, C., and K. Hodges. 2001. "African Easterly Wave Variability and Its Relationship to Atlantic Tropical Cyclone Activity." *Journal of Climate* 14 (6): 1166–79. https://doi.org/10.1175/1520-0442(2001)014<1166:AEWVAI>2.0.CO;2.

Torn, Ryan D., and Chris Snyder. 2012. "Uncertainty of Tropical Cyclone Best-Track Information." *Weather and Forecasting* 27 (3). https://doi.org/10.1175/WAF-D-11-00085.1.

Trahan, Sam, and Lynn Sparling. 2012. "An Analysis of NCEP Tropical Cyclone Vitals and Potential Effects on Forecasting Models." *Weather and Forecasting* 27 (3). https://doi.org/10.1175/WAF-D-11-00063.1.

Uhlhorn, Eric W., Peter G. Black, James L. Franklin, Mark Goodberlet, James Carswell, and Alan S. Goldstein. 2007. "Hurricane Surface Wind Measurements from an Operational Stepped Frequency Microwave Radiometer." *Monthly Weather Review* 135 (9). https://doi.org/10.1175/MWR3454.1.

Velden, Christopher, Bruce Harper, Frank Wells, John L. Beven, Ray Zehr, Timothy Olander, Max Mayfield, et al. 2006. "Supplement To: The Dvorak Tropical Cyclone Intensity Estimation Technique: A Satellite-Based Method That Has Endured for over 30 Years." *Bulletin of the American Meteorological Society* 87 (9). https://doi.org/10.1175/bams-87-9-velden.

Vose, Russell S., Scott Applequist, Mark A. Bourassa, Sara C. Pryor, Rebecca J. Barthelmie, Brian Blanton, Peter D. Bromirski, et al. 2014. "Monitoring and Understanding Changes in Extremes: Extratropical Storms, Winds, and Waves." *Bulletin of the American Meteorological Society* 95 (3): 377–86. https://doi.org/10.1175/BAMS-D-12-00162.1.

Walsh, Kevin J.E., Suzana J. Camargo, Gabriel A. Vecchi, Anne Sophie Daloz, James Elsner, Kerry Emanuel, Michael Horn, et al. 2015. "Hurricanes and Climate: The U.S. Clivar Working Group on Hurricanes." *Bulletin of the American Meteorological Society* 96 (6): 997–1017. https://doi.org/10.1175/BAMS-D-13-00242.1.

Wang, Tianlin, Christopher S. Ruf, Scott Gleason, Bruce Block, Darren McKague, and Andrew O'Brien. 2019. "A Real-Time EIRP Level 1 Calibration Algorithm for the CYGNSS Mission Using the Zenith Measurements." In . https://doi.org/10.1109/igarss.2019.8900456.

Wang, Yuqing, and Charlie Wu. 2004. "Current Understanding of Tropical Cyclone Structure and Intensity Changes - A Review." *Meteorology and Atmospheric Physics* 87 (4): 257–78. https://doi.org/10.1007/s00703-003-0055-6.

Warnock, April, and Christopher S. Ruf. 2019. "Response to Variations in River Flowrate by a Spaceborne GNSS-R River Width Estimator." *Remote Sensing* 11 (20): 1–8. https://doi.org/10.3390/rs11202450.

Warnock, April, Christopher S. Ruf, and Mary Morris. 2017. "Storm Surge Prediction with

Cygnss Winds." In *2017 IEEE International Geoscience and Remote Sensing Symposium (IGARSS)*. IEEE. https://doi.org/10.1109/IGARSS.2017.8127624.

Weissman, David E., and Mark A. Bourassa. 2008. "Measurements of the Effect of Rain-Induced Sea Surface Roughness on the QuikSCAT Scatterometer Radar Cross Section." In *IEEE Transactions on Geoscience and Remote Sensing*. Vol. 46. https://doi.org/10.1109/TGRS.2008.2001032.

Wentz, F. J., L. A. Mattox, and S. Peteherych. 1986. "New Algorithms for Microwave Measurements of Ocean Winds: Applications to Seasat and the Special Sensor Microwave Imager." *Journal of Geophysical Research* 91 (C2). https://doi.org/10.1029/JC091iC02p02289.

Willoughby, Hugh E., R. W.R. Darling, and M. E. Rahn. 2006. "Parametric Representation of the Primary Hurricane Vortex. Part II: A New Family of Sectionally Continuous Profiles." *Monthly Weather Review* 134 (4): 1102–20. https://doi.org/10.1175/MWR3106.1.

Wimmers, Anthony J., and Christopher S. Velden. 2016. "Advancements in Objective Multisatellite Tropical Cyclone Center Fixing." *Journal of Applied Meteorology and Climatology* 55 (1). https://doi.org/10.1175/JAMC-D-15-0098.1.

Wu, Xuerui, Zhounan Dong, Shuanggen Jin, Yang He, Yezhi Song, Wenxiao Ma, and Lei Yang. 2020. "First Measurement of Soil Freeze/Thaw Cycles in the Tibetan Plateau Using CYGNSS GNSS-R Data." *Remote Sensing* 12 (15). https://doi.org/10.3390/RS12152361.

Wu, Xuerui, Shuanggen Jin, and Xinqiu Ouyang. 2020. "A Full-Polarization GNSS-R Delay-Doppler-Map (DDM) Simulator for Bare Soil Freeze/Thaw Process Detection." *Geoscience Letters* 7 (1). https://doi.org/10.1186/s40562-020-00154-8.

Yablonsky, Richard M., Isaac Ginis, Biju Thomas, Vijay Tallapragada, Dmitry Sheinin, and Ligia Bernardet. 2015. "Description and Analysis of the Ocean Component of NOAA'S Operational Hurricane Weather Research and Forecasting Model (HWRF)." *Journal of Atmospheric and Oceanic Technology* 32 (1): 144–63. https://doi.org/10.1175/JTECH-D-14-00063.1.

Zabolotskikh, Elizaveta V., Leonid M. Mitnik, Nicolas Reul, and Bertrand Chapron. 2015. "New Possibilities for Geophysical Parameter Retrievals Opened by GCOM-W1 AMSR2." In *IEEE Journal of Selected Topics in Applied Earth Observations and Remote Sensing*. Vol. 8. https://doi.org/10.1109/JSTARS.2015.2416514.

Zabolotskikh, Elizaveta V., Nicolas Reul, and Bertrand Chapron. 2016. "Geophysical Model Function for the AMSR2 C-Band Wind Excess Emissivity at High Winds." *IEEE Geoscience and Remote Sensing Letters* 13 (1). https://doi.org/10.1109/LGRS.2015.2497463.

Zavorotny, Valéry U., and Alexander G. Voronovich. 2000. "Scattering of GPS Signals from the Ocean with Wind Remote Sensing Application." *IEEE Transactions on Geoscience and Remote Sensing* 38 (2 II). https://doi.org/10.1109/36.841977.

Zhang, Z., and T.N. Krishnamurti. 1997. “Ensemble Forecasting of Hurricane Tracks.” *Bulletin of the American Meteorological Society* 78 (12): 2785–96.